Loss of epigenetic information as a cause of mammalian aging

Jae-Hyun Yang,[1,27] Motoshi Hayano,[1,2,27] Patrick T. Griffin,[1] Joao A. Amorim,[1,3] Michael S. Bonkowski,[1] John K. Apostolides,[4] Marco Blanchette,[5] Elizabeth M. Munding,[5] Mital Bhakta,[5] Elias L. Salfati,[1,26] Yuancheng Lu,[1] Daniel L. Vera,[1] Jaime M. Ross,[1] Giuseppe Coppotelli,[1] Yap Ching Chew,[6] Wei Guo,[6] Xiaojing Yang,[6] Margarita V. Meer,[7] Xiao Tian,[1] Zhixun Dou,[8] Caiyue Xu,[8] Jeffrey W. Pippin,[9] Michael L. Creswell,[9,10] Sarah J. Mitchell,[11] Abhirup Das,[1,12] Brendan L. O'Connell,[13] Sachin Thakur,[1] Alice E. Kane,[1] Qiao Su,[4] Yasuaki Mohri,[14] Emi K. Nishimura,[14] Laura Schaevitz,[15] Neha Garg,[1] Ana-Maria Balta,[1] Meghan A. Rego,[1] Meredith Gregory-Ksander,[16] Tatjana C. Jakobs,[16] Lei Zhong,[17] Hiroko Wakimoto,[18] Raul Mostoslavsky,[17] Amy J. Wagers,[19] Kazuo Tsubota,[2] Stephen J. Bonasera,[20] Carlos M. Palmeira,[21] Jonathan G. Seidman,[18] Christine E. Seidman,[18] Norman S. Wolf,[22] Jill A. Kreiling,[23] John M. Sedivy,[23] George F. Murphy,[24] Richard E. Green,[13] Benjamin A. Garcia,[8] Shelley L. Berger,[8] Philipp Oberdoerffer,[25] Stuart J. Shankland,[9] Vadim N. Gladyshev,[7] Bruce R. Ksander,[16] Andreas R. Pfenning,[4] Luis A. Rajman,[1] and David A. Sinclair,[1,28*]

[1]Paul F. Glenn Center for Biology of Aging Research, Department of Genetics, Blavatnik Institute, Harvard Medical School, Boston, MA 02115, USA

[2]Department of Ophthalmology, Keio University School of Medicine, 35 Shinanomachi, Shinjuku-ku, Tokyo, 160-8582, Japan

[3]IIIUC-Institute of Interdisciplinary Research, University of Coimbra, Coimbra, Portugal

[4]Computational Biology Department, Carnegie Mellon University, Pittsburgh, PA 15213, USA

[5]Dovetail Genomics, Scotts Valley, CA 95066, USA

[6]Zymo Research Corporation, Irvine, CA 92614, USA

[7]Division of Genetics, Department of Medicine, Brigham and Women's Hospital, Harvard Medical School, Boston, MA 02115, USA

[8]Department of Cell and Developmental Biology, Perelman School of Medicine, University of Pennsylvania, Philadelphia, PA 19104, USA

[9]Division of Nephrology, University of Washington, Seattle, WA 98109, USA

[10]Georgetown University School of Medicine, Washington DC 20007, USA

[11]Experimental Gerontology Section, Translational Gerontology Branch, National Institute on Aging, NIH, Baltimore, MD 21224, USA

[12]Laboratory for Ageing Research, Department of Pharmacology, School of Medical Sciences, The University of New South Wales, Sydney, NSW 2052, Australia

35 [13]Department of Biomolecular Engineering, University of California, Santa Cruz, CA 95064, USA

36 [14]Department of Stem Cell Biology, Medical Research Institute, Tokyo Medical and Dental University, 1-5-45

37 Yushima, Bunkyo-ku, Tokyo, 113-8510, Japan

38 [15]Vium Inc., San Mateo, CA 94402 USA

39 [16]Schepens Eye Research Institute, Department of Ophthalmology, Massachusetts Eye and Ear Infirmary, Harvard

40 Medical School, Boston, MA 02114

41 [17]The Massachusetts General Hospital Cancer Center, Harvard Medical School, Boston, MA 02114, USA

42 [18]Department of Genetics, Harvard Medical School, Boston, MA 02115, USA

43 [19]Paul F. Glenn Center for the Biology of Aging Research and Department of Stem Cell and Regenerative Biology,

44 Harvard Stem Cell Institute, Harvard University, Cambridge, MA, USA

45 [20]Division of Geriatrics, Department of Internal Medicine, University of Nebraska Medical Center, 3028 Durham

46 Research Center II, Omaha, NE, 68198-5039, USA

47 [21]Department of Life Sciences, Faculty of Sciences and Technology, University of Coimbra, Coimbra, Portugal

48 [22]Department of Pathology, University of Washington, Seattle, WA 98195, USA

49 [23]Department of Molecular Biology, Cell Biology and Biochemistry, Brown University, Providence, RI 02912, USA

50 [24]Program in Dermatopathology, Department of Pathology, Brigham & Women's Hospital, Harvard Medical School,

51 Boston, MA 02115, USA

52 [25]Laboratory of Receptor Biology and Gene Expression, National Cancer Institute, NIH, Bethesda, MD 20892, USA

53 [26]Present address: Department of Integrative Structural and Computational Biology, The Scripps Research

54 Institute, La Jolla, CA, USA

55 [27]These authors contributed equally

56 [28]Lead Contact

57 *Correspondence: david_sinclair@hms.harvard.edu

58 **Short-title:** DSB-induced epigenetic drift as a cause of aging

59 **One Sentence Summary:** The act of repairing DNA breaks induces chromatin reorganization

60 and a loss of cell identity that may contribute to mammalian aging

61

62

63

64

65

66

2

67   **SUMMARY**

68   All living things experience entropy, manifested as a loss of inherited genetic and epigenetic

69   information over time. As budding yeast cells age, epigenetic changes result in a loss of cell

70   identity and sterility, both hallmarks of yeast aging. In mammals, epigenetic information is also

71   lost over time, but what causes it to be lost and whether it is a cause or a consequence of aging

72   is not known. Using a transgenic mouse system called "ICE" (for Inducible Changes to the

73   Epigenome), we show that the process of repairing non-mutagenic double-stranded DNA breaks

74   (DSBs) accelerates age-related physiological, cognitive, and molecular changes, including the

75   erosion of the epigenetic landscape, a loss of cellular identity, cellular senescence and

76   advancement of the epigenetic clock. Epigenetic reprogramming through ectopic expression of

77   *Oct4*, *Sox2* and *Klf4* (OSK) restores patterns of youthful gene expression. These data support a

78   model in which a loss of epigenetic information is a cause of aging in mammals.

79
80
81
82
83
84
85
86
87
88
89
90
91
92
93
94
95
96

INTRODUCTION

To maintain function, cells utilize energy from their environment to preserve both genetic information encoded in DNA, and 'epigenetic' information encoded in transcriptional networks, histone modifications, chromatin conformation, and DNA methylation (DNAme) patterns (Kane and Sinclair, 2019; Keller, 2009).

In the 1950s, Szilard and Medawar independently proposed that aging is caused by a loss of genetic information (Medawar, 1952; Szilard, 1959). The type of DNA damage that is most consistently linked to aging is the double-stranded DNA break (DSB), occurring at a rate of 10 to 50 per cell per day (Vilenchik and Knudson, 2003). For example, a recent comparison of 18 different rodent species found that, of all DNA repair processes, the repair of DSBs was by far most highly correlated with lifespan (Tian et al., 2019). Indeed, in mice, defects in DSB repair due to the deletion of *Ku70*, *Ku80* or *Ercc1* result in accelerated aging (progeroid) phenotypes (Li et al., 2007; Niedernhofer et al., 2006), and overexpression of the DSB repair protein SIRT6 extends the lifespan of mice (Kaya et al., 2015; Mao et al., 2011; Roichman et al., 2021).

Recently, experiments to test the importance of mutations as a driver of aging have led to questions about its primacy. In numerous species, there is a paucity of mutations in old cells and strains of mice with high levels of free radicals or mutation rates show little to no sign of premature aging (Narayanan et al., 1997). In addition, mice with defects in DNA repair and progeroid phenotypes, such as the *Ercc2* (*Xpd*)$^{m/m}$ mutant mouse, have no detectable increase in mutation rates (Dolle et al., 2006). Perhaps the strongest argument against a loss of genomic information as a ubiquitous cause of aging is the fact that mammals can be cloned from old somatic cells to produce new individuals with normal lifespans (Burgstaller and Brem, 2017).

A loss of epigenetic information as a cause of aging emerged from studies of *Saccharomyces cerevisiae* in the 1990's (Kennedy et al., 1997; Sinclair et al., 1997). In old yeast cells, relocalization of the silent information regulator complex (Sir2/3/4) away from genes that control cell identity and into the nucleolus results in sterility, a hallmark of yeast aging (Smeal et al., 1996). Global epigenetic changes are also seen, including decreases in heterochromatin,

4

128 histone occupancy, altered epigenetic regulators, histone modifications (e.g. H3K56ac and
129 H4K16ac), and an increase in gene transcription globally. Modulation of chromatin factors
130 extends yeast lifespan, including overexpression of *SIR2* or histone genes, or deletion of the
131 histone acetyltransferase gene *HAT2* or histone methyltransferase gene *SET2*, indicating that
132 epigenetic changes are a cause of yeast aging, not merely a biomarker (Dang et al., 2009;
133 Feser et al., 2010; Hu et al., 2014; Kaeberlein et al., 1999; Rosaleny et al., 2005; Ryu et al.,
134 2014).

135

136 Epigenetic changes also occur during aging in multicellular organisms and the rate at which they
137 change is associated with longer lifespans. Examples of epigenetic marks that change during
138 aging include DNAme, H3K4me3 (a euchromatic mark) and H3K9me3 and H3K27me3
139 (heterochromatic marks) (Benayoun et al., 2015; Pal and Tyler, 2016; Sen et al., 2016). Similar
140 to yeast, there is also evidence that epigenetic changes are not simply biomarkers of aging but
141 play an active role. In worms, for example, deletion of genes encoding components of the
142 H3K4me3 complex extends lifespan (Greer et al., 2010; Greer et al., 2011) and in *Drosophila*,
143 dietary restriction and overexpression of the Sir2 gene maintains a youthful epigenome and
144 extends lifespan (Jiang et al., 2013; Rogina and Helfand, 2004; Wood et al., 2016). Similarly,
145 the epigenome of the naked mole rat, a long-lived rodent, is significantly more stable than in
146 mice (Tan et al., 2017).

147

148 One of the most striking discoveries about the epigenome in recent years is that the methylation
149 status of specific CpG sites change with predictability during aging, and can therefore be used
150 to estimate biological age, not just within members of a species but across diverse species,
151 implying a conserved mechanism (Hannum et al., 2013; Horvath, 2013; Lu et al., 2021;
152 Petkovich et al., 2017; Weidner et al., 2014). Whether or not DNA methylation "clocks" play a
153 role in aging or are indicative of overall epigenomic stability is not yet clear (Kan and Sinclair,
154 2020 insert).

155

156 Together, these findings have led to a shift from viewing aging as a random process to one that
157 is non-random and potentially driven by reproducible and predictable epigenetic changes. But
158 key questions remain. What causes the epigenome to change over time and does this cause

159 aging? If DNA repair alters the epigenome, how do these seemingly random events produce

160 similar gene expression changes in cells and individuals, making it appear as though it were a

161 program?

162

163 Again, clues have come from *S. cerevisiae*. A major driver of epigenetic change in yeast

164 is the DSB. The resulting DNA damage signal recruits epigenetic regulators such as Sir2, Hst1,

165 Rpd3, Gcn5, and Esa1 to the DNA break site, where they assist with repair and then return to

166 their original genomic locations (Martin et al., 1999; McAinsh et al., 1999; Mills et al., 1999;

167 Tamburini and Tyler, 2005). The Relocalization of Chromatin Modifiers or "RCM" Hypothesis

168 (Sinclair and LaPlante, 2019) proposes that RCM evolved to coordinate gene expression with

169 DNA repair (Oberdoerffer and Sinclair, 2007) but, over time, the epigenomic landscape is

170 altered, cells lose their identity, and aging ensues. In other words, aging may be caused by the

171 dysregulation of transcriptional networks and epigenetic information over time, driven by a

172 conserved mechanism that evolved to co-regulate genetic and epigenetic responses (Mills et al.,

173 1999; Oberdoerffer et al., 2008). This idea is consistent with antagonistic pleiotropy, in which an

174 advantageous biological system is deleterious later in life (Williams, 1957).

175

176 To test whether epigenetic changes are a cause of mammalian aging, we generated a system

177 that allowed us to accelerate age-related epigenetic changes called ICE (for <u>I</u>nducible <u>C</u>hanges

178 to the <u>E</u>pigenome). Using this system, we provide evidence that changes to the epigenetic

179 landscape lead to a loss of cellular identity, accelerate the DNA methylation clock, and cause an

180 age-related decline in tissue function, which together support the hypothesis that a loss of

181 epigenetic information over time is a cause of aging.

182

183 **RESULTS**

184

185 **A system to induce epigenetic aging**

186 To test the hypothesis that epigenetic changes are an underlying cause of aging, we developed

187 a system that allows for precise temporal and spatial control over DSBs in cells and mice. To

188 test if DSB repair perturbs the epigenome in mammals, we employed I-*Ppo*I, a homing

189 endonuclease encoded by the slime mold *Physarum polycephalum*, to create non-mutagenic

6

190 DSBs. The enzyme has been used previously to study DSB repair in the context of the RCM

191 response, including the roles of ATM, NBS1, SIRT1, SIRT6, HDAC1, and LSD1 (Berkovich et

192 al., 2007; Dobbin et al., 2013; McCord et al., 2009; Mosammaparast et al., 2013). I-*Ppo*I

193 recognizes the DNA sequence CTCTCTTAA▼GGTAGC (Monnat et al., 1999), which is found at

194 20 loci in the mouse genome, 19 of which are non-coding including the rDNA, and none of

195 which occur in mitochondrial DNA (Berkovich et al., 2007).

196

197 The transgenic system consisted of two components: the first is a fusion of the I-*Ppo*I gene to

198 the C-terminus of a tamoxifen (TAM)-regulated mutant estrogen receptor domain gene (ER^{T2})

199 and a transcriptional *loxP*-STOP-*loxP* cassette that is targeted by Cre recombinase (Berkovich

200 et al., 2007) (**Figure 1A**). The second is a tamoxifen-regulated Cre recombinase gene (Cre-

201 ER^{T2}) under the control of the human ubiquitin C promoter to ensure whole-body expression

202 (Ruzankina et al., 2007). When the two components are combined *in vivo* and tamoxifen is

203 provided, Cre-ER^{T2} is expressed and directed to the nucleus where it excises the stop cassette,

204 facilitating transcription of the ER^{T2}-HA-I-*Ppo*I-IRES-GFP gene cassette. The protein product,

205 ER^{T2}-I-*Ppo*I, is then directed to the nucleus. Upon removal of tamoxifen, ER^{T2}-I-*Ppo*I is no

206 longer directed to the nucleus and is degraded in the cytoplasm (**Figure 1A**). C57BL6/J

207 transgenic mice containing each of these components were crossed, generating Het ER^{T2}-I-

208 *Ppo*I and Cre-ER^{T2}, named Inducible Changes to the Epigenome or "ICE" mice, with wildtype

209 (WT), I-*Ppo*I and Cre mice serving as negative controls (**Figure S1A**). Unlike other methods of

210 creating DSBs, such as CRISPR, chemicals and radiation, low level expression of I-*Ppo*I

211 creates cuts with 4-base overhangs that we predicted would be repaired without causing a

212 mutation.

213

214 To generate an equivalent cell-based ICE system, mouse embryonic fibroblasts (MEFs) were

215 isolated from littermates at day E13.5 and cultured in low oxygen (3% v/v). After the addition of

216 tamoxifen (0.5 μM 4-OHT), HA-I-*Ppo*I was detected in the nucleus (**Figure 1B**) and the number

217 of serine 139-phosphorylated H2AX (γH2AX) foci, a marker of DSBs, reached a maximum of 4-

218 fold above background at the 24-hour treatment time point, the extent of cutting being locus-

219 dependent (**Figure 1C and 1D**). Compared to the DNA damaging agent etoposide, a

220 topoisomerase II inhibitor, and phleomycin, a free-radical inducer, the number of γH2AX foci, the

7

extent of DNA breakage, and the DNA damage response in the ICE cells was minimal (**Figure S1B-S1D**). During and after I-*Ppo*I induction, there was no detectable change in the cell cycle profile or percent senescent cells (**Figure S1F-S1G**). In the post-treated ICE cells, we did not detect any change in mutation frequency at the 28S rDNA (**Figure S2A-S2D**), RNA levels (**Figure S2E and S2F**) or overall translation efficiency (**Figure S2L and S2M**). To detect residual I-*Ppo*I activity, we performed ligation-mediated PCR (LM-PCR) using probes complementary to I-*Ppo*I overhangs (**Figure S2H**). No residual I-*Ppo*I activity was detected at the 96-hour time point (**Figure S2I and S2J**).

To test if the treatment accelerated epigenetic aging, three independent ICE cell lines were treated as above and the extend of DNA methylation was measured using reduced representation bisulfite sequencing (RRBS). Using a weighted sum of 89 age-associated methylation sites and a refined set of 74 sites (Petkovich et al., 2017), the DNA methylation age of the cells was on ~1.5-fold greater than the Cre control cells, indicating that post-treated ICE cells were epigenetically older (**Figure 1E;** p=0.01, p=0.008, respectively).

If the RCM hypothesis is correct, we would expect the post-treated ICE cells to display characteristics of cells from old mice. One of the most robust and reproducible effects of aging is an increased sensitivity to DNA damaging agents including camptothecin, etoposide, and hydrogen peroxide (Li et al., 2016; Mapuskar et al., 2017; Miyoshi et al., 2006). The post-treated ICE cells were significantly more susceptible than Cre controls to DNA damage caused by the above agents, based on increased numbers of γH2AX and 53BP1 foci (**Figure S1K and S1L**).

Another hallmark of aging is a decrease in Lamin B1 that can promote cellular senescence, as indicated by SA-β-Gal activity and markers such as IL6, Ccl2, Ccl20, LINE-1 and IAP (Freund et al., 2012; Shah et al., 2013). At later time points of post-treatment (120-168 hrs), ICE cells had lower Lamin B1 levels (**Figure S1M and S1N**) and increased cellular senescence (**Figure 1F-1H**). Based on extensive whole-genome sequencing, there was no difference in mutation frequency at canonical, non-canonical (Wittmayer et al., 1998), or ~100,000 random sites in Cre and ICE cells after cutting and recovery for 96 hours (**Figure S1H-SJ**). Together, these data show ICE cells are epigenetically aged without a discernible increase in mutations.

8

252

The ICE system induces non-mutagenic cuts *in vivo*

To test the ICE system *in vivo*, we performed whole-body I-*Ppo*I induction for three weeks in 4-6

month-old mice by providing a modified AIN-93G purified rodent diet containing tamoxifen (360

mg/kg) and mice were assessed for another 10 months (**Figure 1I**). The extent of STOP

cassette removal was similar in muscle (67%), liver (71%), hippocampus (61%) and cortex

(72%) (**Figure S3A**). HA-I-*Ppo*I, γH2AX and eGFP were detectable during tamoxifen treatment

but not post-treatment in all tissues tested (**Figure S3B-S3E**).

To assess the location and extent of I-*Ppo*I cutting, we used a modified end-capture qPCR

assay (Chailleux et al., 2014) that used a biotinylated oligo with the overhang 5'-TTAA-3' to

capture I-*Ppo*I cut DNA (**Figure 1J**). In skeletal muscle, liver and kidney, the *Tmem56* intron and

the 28S I-*Ppo*I site were cut during tamoxifen treatment and no cutting was detectable 1- and

10-months post-treatment (**Figure 1K and S3F**). At the rDNA, in post-treated ICE muscle and

brain, there was no evidence of residual cutting (**Figure S2K**), change in copy number (**Figure**

S2P), 28S expression levels (**Figure S2Q**) or protein synthesis (**S2N and S2O**).

In 1-month post-treated ICE muscle, no differences in mutation frequency were detected, either

at canonical or non-canonical I-*Ppo*I recognition sites (Wittmayer et al., 1998), or across the

genome, based on whole genome sequencing (**Figure S3G-S3I**). Together, these data show

that the ICE system induces specific DNA breaks that are repaired without leaving mutations or

eliciting short-term, deleterious effects on cells or mice.

The ICE system phenocopies aging *in vivo*

As mice age, they undergo characteristic physical and physiological changes, including

alopecia, hair greying, kyphosis, decreased body weight, decreased motion in the dark phase,

and reduced respiration during the day as they utilize fat rather than carbohydrate as an energy

source (Ackert-Bicknell et al., 2015; Harkema et al., 2016; Houtkooper et al., 2011; Koks et al.,

2016). If the RCM hypothesis is correct, a short period of induction of I-*Ppo*I should introduce

age-related epigenomic changes that accelerate some, if not all, aspects of aging (**Figure 1I**

and 2A). As negative controls for the ICE mice, we assessed identically treated WT, Cre, and I-

9

283   *Ppo*I littermates (**Figure S1A**). During the three-weeks of I-*Ppo*I induction, there were no

284   detectable differences between ICE mice and controls in terms of behavior, activity, or food

285   intake. After one month, however, there were visual differences in the ICE mice compared to the

286   controls, such as slight alopecia and loss of pigment on the feet, tail, ears and nose, resembling

287   middle-aged WT mice (Liu et al., 2019; Nishimura et al., 2005) (**Figure 2B**). By the 10-month

288   post-treatment time-point, none of the controls but all of the ICE mice exhibited classic features

289   of old age, including reduced body weight and fat mass, independent of food intake (**Figure 2B-**

290   **2E and S4A-S4E**), a lower respiratory exchange ratio (RER) during the day (**Figure 2F and**

291   **S4F**) and decreased motion in the dark phase (**Figure 2G**).

292

293   To provide a longitudinal, quantitative measure of health, we utilized a mouse frailty index (FI),

294   which combined 31 parameters, including body weight, temperature, coat condition, grip

295   strength, mobility, vision and hearing (Whitehead et al., 2013). At the 1-month post-treatment

296   time point, there was no significant difference in FI score of ICE mice and controls. By the 10-

297   and 12-month time points, however, the FI scores of the ICE mice were substantially higher than

298   controls, closer to 24 month-old WT mice (p=0.0006 and <0.0001, respectively) (**Figure 2H**).

299   We also noted accelerated kyphosis and a loss of cortical bone thickness and trabecular bone

300   density in the inner layer (Ferguson et al., 2003; Katzman et al., 2010), both common features of

301   mouse aging (**Figure 2I and 2J**).

302

303   To determine if ICE mice mimicked the histological changes seen during aging, we assessed

304   kidney and skin, two tissues that undergo well characterized changes during aging that are

305   similar to humans. In the kidney, major age-related changes include an increase in damage of

306   the glomerular basement membrane and the loss of podocytes that line the glomerular capillary

307   (Roeder et al., 2017). Compared to Cre controls, the kidneys of 10-month post-treated ICE mice

308   had a lower percentage of samples that were scored as healthy and normal (1+) and a higher

309   percent that were scored as damaged (2+ and 3+) for both the outer cortex (OC) and

310   juxtamedullary (JM) glomerulus, along with a greater loss of podocytes (**Figure 2K-N**). Based

311   on the level of the alpha isoform of smooth muscle actin (αSMA), a well-described epithelial to

312   mesenchymal transition (EMT) marker, the glomerular parietal epithelial cells (PECs) of ICE

10

313   mice experienced a greater EMT, a characteristic of aged kidneys (Roeder et al., 2015) (**Figure**

314   **2O and P**).

315

316   The subepidermal thickness of skin typically increases until middle age then declines rapidly,

317   along with hair greying due to a loss of KIT/CD117-positive melanocyte stem cells (Gomes et

318   al., 2013; Matsumura et al., 2016; Nishimura et al., 2005). These features were accelerated in

319   the ICE mice, including hair greying and a loss of subepidermal thickness and fewer

320   KIT/CD117-positive melanocytes (**Figure S4J-S4M**). Together, these data indicate that the

321   induction of non-mutagenic DSBs phenocopies age-associated physiological changes.

322

323   **ICE mice phenocopy brain aging**

324   One of the main hallmarks of mammalian aging is a decline in the function of the central

325   nervous system, leading to a loss of motor coordination and cognition (**Figure 3A**) (Johnson et

326   al., 2018; Ungvari et al., 2017). During aging, mice move less when the light are off (dark phase)

327   and have a characteristic loss of gait coordination. Relative to Cre controls, the ICE mice moved

328   ~50% less in the dark phase (**Figure 3B**) and, based on swing and stance times, gait

329   coordination was impaired (**Figure S4N-S4P**).

330

331   The hippocampus is critical for spatial and memory consolidation, the function of which declines

332   predictably with age in mice and humans (Gallagher et al., 2010; Miller and O'Callaghan, 2005;

333   Park and Reuter-Lorenz, 2009). In the fear-conditioning paradigm, the short-term memory of

334   mice is measured by placing them in specific contexts and inducing a mild electric shock on Day

335   1, which is typically recalled on Day 2 and expressed as a freezing response. The immediate

336   freezing response was similar between young and old mice (6- vs. 24- and 30-month) on Day 1,

337   but on the second day, 75% of the young mice compared to <40% of old mice froze, indicating

338   the old mice had a reduced ability to recall the context from the day before (**Figure 6C-E)**. A

339   similar difference was seen when comparing Cre and ICE mice at the 10-month post-treatment

340   time point (16 months of age), with >40% of the Cre controls responding to the context on the

341   second day, compared to only about 24% of the ICE mice (**Figure 6D-E**).

342

11

343 Another measure of hippocampal function and long-term memory is the Barnes maze test. Over

344 five days, mice learn to identify the location of a hiding box then, 7 days later, mice are re-tested

345 for their ability to recall the location of the hiding box. The memory recall of ICE mice was about

346 half that of age matched Cre controls, similar to the recall of 24 month-old WT mice (**Figure 6F**

347 **and 6G**).

348

349 Within the central nervous system, astrocytes and microglia are critical mediators of the innate

350 immune response. As mammals age, the innate immune system becomes hyper-activated and

351 the number of activated microglia and astrocytes increases (Baruch et al., 2014; Norden and

352 Godbout, 2013). In the WT cohort, the hippocampi of 24 month-old mice had greater numbers of

353 activated microglia and astrocytes compared to 6-month-old mice, consistent with previous

354 reports (Baruch et al., 2014). Paralleling normal aging, the ICE mice had greater numbers of

355 activated microglia (1.6x) and astrocytes (3.5x) than the Cre controls (**Figure 6H-6K**). Together,

356 these data indicate that ICE mice experience an acceleration of brain inflammation and memory

357 loss, reminiscent of normal aging.

358

359 **ICE mice phenocopy muscle aging**

360 Age-related changes to skeletal muscle include decreases in exercise endurance, strength,

361 muscle mass, vascularization and mitochondrial function (Das et al., 2019; Demontis et al.,

362 2013) (**Figure 4A**). At 16 months of age, compared to the negative control mice, ICE mice had

363 significantly less muscle mass (**Figure 4B**), reduced endurance (**Figure 4C**), and greater lactate

364 levels post-exercise, similar to WT mice at 30 months of age (**Figure S5A**). Grip strength of ICE

365 mice was also lower than age-matched Cre controls (**Figure S5B**). At the cellular level,

366 hallmarks of muscle aging include reduced ATP and mitochondrial DNA copy number,

367 increased mitochondrial area, and alterations in subsarcolemmal and intermyofibrillar

368 mitochondrial morphology (Demontis et al., 2013; Leduc-Gaudet et al., 2015). The ICE mice but

369 not the negative controls displayed all of these changes at the 10-month post-treatment time

370 point, resembling 20 to 24 month-old wild type mice (**Figure 4D-4F and S5C-S5F**).

371

372 Another well-known hallmark of muscle aging is a decrease in the abundance of cytochrome

373 oxidase, a component of complex IV in the OXPHOS system (Wenz et al., 2009). At the 10-

12

374 month post-treatment time point the ICE mice had 6-fold fewer COX-positive myofibers,

375 paralleling the difference between 6 and 24 month-old WT mice (**Figure S5G and S5H**).

376

377 One of the most obvious changes during mammalian aging is the loss of muscle

378 microvasculature (Das et al., 2019). The capillary to fiber ratio in skeletal muscles of ICE mice

379 was about half that of the Cre mice, similar to ratio between 6 and 20 month-old mice (**Figure**

380 **4G and 4H**). In skeletal muscle, a loss of silencing at repetitive elements and the transcription of

381 retrotransposons was also seen in ICE mice, paralleling what occurs during normal aging (De

382 Cecco et al., 2019; Oberdoerffer et al., 2008) (**Figure S5I**). We did not significant cardiac

383 changes in the ICE mice, except for thinner left ventricular (LV) posterior walls, implying

384 possible dilated cardiomyopathy (**Figure S5K and S5L**).

385

386 **ICE mice undergo accelerated epigenetic aging**

387 To provide a more quantitative assessment of biological age, we compared gene expression

388 and DNA methylation (DNAme) patterns of ICE mice. In skeletal muscle, genes that were

389 significantly dysregulated in ICE mice were positively correlated with changes in wild type 24

390 month-old mice (**Figure 4I, 4J, S5M-S5O and Table S2**). Notable examples were *Cdkn1a*

391 (Cyclin Dependent Kinase Inhibitor 1A or p21), a mediator of p53-mediated cellular senescence

392 (Beggs et al., 2004; Choudhury et al., 2007; Welle et al., 2004), *Myl4* (Myosin light chain 4),

393 which encodes an embryonic form of myosin that is upregulated in aged mouse muscle (Lin et

394 al., 2018), *Nlrc5* (NLR family CARD domain containing 5), which inhibits NF-κB activation and is

395 one of the most significantly hypomethylated genes in centenarians (Zeng et al., 2018), and

396 *Mrpl55* (mitochondrial ribosomal protein L55), which encodes a 39S mitochondrial ribosomal

397 gene whose methylation status is associated with life expectancy (Weidner et al., 2014; Zhang

398 et al., 2017).

399

400 DNAme clocks serve as a robust biomarker of biological age in mammals (Hannum et al., 2013;

401 Horvath, 2013; Petkovich et al., 2017; Weidner et al., 2014). To assess the relative DNAme age

402 of the ICE mice, we developed DNAme clocks for skeletal muscle and blood (**Figure S6A-S6D**).

403 Reduced-representation bisulfite sequencing (RRBS) on 79 skeletal muscle and 118 whole

404 blood samples identified 915 age-associated CpG loci for a blood panel and 2,048 CpG loci for

13

a multi-tissue panel. Targeted bisulfite-sequencing libraries using a simplified whole-panel amplification reaction method (SWARM) was then used to assess DNA methylation changes at >2,000 CpG sites sequenced to >2,500x coverage. We used 61 WT muscle and 29 WT blood samples from male and female C57BL/6 mice aged 2 to 30 months to define the training set (**Figure S6A-S6D**) and selected 2,048 multi-tissue clock CpGs by ElasticNet regression model with CpG sites, with at least 300 reads in all samples. The epigenetic age for muscle and blood samples was calculated as: epigenetic age = $inverse.F(b_0 + b_1 CpG_1 + \cdots + b_n CpG_n)$, where the b are coefficients obtained from the trained model with b_0 being the intercept and CpG are methylation values of the loci.

Within the training dataset, the epigenetic age derived from the weighted sum of DNA methylation levels of age-modulated CpG sites was highly correlated with the chronological age of the individual samples, with $R^2 = 0.995$ and 0.992 for the muscle and the blood clock, respectively (**Figure S6A, S6C and Table S3**). For validation, 18 muscle and 90 blood samples aged 2 to 30 months were used for the testing dataset (**Figure S6B, S6D and Table S3**). The clocks performed well in the validation data sets with $R^2 = 0.915$ and 0.944 for the muscle and blood clocks respectively, indicating that both were able to accurately estimate age using two completely independent datasets. Across the genome, 40% of the DNAme clock sites were in CpG islands, 30% were in introns, 20% were in coding sequences and less than 5% were in enhancers or 3' UTRs. There was no overlap between the DNAme sites and known I-*Ppo*I recognition sequences (**Figure S6E**).

Using these two mouse clocks, the rate of epigenetic aging was estimated to be ~50% faster in the ICE mice than Cre controls (p<0.0001), closely paralleling the accelerated age of cultured fibroblasts from ICE mice (**Figure 4K**). Delta age (Δ age), the difference between chronological and epigenetic age, was greater in the ICE mice compared to Cre controls for both the muscle and the blood clock (**Figure 4L and 4M**).

DNA breaks alter the epigenetic landscape
Having established that non-mutagenic DSBs accelerate phenotypes of aging and the DNA methylation clock in cell culture and in mice, we sought to understand the underlying

14

436 mechanisms. We first assessed global epigenetic changes in the aged ICE cells. Using mass

437 spectrometry, a total of 46 different post-translational histone modifications were quantified.

438 Three major changes were observed: a decrease in H3K27ac and H3K56ac, and an increase in

439 H3K122ac (**Figure 5A, S6F**). Interestingly, these marks are linked to aging. For example,

440 H3K27ac and H3K56ac are decreased in many human immune cell types at the single cell level

441 (Cheung et al., 2018; Dang et al., 2009) and reduced levels of H3K122ac extend the lifespan of

442 yeast (Sen et al., 2015). Chromatin immunoprecipitation followed by DNA sequencing (ChIP-

443 seq) was performed on ICE and Cre control cells, with a spike in control of *Drosophila* S2+ cells

444 (Orlando et al., 2014). Relative to Cre controls, ICE cells had less chromatin-bound H3K27ac

445 and H3K56ac (2% and 5%, respectively) (**Figure S6G and Table S4**).

446

447 Based on ChIP-seq and ATAC-seq, H3K27ac was generally enriched in accessible chromatin

448 regions, consistent with the known association of H3K27ac with active promoters and

449 enhancers (Heinz et al., 2015; Klemm et al., 2019). In post-treated ICE cells, regions with higher

450 accessibility lost H3K27ac, and those with lower accessibility gained it (**Figure S6H**). An

451 analysis of the aggregated H3K27ac signals that changed in the ICE cells showed that loci with

452 the high peak intensities tended to lose the most signal and vice versa, consistent with a

453 smoothening of the H3K27ac landscape, with no obvious changes at the I-*Ppo*I recognition sites

454 (**Figure S6I**). A smoothening was also seen across H3K27ac peaks genome-wide or in the top

455 or bottom 40% quantile of H3K27ac signals, such that the ICE:Cre ratio of H3K27ac signals was

456 inversely correlated with basal H3K27ac signals (**Figure 5B and S6J**).

457

458 **Erosion of the epigenetic landscape disrupts developmental genes**

459 Gene Ontology (GO) analysis of the gene set with significant increases in H3K27ac and

460 H3K56ac, and decreases in H3K27me3 indicated that developmental processes were disrupted

461 in the ICE cells. Within the top 20 processes, half of them were involved in developmental

462 processes, including pattern specification, organ identity, tissue and organ development (**Figure

463 5C, Table S5 and S6**). Consistent with RCM being an ancient stress response, loci that

464 experienced a decrease in H3K27ac were predominately involved in stress responses,

465 chromatin structure, metabolism, cellular component organization, nucleobase synthesis, and

466 DNA repair (**Table S6**).

15

467

468 To gain insights into what might be driving epigenetic changes to developmental genes, the

469 intersection of the ChIP-seq datasets in **Figure 5C** was cross-referenced with the TreeFam

470 database, which provides orthology and paralogy predictions of gene families (Li et al., 2006;

471 Ruan et al., 2008) (**Figure 5D**). At the intersection of all three data sets were two gene families,

472 both comprised of homeobox (*Hox*) genes encoding developmental transcription factors that

473 specify body plan and the head-tail axis during embryogenesis. In the epigenetically aged ICE

474 cells, all of the *Hox* gene clusters (Hoxa-d) had significant alterations in peaks of H3K27ac,

475 H3K56ac and H3K27me3 coincident with changes in mRNA levels (**Figure 5E and 5F**).

476

477 Genes in the *Hoxa* cluster were of particular interest in the context of RCM because they are

478 known to be regulated by the yeast Sir2 homolog SIRT1 and mediate stress and DNA repair

479 responses (Oberdoerffer et al., 2008; Schworer et al., 2016; Singh et al., 2013). From *Hoxa1* to

480 *Hoxa6*, levels of H3K27ac and H3K56ac decreased in ICE cells, while from *Hoxa9* to *Hoxa13*

481 they increased, coincident with opposing changes in H3K27me3 and corresponding changes in

482 mRNA levels (**Figure 5F and S6K**). These data add further evidence that repeated cycles of

483 DSB repair erode chromatin boundaries and smooth out the epigenetic landscape.

484

485 To test if the effects of DSB repair were specific to I-*Ppo*I, we isolated MEFs from a mouse

486 strain with an inducible homing endonuclease from budding yeast called I-*Sce*I, which cuts at

487 ~18 cryptic (non-canonical) sites in the mouse genome, far from the vicinity of I-*Ppo*I sites

488 (Chiarle et al., 2011). Paralleling the effects of I-*Ppo*I on post-recovery gene expression, I-*Sce*I

489 altered mRNA levels of genes in the *Hoxa* cluster. Thus, the effect of DSBs on Hoxa expression

490 does not depend on where the DNA breaks occur (**Figure S6L**).

491

492 **DSB repair alters spatial chromatin contacts**

493 The spatial organization of chromatin, including long-range interactions between regulatory

494 elements, plays a key role in the control of epigenetic information (Kundu et al., 2017; Narendra

495 et al., 2015; Schoenfelder et al., 2015), the maintenance of cellular identity (Gorkin et al., 2014)

496 and aging (Zirkel et al., 2018). High-resolution spatial chromatin contacts between promoters

497 and enhancers was assessed by mapping the H3K27ac-accociated chromatic contacts

16

498 (HiChIP.) The higher sensitivity and selectivity of HiChIP identified numerous chromatin contacts

499 disordered in the epigenetically aged ICE cells. H3K27ac HiChIP revealed aberrant spatial

500 contacts between *Hoxa* promoters and distal enhancer elements while topologically associated

501 domains (TADs) remain unchanged in Hi-C (**Figure 5G**). Posterior *Hoxa* gene promoters (*Hoxa*

502 9-13) formed new contacts with active enhancers (H3K27ac+) present in an adjacent TAD with

503 a concomitant increase in mRNA levels indicating weakened insulation and disordered

504 promoter-enhancer (P-E) communication. This is the first evidence that faithful DNA repair alters

505 multiple layers of epigenetic information, including spatial chromatin contacts, chromatin

506 insulation, and P-E communication.

507

508 **Epigenetically aged cells lose the ability to maintain cellular identity**

509 The smoothening of the epigenetic landscape across the genome of ICE cells and the fact that

510 the most prominent epigenetic and transcriptional changes were in genes involved in

511 developmental and cellular differentiation pathways, prompted us to test if the identity of the ICE

512 fibroblasts had been impacted. An assessment of GO processes or tissue types of

513 transcriptional profiles that overlap genes with decreased H3K27me3 revealed that 4 and 6 out

514 of the top 10 were involved in neuronal processes and tissue types including cerebral cortex,

515 spinal cord, and cerebellum (**Figure 6A and 6B**). H3K27me3 signals were lower across

516 promoter regions of genes that specify neuronal fate, including the *Neurod1* gene, which lies

517 within a cerebellum SE, and the neurofilament gene *Nefh,* which maintains neuronal caliber

518 (**Figure 6C**).

519

520 These findings indicated that epigenetically aged MEFs might have been shifting away from a

521 fibroblast lineage and towards a more neuronal landscape. If so, they should be primed to

522 differentiate into neuronal cell types. To test this, Cre and ICE cells were subjected to a

523 standard 17-day neuronal reprogramming protocol that uses small molecules to induce neuronal

524 genes and inactivate fibroblast genes such as *Col1A1* (Li et al., 2015) (**Figure 6D and 6E**).

525 During reprogramming, *Neurod1* and *Nefh* were 8-15-fold more easily derepressed in ICE MEFs

526 than in Cre control cells (**Figure 6E**). Compared to the Cre controls, 2.5-fold more ICE-derived

527 neurons were created along with 4-fold higher levels of Tuj1, a canonical neuronal cell marker

528 (**Figure 6F and 6G**) indicating that their identity as fibroblasts might have been compromised.

529

Cellular identity changes in ICE mice

530 To test whether DSBs accelerate the loss of tissue identity *in vivo*, we performed H3K27ac
531 ChIP-seq on skeletal muscle of ICE mice that were treated 10-months earlier. To assess if the
532 muscle of ICE mice had taken on a signature of another cell type, we compared the dataset of
533 regions with altered H3K27ac signals to the epigenome roadmap, a consortium of human
534 epigenomic data from different cell types and tissues (Roadmap Epigenomics et al., 2015).
535 Regions with lower H3K27ac ($p < 0.01$) in Cre vs. ICE showed the strongest enrichment for
536 muscle tissue signatures ($p = 9.0 \times 10^{-8}$) while regions with higher H3K27ac showed an
537 enrichment for immune cell enhancers ($p = 9.3 \times 10^{-28}$) (**Figure 6H and S6M**). Of the regions that
538 gained H3K27ac, there was overlap with super-enhancer regions from immune cell types and
539 with regulatory regions involved in developmental processes and immune cell activation (**Figure
540 S6N**).

542

543 Of the top 20 processes that were increased in ICE muscle, all were also elevated in old
544 wildtype mice, indicating the ICE mice closely parallel changes seen in normal aging (**Figure
545 6I**). Because ChIP-seq data is not influenced by a small portion of infiltrated cells, we infer that
546 the muscle tissue in post-treated ICE mice had shifted more towards an immune signature. The
547 observed increased overlap of inflammation-related gene expression patterns and chromatin
548 changes in old mice is consistent with recently published data (Benayoun et al., 2019). Together
549 with the neuronal priming of ICE cells and increased EMT in the ICE kidney, these analyses
550 indicate that the induction of non-mutagenic DSBs accelerates the DNA methylation clock and
551 induces many of the same changes to chromatin, gene expression, and cellular identity that
552 occur in normal mouse aging.

553

Epigenetic reprogramming restores a youthful transcriptome

554 To gain insights into a causal role of epigenetic alterations in aging, we tested whether the
555 altered epigenome of ICE cells or old WT cells could be recovered while maintaining cell
556 identity. If so, this would essentially rule out mutations as a cause of the phenotype and provide
557 strong evidence that epigenetic alterations are a cause of the aging phenotype. The cyclic
558 expression of Yamanaka factors *Oct4*, *Sox2*, *Klf4* and *Myc* (OSKM), which are known to induce

18

560 somatic cell reprograming (Takahashi and Yamanaka, 2006), alleviates symptoms and extends

561 lifespan of a progeroid mouse (Ocampo et al., 2016). We recently reported that expression of

562 OSK reverses aging *in vitro* and *in vivo*, and safely restores youthful epigenetic information to

563 reset gene expression patterns and restore the vision of glaucomatous and aged mice (Lu et al.,

564 2020).

565

566 To induce OSK in ICE cells, we utilized an AAV system (AAV-DJ) under the tight control of

567 doxycycline (Dox)-inducible promoter (**Figure S7A and S7B**), which, after 2 days of Dox

568 treatment, induced OSK in a dose-dependent manner without activating the endogenous

569 pluripotency gene *Nanog* (**Figure S7C-S7E**). After 6 days of OSK induction, age-associated

570 mRNA changes were reversed, including mRNAs for *Lmnb1*, *Chaf1b*, *Hoxa* and canonical

571 histone genes (**Figure 7A-7C, S7F and S7G**). Old fibroblasts derived from OSK transgenic mice

572 showed a similar restoration of youthful mRNA levels (**Figure 7D-7F, S7H and S7I**).

573

574 The visual system of mammals is an excellent system to study the effects of aging and its

575 reversal *in vivo* (Lu et al, 2020). We first tested if ICE mice undergo changes to the visual

576 system that resemble normal mice. Similar to old WT mice (Calkins, 2013; Samuel et al., 2011;

577 Wolf et al., 2000), there was significantly more lens opacity in the ICE mice compared to Cre

578 controls (**Figure S7J-S7L**). Like cells in the lens, retinal ganglion cells that reside in the

579 innermost retinal layer and form the optic nerve (**Figure 7G**) are particularly vulnerable to

580 mechanical and metabolic stress during aging (Downs, 2015). Paralleling what is typically seen

581 in 24 month-old wild type mice, the ICE mice had significantly fewer optic nerve axons in the

582 myelinated region (**Figure 7H-7K**). Ectopic expression of OSK in RGCs (**Figure 7L**) restored

583 the mRNA levels of 86% of genes that were altered by aging. Consistent with our *in vitro* data, 7

584 of the top 10 upregulated processes in the RGCs of 12 month-old mice were involved in

585 development (**Figure 7M**), the majority of which (87%) were restored by OSK (**Figure 7N**).

586

587 **DISCUSSION**

588

589 Studies in simple organisms such as yeast and flies indicate that changes to the epigenome are

590 a cause of aging (Imai and Kitano, 1998; Jiang et al., 2013; Mills et al., 1999; Oberdoerffer et al.,

19

591 2008). But whether this process occurs in mammals is not known. During mammalian

592 development, cell types are specified by the establishment of specific transcriptional networks

593 and chromatin landscapes, such that cells land in valleys depicted by the Waddington

594 epigenetic landscape (Waddington, 1957). Why and how mammals lose epigenetic information

595 over time, and whether this process is an underlying cause of aging, are currently debated. The

596 results in this study indicate repeated disruptions to the epigenome, such as DSBs, cause the

597 landscape to erode and the epigenetic clock to advance. As erosion proceeds, cells move

598 towards adjacent valleys, losing their identity. We envisage that this process, which we call "ex-

599 differentiation," is a major driver of aging and its various hallmarks.

600

601 Through a series of complementary *in vitro* and *in vivo* experiments, we show that non-

602 mutagenic DNA breaks alter the structure of the epigenome in ways that are reminiscent of

603 aging, including a smoothening of the chromatin landscape, disordered spatial chromatin

604 contacts and a loss of cellular identity. The data strongly argue that the process of DSB repair,

605 even if it doesn't lead to a mutation, alters the epigenome and accelerates aging at

606 physiological, histological, and molecular levels, including an acceleration of the epigenetic

607 clock, and that it can be restored by epigenetic reprogramming. We regard these results as

608 strong evidence that epigenetic drift, driven by the DSB repair response are a universal cause of

609 aging in eukaryotes (**Figure 7O**). As far as we are aware, these studies identify the first

610 molecular driver of epigenetic changes during aging *in vivo* and the first set for convincing

611 evidence that they drive the aging process.

612

613 Traditionally, the process of DNA damage checkpoint activation and DNA repair has been

614 studied using mutagens or radiation doses that cause DNA damage substantially above

615 background levels. The ICE system allows us to create DSBs at levels at more natural levels,

616 only a few-fold above background, thus avoiding overt DNA damage signaling response, cell

617 cycle arrest, aneuploidy, mutations, or cellular senescence. Initially, no profound changes at the

618 physiological or molecular levels were observed in the treated ICE mice. Indeed, the epigenetic

619 clock did not initially advance. Over the course of the next 10 months, however, every tissue we

620 examined had deteriorated and developed signs of aging. This observation suggests that

621 molecular changes occurring during or shortly after the treatment trigger an advancement of the

20

622 epigenetic clock many months later. We don't yet know what these triggers are, but we

623 hypothesize that might be alterations in DNA, chromatin, or transcriptional networks that initiate

624 a feed-forward cascade of deleterious events. Future work will be aimed at identifying these

625 cascades.

626

627 In humans, there is an abundance of evidence linking DNA damage to aging, including cancer

628 chemotherapy, radiation exposure, smoking, and progeroid diseases such as Werner and

629 Cockayne's syndrome (Hofstatter et al., 2018; Horvath and Levine, 2015; Maccormick, 2006;

630 Nance and Berry, 1992; Salk et al., 1985). Similarly, in model organisms, deficiencies in DNA

631 repair, such as Ercc1, BubR1, Ku70, and Xpd mutant mice, also appear to accelerate aspects of

632 aging (Carrero et al., 2016; White and Vijg, 2016). But mutation accumulation as a main cause

633 of aging has been hard to reconcile with other findings, such as the ability to clone mammals

634 from adult cells and that nuclear mutations are not only rarer than would be expected in old

635 tissues, they can occur with high frequency without causing signs of aging (Dolle et al., 2006;

636 Dolle et al., 1997; Narayanan et al., 1997).

637

638 By causing DNA damage without causing mutations in cells and in mice, we provide strong

639 evidence that it is the cell's reaction to DNA breaks, rather than actual mutations, that drives the

640 aging clock. This idea is particularly appealing because it explains why aging proceeds through

641 a predictable series of molecular and physiological changes, even though DNA damage can

642 occur anywhere in the genome. These data also help explain why DSB repair efficiency

643 correlates with longevity in diverse species, but not other types of DNA repair such as NER and

644 BER (Brown and Stuart, 2007; Tian et al., 2019). In our model, DSBs are a special type of

645 damage that potently induces epigenetic change. Because transcription-coupled DNA repair

646 (TCR) defects in ERCC1 mutant mice also mimic aging (Niedernhofer et al., 2006), it will be

647 interesting to determine whether TCR also induces an RCM response, epigenomic changes,

648 and acceleration of the DNAme clock. Given that ERCC1 plays an indispensable role in the

649 repair of DSBs containing DNA secondary structures, including AT-rich DNA sequences at

650 fragile sites and G-quadruplexes (Li et al., 2019), perhaps the fundamental underlying

651 mechanism of the ICE and ERCC1 mutant phenotype is the same.

652

21

653 Individuals treated with DSB-generating agents, such as chemotherapy, X-rays, and gamma
654 radiation, are known to experience an acceleration of aging (Garrett-Bakelman et al., 2019;
655 Maccormick, 2006; Richardson, 2009). In this study, low levels of DSBs were surprisingly
656 impactful, even months later, raising the specter that very low doses radiation and even DNA
657 editing enzymes may have deleterious long-term effects on the epigenome and tissue function.
658
659 The negative impact of DSBs on the epigenome also raises the question why RCM evolved in
660 the first place. We hypothesize it is an ancient system that places cells in a state of high-alert
661 while DSB repair is carried out. At the molecular levels, DSBs induce relocalization of
662 transcription factors and chromatin modifying proteins to the DSB site, thereby inducing a
663 coordinated DNA damage response at the transcriptional level while repair takes place. Factors
664 known to relocalize include the histone deacetylases SIRT1, SIRT6, HDAC1, and poly-ADP
665 ribose polymerase, PARP1 (Dobbin et al., 2013; Mao et al., 2011; Oberdoerffer et al., 2008).
666 After repair, the majority of the original chromatin structure is restored, but repeated triggering of
667 the response disrupts youthful gene expression patterns and can de-silence retrotransposons
668 that are held at bay by SIRT1 and SIRT6 (De Cecco et al., 2019; Oberdoerffer et al., 2008;
669 Simon et al., 2019), analogous to erosion of the Waddington landscape or accumulation of
670 epigenetic noise. Why the epigenetic clock is advanced by DSBs remains a mystery, but one
671 possibility is that DSBs cause the relocalization of ten eleven translocation enzymes (Tets) or
672 DNA methyltransferases (DNMTs) to DNA breaks, leading to specific changes in DNA
673 methylation patterns over time (Field et al., 2018).
674
675 The dysregulation of developmental genes that we observed in ICE cells, which included the
676 *Hox* loci, has previously been reported in aged hematopoietic stem cells (Florian et al., 2013),
677 dermal fibroblasts (Salzer et al., 2018) and muscle satellite cells (Brack et al., 2007). Why DSBs
678 preferentially disrupt developmental pathways is not yet clear but one possible reason is that
679 genes regulated by transient transcriptional networks are more easily reset than developmental
680 genes, which are under multiple layers of regulation. The coordination of DSB signaling with
681 cellular identity appears to be an ancient mechanism, one that may have evolved in embryonic
682 cells to deal with an abundance of potentially lethal DSBs that occur as a result of rapid DNA
683 replication. This would explain why developmental regulators, such as *Wnt* and *Hox* genes, also

22

684 mediate DSB repair (Feltes, 2019; Rubin et al., 2007; Zhao et al., 2018). As to the role of DNA

685 methylation, a survey of 128 mammalian species discovered numerous conserved CpGs

686 proximal to developmental genes, such as *Hox* and *Pax*, indicating that these sites may play a

687 functional role in aging (Lu et al., 2021).

688

689 We cannot rule out that some of the effects we see in the ICE mice are due to cutting of the

690 rDNA locus. Indeed, rDNA instability is a known cause of aging in yeast and the nucleolus size

691 predicts lifespan (Sinclair et al., 1997; Tiku et al., 2017). Given that we saw no evidence of rDNA

692 mutations, changes in rRNA levels or protein translation, and the observation that the I-*Sce*I

693 enzyme generated a similar gene expression pattern, alterations to the rDNA are unlikely to

694 explain the ICE phenotype. It will be interesting to test whether interventions that prevent DSBs

695 increase the stability of the epigenome and extend lifespan.

696

697 The duality of decreased silencing and increased DNA repair was first detected in budding

698 yeast, in which the derepression of silent mating-type genes increases DNA repair efficiency

699 (Lee et al., 1999) but constitutive derepression causes a loss of cell identity and sterility, a

700 hallmark of yeast aging (Smeal et al., 1996). This is a clear example of antagonistic pleiotropy,

701 in which an adaptive process that promotes survival in young individuals disrupts homeostasis

702 at an advanced age where the influence of natural selection falls to near zero.

703

704 Besides facilitating a new understanding of epigenetic change during aging, the ICE system

705 may overcome a variety of other research challenges. Short-lived species such as rodents have

706 proven to be poor models of many human age-related diseases. ICE mice, however, may solve

707 this problem by accelerating the epigenetic age of the mice. Indeed, some of the phenotypes of

708 the ICE mice, such as retinal degeneration, loss of vascularity and memory loss, closely

709 resemble aging in humans. And by accelerating aging in specific tissues, it will be possible to

710 test how much individual organ systems contribute to aging. By introducing the ICE system into

711 human iPSCs, it should be possible to generate human tissue cultures and organoids that

712 recapitulate human diseases of aging better than those that are currently available.

713

714

23

AUTHOR CONTRIBUTIONS

J.-H.Y., L.A.R. and D.A.S. initiated and designed the project. J.-H.Y. performed most experiments, analyzed data and wrote the manuscript. A.R.P., J.-H.Y., P.T.G., D.L.V., J.A. and C.S. analyzed ChIP-seq and RNA-seq data. E.L.S., J.-H.Y. and M.H. analyzed WGS data. M. Blanchette, J-H.Y., E.M.M., M. Bhakta, D.L.V., B.O., and R.E.G. performed and analyzed Hi-C and HiChIP data. M.H., J.-H.Y., J.A.A., G.C., J.M.R., M.S.B., Y. L., X. T., A.D., S.T., N.G., A.-M.B., S.J.B., S.J.M., L.S., Y.M., E.K.N., G.F.M. H.W., J.G.S., A.E.K., M.A.R., C.E.S., J.W.P., M.C. and S.J.S. conducted mouse phenotype analyses. Z.D., C.X., B.A.G., J.-H.Y. and S.L.B. performed and analyzed MS. M.V.M., V.N.G. Y.C.C., W.G., J.-H.Y., J.A.A., and X.Y. calculated epigenetic ages. N.S.W., M.G.-K., T.C.J and B.R.K. assessed eye phenotypes. J.A.K. and J.M.S. measured activation of repetitive sequences. K.T., C.M.P., L.Z., R.M. and A.J.W.

24

provided advice and assistance with experiments. P.O. and D.A.S. designed the I-*Ppo*I

construct and integrated the construct into ES cells to generate I-*Ppo*I mouse. L.A.R. initiated

ICE mouse study and provide advice and assistance throughout. D.A.S. supervised the project

and wrote the manuscript.

DECLARATION OF INTERESTS

25

Figure 1. The Inducible Changes to the Epigenome (ICE) system

(A) Schematic of the ICE system based on a tamoxifen-inducible I-*Ppo*I endonuclease.

(B and C) γH2AX foci in DAPI-stained nuclei of MEFs from ICE mice and Cre controls after tamoxifen (4-OHT, 0.5 μM) treatment. Scale bar, 10 μm. Two-way ANOVA-Bonferroni.

(D) qPCR analysis of DNA cutting at I-*Ppo*I canonical sites. One-way ANOVA-Bonferroni.

(E) Epigenetic age of 96-hour post-treated ICE cells. All DNA methylation sites (left) and DNA methylation sites post-batch effect correction (right). Mann-Whitney U test.

(F and G) Images and quantification of SA-β-Gal staining of post-treated ICE and Cre cells. Two-tailed Student's *t* test.

(H) mRNA levels of genes known to change during senescence at 144-hour post-treatment. Two-tailed Student's *t* test.

(I) Timeline of the induction of I-*Ppo*I and assessment of mice.

(J and K) Immunoprecipitation and quantification of a I-*Ppo*I cut site (Tmem56) in skeletal muscle, liver and kidney during and after tamoxifen treatment (0-,1- and 10-month post-treatment). Two-tailed Student's *t* test.

Data are mean (n≥3) ± SD. n.s.: $p > 0.05$; $*p < 0.05$; $**p < 0.01$; $***p < 0.001$.

26

Figure 2. ICE mice phenocopy normal aging

(A) Timeline of phenotypic assessments of mice.

(B) Representative images of Cre and ICE mice.

(C-E) Weight and body mass of Cre and ICE mice. Repeated measures one-way ANOVA (C). One-way ANOVA-Bonferroni (D, left). Two-way ANOVA-Bonferroni (D right and E).

(F) Respiratory Exchange Rate (RER) of 10-month post-treated Cre and ICE mice. Repeated measures one-way ANOVA.

(G) Average activity of Cre and ICE mice for 55 days. Repeated measures one-way ANOVA.

(H) Frailty index scores of Cre, ICE, wild type 3 and 24 month-old mice. Two-tailed Student's *t* test (left) or two-way ANOVA-Bonferroni (right).

(I and J) CT of whole skeleton and micro-CT of trabecular and cortical bones of post-treated Cre and ICE mice. Kyphosis assessment (I), bone/tissue volume (J, left) and trabecular separation (J, right). Two-tailed Student's *t* test.

(K and L) Representative images and average damage scores (1+ normal – 4+ global scarring) of glomeruli of 10-month post-treated ICE mice. OC, outer cortex; JM, juxtamedullary glomeruli. Two-tailed Student's *t* test.

(M and N) Representative images of p57 (podocyte) and Periodic acid-Schiff staining and podocyte density of 10-month post-treated ICE mice. Circles with broken line indicate glomeruli. Scale bar, 50 µm. Two-tailed Student's *t* test.

(O and P) Representative images and fraction of α-SMA-positive cells in parietal epithelial cells (PEC) along Bowman's capsule (arrows) of 10-month post-treated ICE mice showing an epithelial to mesenchymal transition (EMT). Circles with broken line indicate glomeruli. Scale bar, 50 µm. Two-tailed Student's *t* test.

Data are mean ± SEM. n.s.: $p > 0.05$; *$p < 0.05$; **$p < 0.01$; ***$p < 0.001$; ****$p < 0.0001$.

27

Figure 3. ICE mice phenocopy brain aging

(A) Timeline of phenotypic assessments of mice.

(B) Ambulatory activity of 10-month post-treated Cre and ICE mice in light and dark cycles. Two-way ANOVA-Bonferroni.

(C-E) Immediate and contextual freezing in fear conditioning tests in 10-month post-treated Cre and ICE mice. One-way ANOVA-Bonferroni (D, left and E, left) or two-tailed Student's t test (D, right and E, right).

(F and G) Representative images of Barnes maze tests and mean number of pokes at each hole in 10-month post-treated Cre and ICE mice. Two-way ANOVA-Bonferroni.

(H-K) Immunofluorescence of the hippocampal CA3 region immunostained for activation of astrocytes (GFAP) and microglia (Iba1) in 10-month post-treated Cre and ICE mice. Scale bar, 100 μm. Two-tailed Student's t test.

Data are mean ± SEM. n.s.: $p > 0.05$; *$p < 0.05$; **$p < 0.01$; ***$p < 0.001$; **** $p < 0.0001$.

28

Figure 4. ICE mice phenocopy muscle aging

(A) Timeline of phenotypic assessments of mice.

(B) Muscle mass of 10-month post-treated Cre and ICE mice assessed by MRI. Two-tailed Student's t test.

(C) Treadmill endurance in WT, 10-month post-treated Cre and ICE mice. Two-tailed Student's t test.

(D) ATP levels of 10-month post-treated Cre and ICE muscle. Two-tailed Student's t test (let) or two-way ANOVA-Bonferroni (right).

(E and F) Mitochondrial morphology and area of 10-month post-treated Cre and ICE muscle. Scale bar, 500 nm. Two-tailed Student's t test.

(G and H) 10-month post-treated Cre and ICE gastrocnemius immunostained with laminin (red) and CD31(green), markers of the extracellular matrix and capillaries, respectively, and the ratio thereof. Two-tailed Student's t test.

(I) Scatter plot of genes significantly changed ($p<0.01$) in muscle from 10-month post-treated ICE mice and wild type 24 month-old mice.

(J) Heatmaps of the top 200 most significantly altered genes in skeletal muscle of Cre and ICE mice.

(K) Epigenetic age of gastrocnemii of Cre and ICE mice 1-, 10-, and 14-month post-treatment. Linear regression analysis and Spearman correlation.

(L and M) Epigenetic age of muscle and blood of Cre and ICE mice at 10-month post-treatment (Δ age = epigenetic age – chronological age.). Two-tailed Student's t test.

Data are mean ± SEM. n.s.: $p > 0.05$; *$p < 0.05$; **$p < 0.01$; ***$p< 0.001$; **** $p < 0.0001$.

29

Figure 5. ICE cells exhibit smoothening of the epigenetic landscape

907

908 (A) Quantitative mass spectrometry of histone H3 and H4 modifications in 96-hour post-treated

909 ICE cells; unmod, unmodified; me, methylation; ac, acetylation.

910 (B) Genome-wide changes of H3K27ac in 96- hour post-treated ICE cells compared to Cre

911 controls. Heatmap of ICE/Cre.

912 (C) Gene Ontology analysis of H3K27ac-increased, H3K56ac-increased, or H3K27me3-

913 decreased peaks ordered by top 20 processes enriched in H3K27ac-increased regions (padj <

914 0.01). ↑, Cre < ICE peaks, padj < 0.01; ↓, Cre > ICE peaks, padj < 0.01.

915 (D) TreeFam analysis of gene families with overlapping regions with histone modification

916 changes (padj < 0.01) in ICE cells. Two gene families with triple overlap were homeobox (*Hox*)

917 genes.

918 (E) Volcano plot of H3K27ac peaks. All peaks and peaks in *Hox* genes shown white to yellow

919 and blue to purple, respectively.

920 (F) ChIP-seq track of histone modifications and mRNA levels across the 120 kb *Hoxa* locus of

921 post-treated ICE cells.

922 (G) Hi-C contact matrices and HiChIP contact loops in *Hoxa*. Red loops show chromatin

923 contacts between *Hoxa* promoters and other regions. Lower panels show regions with ChIP-seq

924 or RNA-seq peaks. Peak regions were marked in red (Cre<ICE), blue (Cre>ICE) or grey

925 (unchanged). MEF H3K4me1 ChIP-seq peaks were from ENCODE database.

926

927

928

929

930

931

932

933

934

935

936

937

Figure 6. Induction of the ICE system disrupts cellular identity

(A) Gene Ontology analysis of H3K27me3 decreased regions (padj < 0.05). Red represents developmental processes. *neuronal processes.

(B) Mouse tissue types of transcriptional profiles that overlap decreased H3K27me3 regions (padj < 0.05) in epigenetically aged ICE cells. Red represents neuronal tissues. Numbers indicate ranks.

(C) ChIP-seq track of representative neuronal marker genes, *Neurod1* and *Nefh*. Diff peaks = ICE – Cre.

(D and E) Time-course analysis of mRNA levels of *Col1A1* (a fibroblast marker), *Neurod1* and *Nefh* (neuronal markers) during neuronal reprogramming. Two-way ANOVA-Bonferroni.

(F and G) Immunostaining and quantification of neuronal marker Tuj1 after 8 days of reprogramming. DNA stained with DAPI. Scale bar, 100 µm. Two-tailed Student's *t* test.

(H) Comparison of H3K27ac increased regions (p < 0.01) to epigenome roadmap data from different human tissue types.

(I) Gene Ontology comparison of H3K27ac increased regions in 10-month post-treated ICE mice (16 mo.) (p < 0.01) to RNA-seq data from skeletal muscle from old wildtype mice (24 mo.) (padj < 0.05).

Data are mean (n≥3) ± SD. *p < 0.05; **p < 0.01.

Figure 7. Epigenetic reprogramming restores youthful gene expression patterns

(A) AAV vectors used for polycistronic OSK expression.

(B) Experimental scheme for AAV transduction and doxycycline (Dox) treatment. Fibroblasts were isolated from 1-month post-treated Cre (n=3) or ICE (n=3) mice for AAV-DJ-OSK transduction (ICE, n=3).

(C) Scatter plot of mRNA changes in ICE or ICE+OSK fibroblasts. Linear regression.

(D) Schematic of the transgenes in the OSK transgenic mouse.

(E) Experimental scheme for OSK induction in fibroblasts from young (3 mo., n=8) or old (15 mo., n=3) OSK transgenic mice for Dox treatment (15 mo., n=3).

(F) Scatter plot of mRNA changes by aging or OSK. Linear regression.

(G) Schematic diagram of the optic nerve head indicating the location of tissues obtained for axon counts (solid line). V, retinal blood vessels; MTZ, myelination transition zone; Ax, axon bundles.

(H-K) Representative photomicrographs of PPD stained myelinated optic nerve axons. Scale bar, 10 μm. Quantification of healthy axons in 10-month post-treated Cre and ICE mice, represented as axon density (x10^4)/mm^2. Two-tailed Student's t test.

(L) Schematic of intravitreal injection of AAV2-OSK and retina ganglion cell (RGC) sorting. RGCs were sorted from the retinas of young (5 mo., n=5), old (12 mo., n=6) and old mice injected with AAV2-OSK (15 mo., n=4).

(M) Gene Ontology analysis of upregulated genes in RNA-seq data (5 mo. vs 12 mo., padj < 0.01).

(N) Scatter plot of mRNA changes in age-associated genes (grey) and nerve system developmental genes (other colors) by aging or epigenetic reprogramming.

(O) Model for the loss of epigenetic information during aging.

Data are mean ± SEM. *p < 0.05.

32

Figure S1. The ICE system does not induce genomic instability, Related to Figure 1

(A) Breeding scheme to generate ICE mice and negative controls (WT, Cre and I-*Ppo*I).

(B and C) DNA damage response induced by I-*Ppo*I (4-OHT, 0.1, 0.5, 1 μM) vs. other DNA damaging agents, etoposide (ETS, 1, 10, 25 μM) and phleomycin (Phleo, 1, 25, 50 μg/ml). Scale bar, 10 μM. One-way ANOVA-Bonferroni.

(D) Western blot of proteins that are involved in and downstream of the DNA damage response. Blots assessing p53p and γH2AX were reprobed for p53 and H2AX using antibodies raised in different species.

(E) Cell cycle profile in Cre and ICE cells 96-hour post-tamoxifen treatment.

(F) Percentage of senescence-associated β-galactosidase positive (blue) cells during and after tamoxifen treatment compared to replicative senescent cells. p, passage. One-way ANOVA-Bonferroni.

(G) Cell diameter after recovery from I-*Ppo*I induction vs. irradiated (senescent) cells. One-way ANOVA-Bonferroni.

(H-J) Percent non-mutated I-*Ppo*I canonical, non-canonical recognition and random sequences in 96-hour post-treated ICE cells assessed by deep sequencing (>50x).

(K and L) Immunostaining of DNA damage markers γH2AX and 53BP1 in post-treated ICE cells with and without exposure to the DNA damaging agents (ETS, etoposide; CPT, camptothecin; H_2O_2, hydrogen peroxide). Scale bar, 10 μm. Two-tailed Student's *t* test.

(M and N) Lamin B1 mRNA and protein levels in 144-hour post-treated ICE cells. Lamin A/C and actin are loading controls known not to change during senescence.

Data are mean (n≥3) ± SD. n.s.: $p > 0.05$; *$p < 0.05$; **$p < 0.01$; ***$p < 0.001$; **** $p < 0.0001$.

33

Figure S2. No change in 28S rDNA in post-treated ice cells and muscle, Related to Figure 1 and 2

(A) Southern blot of 28S rDNA during 4-OHT treatment and post-treatment.

(B) *In vitro* cutting of I-*Ppo*I targets PCR-amplified from genomic DNA from 96- hour post-treated Cre and ICE cells.

(C) Surveyor nuclease assay of I-*Ppo*I targets in 96- hour post-treated Cre and ICE cells. A PCR fragment with a point mutation (PM) in the I-*Ppo*I site served as a positive control.

(D) Mutation frequency of 28S rDNA in 96- hour post-treated Cre and ICE cells. Two-tailed Student's *t* test.

(E) 28S rRNA level in 96- hour post-treated ICE cells. Two-tailed Student's *t* test.

(F) Bioanalyzer tracks of 28S and 18S rRNA in 96- hour post-treated Cre and ICE cells.

(G) 28S:18S rRNA ratio. Two-tailed Student's *t* test.

(H) Scheme for ligation-mediated PCR to detect residual rDNA breaks.

(I-K) Ligation-mediated PCR after I-*Ppo*I digestion *In vitro* (I), in Cre and ICE cells (J) or in 10-month post-treated Cre and ICE muscle (K).

(L and M) Protein translation in 96- hour post-treated Cre and ICE cells assessed by metabolic ^{35}S-labelling. Two-tailed Student's *t* test.

(N and O) Protein translation in 10-month post-treated Cre and ICE brain (N) and muscle (O) assessed by metabolic ^{35}S-labelling. Two-tailed Student's *t* test.

(P) 28S rDNA copy number in 10-month post-treated Cre and ICE muscle assessed by monochrome multiplex quantitative PCR (MMQPCR). One-way ANOVA-Bonferroni (left) or two-way ANOVA-Bonferroni (right).

(Q) 28S rRNA levels in 10-month post-treated Cre and ICE muscle. One-way ANOVA-Bonferroni (left) or two-way ANOVA-Bonferroni (right).

Data are mean (n≥3) ± SD. n.s.: p > 0.05; **** p < 0.0001.

Figure S3. Validation of the ICE mouse, Related to Figure 2

(A) Removal of the transcriptional STOP cassette in major tissues. One-way ANOVA-Bonferroni.

(B) Western blot of tissues probed with anti-HA to detect I-*Ppo*I expression and γH2AX after a 4-week tamoxifen treatment.

(C and D) Hippocampal sections immunostained for GFP (as a proxy for IRES-linked I-*Ppo*I expression) and γH2AX. Scale bar, 200 μm (100X, C) and 50 μm (400X, D).

(E) Western blot of tissues probed with anti-HA to detect I-*Ppo*I expression at 3-week tamoxifen treatment and 1-month post-treatment time point.

(F) Immunoprecipitation and quantification of a I-*Ppo*I cut site (28S rDNA) in skeletal muscle, liver and kidney during and after tamoxifen treatment (0-,1- and 10-month post-treatment). Two-tailed Student's *t* test. Data are mean (n=3-6) ± SEM. * p < 0.05.

(G-I) Percent non-mutated I-*Ppo*I canonical, non-canonical recognition and random sequences in 1-month post-treated ICE muscle assessed by deep sequencing (>50x).

35

Figure S4. ICE mice phenocopy normal aging, Related to Figure 2 and 3

1092 **Figure S4. ICE mice phenocopy normal aging, Related to Figure 2 and 3**

1093 (A) Food consumption of post-treated Cre and ICE mice. Two-tailed Student's *t* test.

1094 (B) Body weights of female Cre and ICE mice during post-treatment. Repeated measures one-

1095 way ANOVA.

1096 (C) Representative images of Cre and ICE mice from Dual Energy X-ray Absorptiometry (DEXA)

1097 10-month post-treatment.

1098 (D) Body mass of 10-month post-treated Cre and ICE mice. Two-tailed Student's *t* test.

1099 (E) Subcutaneous fat thickness of 10-month post-treated Cre and ICE mice. Two-tailed

1100 Student's *t* test.

1101 (F) Respiratory Exchange Rate (RER) of female Cre and ICE mice. Repeated measures one-

1102 way ANOVA.

1103 (G and H) Blood glucose levels of 10-month post-treated Cre and ICE mice in the fed or fasted

1104 state. Two-tailed Student's *t* test.

1105 (I) IGF-1 levels in 10-month post-treated Cre and ICE mice. Two-way ANOVA-Bonferroni.

1106 (J and K) H&E staining of subcutaneous fat layers and subepidermal thickness of back skin from

1107 old WT, 10-month post-treated Cre and ICE mice. Scale bar, 500 μm. One-way ANOVA-

1108 Bonferroni (left) or two-tailed Student's *t* test (right).

1109 (L) KIT (CD117), KRT55 and DAPI staining of back skin. Scale bar, 50 μm.

1110 (M) Percent of hair follicle bulges without KIT staining. Two-tailed Student's *t* test.

1111 (N-P) Gait analysis of 10-month post-treated Cre and ICE mice. Two-tailed Student's *t* test.

1112 Data are mean ± SEM. n.s.: $p > 0.05$; *$p < 0.05$; **$p < 0.01$; ***$p < 0.001$.

1113

1114

1115

1116

1117

1118

1119

1120

1121

1122

36

Figure S5. Progeroid features of ICE mouse muscle, Related to Figure 4

(A) Blood lactate build-up after exercise in WT, 10-month post-treated Cre and ICE mice. Two-tailed Student's *t* test.

(B) Grip strength measured as maximal "peak force". Two-tailed Student's *t* test.

(C) Mitochondrial DNA copy number. Two-tailed Student's *t* test.

(D-F) Mitochondria number (D and E) and mitochondrial perimeter (D and F) of 10-month post-treated Cre and ICE muscle determined with electron microscopy. Two-tailed Student's *t* test. Scale bar, 500 nm.

(G and H) Cytochrome oxidase (COX) staining of 10-month post-treated Cre and ICE gastrocnemius muscle. Scale bar, 100 μm. Two-tailed Student's *t* test.

(I and J) Quantification of RNA from repetitive DNA elements in gastrocnemius muscle (I) and liver (J) of 10-month post-treated Cre and ICE mice. Two-tailed Student's *t* test.

(K and L) Echocardiogram of 10-month post-treated Cre and ICE mice. LVPWd, Left ventricular posterior wall thickness at end-diastole mm. LVIDd, Left ventricular internal diameter in diastole; LVPWd, Left ventricular posterior wall in diastole; LVEF, Left ventricular ejection fraction. Two-tailed Student's *t* test.

(M) Scatter plot of genes significantly altered (p<0.01) in muscle from 10-month post-treated ICE mice or wild type 24 month-old mice.

(N) Fold change of altered genes (padj<0.05, Cre vs ICE mice) in wild type 24 month-old mice.

(O) Fold change of altered genes (padj<0.05, 12mo. vs 24mo.) in 10-month post-treated ICE mice.

Data are mean ± SEM. n.s.: p > 0.05; *p < 0.05; **p < 0.01; ***p< 0.001, ****p< 0.0001.

37

Figure S6. Altered epigenetic landscapes in ICE cells and muscle, Related to Figure 4-6

(A-D) Muscle and blood training (A and C) and testing sets (B and D) of the clock CpG sites in WT C57BL/6J mice.

(E) Circos plot of genomic locations of I-*Ppo*I cut sites (green), muscle clock GpG sites in CpG islands (red), and all muscle clock sites (blue).

(F) Western blotting for histone modifications in 96-hour post-treated ICE cells. Histone H3, macroH2A and GAPDH serve as loading and internal controls.

(G) Spike-in normalization of ChIP-seq data.

(H) ATAC signal in H3K27ac peaks.

(I) Aggregation plots and heatmaps of H3K27ac signal in H3K27ac changed regions (padj < 0.01).

(J) Aggregation plots of H3K27ac signal in top 40% or bottom 40% quantile.

(K and L) qPCR analysis of *Hoxa* genes in 96-hour post-treated cells cut with either I-*Ppo*I or I-*Sce*I homing endonucleases. Two-tailed Student's *t* test.

(M) Super-enhancers (SEs) in different cell types that overlap with regions with increased H3K27ac signals (Cre>ICE in 10-month post-treated ICE muscle).

(N) Comparison of H3K27ac decreased regions (p < 0.01) in muscle to epigenome roadmap data from different human tissue types.

Data are mean (n=3) ± SD. *p < 0.05; **p < 0.01.

38

Figure S7. Partial epigenetic reprogramming using adeno-associated virus (AAV)-

1186 **mediated gene transfer, Related to Figure 7**

1187 (A and B) Western blot of Oct4 and Klf4 in 293T cells after AAV-DJ transduction.

1188 (C) Experimental scheme for AAV transduction and doxycycline (Dox) treatment to fibroblasts.

1189 (D) Dose-dependent increase in mRNA levels of Oct4, Sox2 and Klf4 in mouse fibroblasts at

1190 day 4. Two-tailed Student's *t* test.

1191 (E) Immunocytochemistry of Oct4 and Klf4 in mouse fibroblasts at day 4. DNA stained with

1192 DAPI. Scale bar, 50 μm.

1193 (F-I) Experimental scheme and mRNA levels of Oct4, Sox2 and Klf4 at day 12 in Cre and ICE

1194 fibroblasts (F and G) or at day 5 in young and old OSK transgenic fibroblasts (H and I). One-way

1195 ANOVA-Bonferroni.

1196 (J) Timeline of phenotype assessments.

1197 (K and L) Representative images and quantification of lens opacity in 10-month post-treated Cre

1198 and ICE mice. Two-tailed Student's *t* test.

1199 Data are mean (n=3) ± SD. *p < 0.05; **p < 0.01; ***p< 0.001; ****p< 0.0001.

1200

1201

1202

1203

1204

1205

1206

1207

1208

1209

1210

1211

1212

1213

1214

1215

1216 **Key resources table**

REGENT or RESOURCE	SOURCE	IDENTIFIER
Antibodies		
Rabbit polyclonal anti-H3	Abcam	Cat# ab1791 RRID: AB_302613
Mouse monoclonal anti-H3	Abcam	Cat# ab10799 RRID: AB_470239
Rabbit polyclonal anti-H3K27ac	Active motif	Cat# 39134 RRID: AB_2722569
Rabbit polyclonal anti-H3K56ac	Millipore	Cat# 07-677-I RRID: AB_390167
Rabbit polyclonal anti-H3K27me3	Millipore	Cat# 07-449 RRID: AB_310624
Rabbit polyclonal anti-H4K20me3	Abcam	Cat# ab9053 RRID: AB_306969
Rabbit polyclonal anti-γH2AX	Abcam	Cat# ab2893 RRID: AB_303388
Rabbit polyclonal anti-γH2AX	Cell Signaling Technology	Cat# 2577 RRID: AB_2118010
Mouse monoclonal anti-γH2AX	Novus	Cat# NBP1-19255 RRID: AB_1642310
Rabbit polyclonal anti-H2AX	Abcam	Cat# ab11175 RRID: AB_297814
Rabbit polyclonal anti-53BP1	Novus	Cat# NB100-304 RRID: AB_10003037
Rabbit polyclonal anti-p53p	Cell Signaling Technology	Cat# 9284 RRID: AB_331464
Mouse monoclonal anti-P53	Cell Signaling Technology	Cat# 2524 RRID: AB_331743
Mouse monoclonal anti-ATMp	Cell Signaling Technology	Cat# 4526 RRID: AB_2062663
Rabbit polyclonal anti-p16	Santa Cruz Biotechnology	Cat# sc-1207 RRID: AB_632106
Rabbit polyclonal anti-PARP1	Cell Signaling Technology	Cat# 9542 RRID: AB_2160739
Rat monoclonal anti-CD31 (RM0032-1D12)	Abcam	Cat# ab56299 RRID: AB_940884
Rabbit polyclonal anti-Laminin	Sigma-Aldrich	Cat# L9393 RRID: AB_477163
Rabbit polyclonal anti-Iba1	Wako	Cat# 01919741 RRID: 01919741
Rabbit polyclonal anti-GFAP	Antibodies.com	Cat# A85419 RRID: AB_2752917
Mouse monoclonal anti-Lamin A/C	BD Bioscience	Cat# 612163 RRID: AB_399534
Rabbit polyclonal anti-Lamin B1	Abcam	Cat# ab16048 RRID: ab16048

40

Rabbit polyclonal anti-macroH2A1	Active motif	Cat# 39593 RRID: AB_2793271
Mouse monoclonal anti-GAPDH	Millipore	Cat# MAB374 RRID:
Mouse monoclonal anti-TuJ1	BioLegend	Cat# 801201 RRID: AB_2313773
Rat monoclonal anti-HA-Peroxidase	Roche	Cat# 12013819001 RRID: AB_390917
Alexa Fluor® 488 Goat Anti-Mouse IgG (H+L)	Thermo Fisher Scientific	Cat# A-11029 RRID: AB_138404
Alexa Fluor® 568 Goat Anti-Rabbit IgG (H+L)	Thermo Fisher Scientific	Cat# A-11036 RRID: AB_10563566
Anti-rabbit IgG	Millipore	Cat# 12-370 RRID: AB_145841
Chemicals, Peptides, and Recombinant Proteins		
Tamoxifen citrate salt	Sigma-Aldrich	Cat# T9262
Etoposide	CALBIOCHEM	Cat# 341205
Camptothecin	CALBIOCHEM	Cat# 208925
Paraquat	SIGMA	Cat# 36541
Hydrogen peroxide	SIGMA	Cat# 216763
Phleomycin	InvivoGen	Cat# ant-ph-1
dCTP [α-32P]	PerkinElmer	Cat# BLU513H500UC
L-[35S]-Methionine	PerkinElmer	Cat# NEG709A500UC
Recombinant I-PpoI	Promega	Cat# R7031
Rodent Chow Diet	LabDiet	Cat# 5053
LightCycler 480 SYBR Green I Master	Roche	Cat# 4707516001
Dynabeads® Protein A for Immunoprecipitation	Life Technologies	Cat# 10001D
Dynabeads® Protein G for Immunoprecipitation	Life Technologies	Cat# 10003D
Dynabeads® M-280 Streptavidin	Life Technologies	Cat# 11205D
UltraPure™ Buffer-Saturated Phenol	Thermo Fisher	Cat# 15513039
Phenylalanine, L-[2,3,4,5,6-3H]	PerkinElmer	Cat# NET1122001MC
Hematoxylin solution modified acc. to Gill II	Millipore	Cat# 1051750500
Eosin Y-solution 0.5% alcoholic	Millipore	Cat# 1024390500
Fluoroshield mounting medium with DAPI	Sigma-Aldrich	Cat# F6057
bFGF	STEM CELL	Cat# 78003.1
ISX9	CAYMAN CHEM	Cat# 16165
Forskolin	CAYMAN CHEM	Cat# 11018
CHIR99021	LC Laboratories	Cat# C-6556
I-BET151	CAYMAN CHEM	Cat# 11181
Fasudil	Selleckchem	Cat# S1573
SB203580	Selleckchem	Cat# S1076
Dynabeads® Protein A	Thermo Fisher	Cat# 10001D
Dynabeads® Protein G	Thermo Fisher	Cat# 10003D
AMPure® XP Beads	BECKMAN COULTER	Cat# A63881
Propidium Iodide	Abcam	Cat# ab14083
Premium Grade Fetal Bovine Serum	Seradigm	Cat# 1500-500
Charcoal stripped FBS	VWR	Cat# 35-072-CV

Tet System Approved FBS	TAKARA	Cat# 631106
N-2 Supplement	Thermo Fisher Scientific	Cat# 17502001
B-27™ Supplement	Thermo Fisher Scientific	Cat# 17504044
GlutaMAX™ Supplement	Thermo Fisher Scientific	Cat# 35050061
Neurobasal™ Medium	Thermo Fisher Scientific	Cat# 21103049
0.1% Gelatin	Millipore	Cat# ES-006-B
Formaldehyde	CALBIOCHEM	Cat# 344198
Paraformaldehyde	Electron Microscopy Sciences	Cat# 15710
Adenosine-5'-triphosphate disodium salt hydrate	VWR	Cat# AAJ61125-09
NEBNext® High-Fidelity 2X PCR Master Mix	New England Biolabs	Cat# M0541S
TRIzol® Reagent	Thermo Fisher Scientific	Cat# 15596-026
VECTASHIELD® PLUS Antifade Mounting Medium	Vector Laboratories	Cat# H-1900-10
cOmplete™ EDTA-free Protease Inhibitor Cocktail	Roche	Cat# 4693132001
Phosphatase Inhibitor Cocktail 2	SIGMA	Cat# P5726
Phosphatase Inhibitor Cocktail 3	SIGMA	Cat# P0044
SuperScript® III Reverse Transcriptase	Thermo Fisher Scientific	Cat# 18080093
Critical Commercial Assays		
E.Z.N.A.® Tissue DNA Kit	Omega Bio-tek	Cat# D3396
E.Z.N.A.® Total RNA Kit I	Omega Bio-tek	Cat# R6834
iScript cDNA synthesis kit	Bio-rad	Cat# 1708891
NEBNext® ChIP-Seq Library Prep Master Mix Set	New England Biolabs	Cat# NEB E6240L
NEBNext® Multiplex Oligos for Illumina	New England Biolabs	Cat# NEB E7335S
RNeasy MinElute Cleanup Kit	QIAGEN	Cat# 74204
NEXTflex™ Rapid RNA Sequencing Kit	Bioo Scientific	Cat# 5138-01
NEXTflex™ RNA-Seq Barcodes – 12	Bioo Scientific	Cat# 512912
Nextera DNA Library Prep Kit	Illumina	Cat# FC-121-1030
Dovetail™ HiChIP MNase Kit	Dovetail Genomics	Cat# 21007
QuantiFluor® dsDNA System	Promega	Cat# E2670
QuantiFluor® RNA System	Promega	Cat# E3310
Library Quantification Kits	Kapa Biosystems	Cat# KK4854
ChIP DNA clean & concentrator	Zymo	Cat# D5201
Surveyor® Mutation Detection Kits	Transgenomic	Cat# 706025
ChIP DNA Clean & Concentrator™	Zymo Research	Cat# D5201
Click-iT™ EdU Alexa Fluor™ 488 Flow Cytometry Assay Kit	Thermo Fisher Scientific	Cat# C-10425
Senescence β-Galactosidase Staining	Cell Signaling Technology	Cat# 9860
Software and Algorithms		
Cellprofiler	Broad Institute	http://cellprofiler.org/
Ensembl blat	European Bioinformatics Institute	http://www.ensembl.org/Multi/Tools/Blast?db=core
GraphPad Prism	GraphPad Software	https://www.graphpad.com
Metacore	GeneGo	https://portal.genego.com/
Galaxy	Penn State University	https://usegalaxy.org/
GREAT	Stanford University	http://great.stanford.edu/public/html/
Enrichr	Mount Sinai	http://amp.pharm.mssm.edu/Enrichr/

ChIP-enrich	University of Michigan	http://chip-enrich.med.umich.edu/chipMain.jsp
Easeq	University of Copenhagen	https://easeq.net/
Primer-BLAST	NIH	https://www.ncbi.nlm.nih.gov/tools/primer-blast/
Experimental Models: Organisms/Strains		
C57BL/6 mouse	NIA (USA)	N/A
C57BL/6 HA-ERT2-I-*Ppo*I mouse	This paper	N/A
C57BL/6 Cre-ERT2 mouse	Ruzankina et al., 2007	N/A
I-*Sce*I mouse	Chiarle et al., 2011	N/A
Experimental Models: Cell Lines		
WT mouse embryonic fibroblasts	This paper	N/A
I-*Ppo*I mouse embryonic fibroblasts	This paper	N/A
Cre mouse embryonic fibroblasts	This paper	N/A
ICE mouse embryonic fibroblasts	This paper	N/A
Cre mouse adult fibroblasts	This paper	N/A
ICE mouse adult fibroblasts	This paper	N/A
I-*Sce*I mouse embryonic fibroblasts	This paper	N/A
3 mo. OSK-tg mouse adult fibroblasts	This paper	N/A
15 mo. OSK-tg mouse adult fibroblasts	This paper	N/A
Deposited Data		
ChIP-seq, ATAC-seq, RNA-seq or Hi-C data	BioProject ID: PRJNA554729	

1217

1218

METHOD DETAILS

1220

Mice and treatments

1222 I-*Ppo*I^{STOP} knock-in mouse ES cells were generated the following way. Briefly, an estrogen

1223 receptor nuclear translocation domain (ER^{T2}) tagged with HA at N-terminus and I-*Ppo*I were

1224 inserted into STOP-eGFP-ROSA26TV plasmid (addgene, plasmid #11739) together followed by

1225 IRES and EGFP sequence. HA-ER^{T2}-I-*Ppo*I^{STOP} cassette was integrated at Rosa26 loci and the

1226 targeted C57BL6 ES cells were injected into C57BL/6 albino (cBRD/cBRD) blastocysts. After

1227 back-crossing I-*Ppo*I $^{STOP/+}$ chimeric mice with C57BL/6 mice, ICE mice were generated by

1228 crossing I-*Ppo*I $^{STOP/+}$ mice to Cre$^{ERT2/+}$ mice harboring a single ER^{T2} fused to Cre recombinase

1229 that is induced whole body (Ruzankina et al., 2007). 4-6 month-old Cre and ICE mice were fed a

1230 modified AIN-93G purified rodent diet with 360 mg/kg Tamoxifen citrate for 3 weeks to carry out

1231 I-*Ppo*I induction. ER^{T2} containing three mutations selectively binds to 4-hydroxytamoxifen (4-

1232 OHT) but not estradiol. Cre-ER^{T2} protein is translocated into nucleus by tamoxifen treatment

1233 followed by removal of the STOP cassette located at upstream of I-*Ppo*I. In the presence of

43

1234 tamoxifen, Cre- ER^{T2} and HA-ER^{T2}-I-*Ppo*I localize to the nucleus and induce DNA double strand

1235 breaks. Wild-type aged mice were obtained from the NIA aged rodent colonies and acclimatized

1236 at least for a month prior to experimentation. Mice were fed LabDiet 5053 diet and all animal

1237 care followed the guidelines of Animal Care and Use Committees (IACUCs) at Harvard Medical

1238 School.

1239

1240 **Cell culture**

1241 Mouse Embryonic Fibroblast (MEF) cells were isolated from E13.5 mouse embryos. After

1242 dissecting out the uterus and yolk sac, fetuses were moved in a new dish containing sterile

1243 PBS. The liver, heart, head were removed and the remaining part was washed in sterile PBS to

1244 remove blood. Fetuses were minced in 0.25% trypsin-EDTA and incubated at 37°C for 30 min.

1245 Cells were washed and maintained with MEF growth medium (DMEM containing 20% FBS, 1%

1246 penicillin/streptomycin, 0.1 mM β-mercaptoethanol). For activation of ER (estrogen receptor)-

1247 fused Cre in MEFs, 0.5 μM 4-Hydroxytamoxifen (4-OHT) was treated for 24 h and medium was

1248 switched to one without 4-OHT to stop I-*Ppo*I-mediated DNA breaks. For activation of GR

1249 (glucocorticoid receptor)-fused I-*Sce*I, 10 μM triamcinolone acetonide (TA) were treated in

1250 DMEM containing charcoal stripped FBS for 2 days.

1251 Mouse adult fibroblast cells were isolated from ears taken from 3, 24 and 30 month-old mice. 2

1252 whole ears were washed with 70% EtOH and sterile PBS and minced in DMEM containing 0.14

1253 Wunsch Units/ml Liberase TM and 1% penicillin/streptomycin. After incubation of minced tissues

1254 at 37°C for 45 min with shaking, cells were washed with medium twice and plated on collagen

1255 coated culture dishes.

1256 Human adult fibroblast cells were obtained from Coriell Institute.

1257 All cells were cultured in DMEM containing 20% FBS (Seradigm), 1% penicillin/streptomycin,

1258 0.1 mM β-mercaptoethanol at 37°C, 3% O_2 and 5% CO_2 unless otherwise specified.

1259

1260 **Western blot analysis**

1261 Cell and tissue samples were lysed in RIPA buffer (50 mM Tris-HCl pH 7.4, 150 mM NaCl,

1262 0.25% deoxycholic acid, 1% NP-40, 1 mM EDTA) containing a proteinase inhibitor cocktail

1263 (Sigma-Aldrich). An equal amount of lysate was incubated with sample buffer (0.05%

1264 Bromophenol blue, 2% sodium dodecyl sulfate, 50 mM Tris-Cl pH 6.8, 5% β-mercaptoethanol)

44

1265 at 95°C for 5 min then separated on an SDS-PAGE gradient gel, transferred to a membrane

1266 using transfer buffer (25 mM Tris-HCl pH 8.3, 190 mM glycine 20% methanol), blocked with

1267 TBSTM (Tris-buffered saline, 0.1% Tween 20, with 5% skim milk), probed with primary and

1268 secondary antibodies and developed using ECL Western Blotting Detection Reagent (Sigma-

1269 Aldrich).

1270

1271 **Southern blotting**

1272 Genomic DNA samples were prepared using EZNATissue DNA Kit (Omega Bio-tek). DNA (3

1273 μg) was run in 0.8% agarose gel, DNA was depurinated in 0.25 N HCl, denatured in 0.4 N

1274 NaOH, and washed with 20X SSC. DNA was transferred to a nylon membrane in 0.4 N NaOH

1275 using a TurboBlotter (Whatman), washed with 2X SSC, crosslinked by UV then incubated in

1276 pre-hybridization solution (6X SSC, 5X Denhardt's solution, 1X SSD,0.0625 M Tris-HCl pH7 .5,

1277 75 μ/ml salmon sperm DNA) at 65ºC for 3 h with rotation. DNA probes were generated using

1278 target-specific PCR with dCTP [α-32P]. Radioactive DNA probes were added to fresh pre-

1279 hybridization solution and incubated with the membrane overnight with rotation. The membrane

1280 was washed with 2X SSC, 2X SSC containing 1% SDS and 0.1X SSC and exposed to X-ray

1281 film at

1282 -80°C.

1283

1284 **Surveyor assay**

1285 I-*Ppo*I target regions were amplified from genomic DNA isolated from either Cre or ICE cells by

1286 PCR using flanking primer sets. Hetero- or homo-duplexes were hybridized in thermocycler and

1287 hybridized DNA (200 ng) was treated with SURVEYOR nuclease S (Transgenomic) at 42ºC for

1288 60 min. Nuclease reactions were stopped and digestion was analyzed by agarose gel

1289 electrophoresis or a Bioanalyzer (Agilent).

1290

1291 **Metabolic labeling of MEFs**

1292 MEFs were washed twice with pulse-labeling medium (Met- Cys-free DMEM containing 10%

1293 dialyzed serum) and incubated in pulse-labeling medium for 1 h to deplete intracellular

1294 Methionine. Pulse-labeling medium with 0.2 mCi/ml methionine [35S] was added to cells and

1295   incubated for 1h. Cells were lysed and ^{35}S-methionine incorporation was determined by TCA

1296   precipitation and scintillation counting.

1297

Quantification of protein synthesis

1299   Protein synthesis was quantified as published (Garlick et al., 1980; Hofmann et al., 2015). L-^{3}H-

1300   phenylalanine (1 mCi/mL) was combined with unlabeled phenylalanine (135 mM) to create 100

1301   mCi/ml. After adjusting the solution to pH 7.1 with NaOH, the labeling solution was injected via

1302   the lateral tail vein at 1 ml/100 g bodyweight under anesthesia with ketamine (75 mg/kg) and

1303   xylazine (10 mg/kg).

1304

Quantification of DSBs

1306   DNA double strand breaks (DSB) generated by I-$PpoI$ were detected as described previously

1307   (Chailleux et al., 2014). Briefly, tissue was homogenized in phenol and genomic DNA was

1308   purified with chloroform, ethanol and RNase. Genomic DNA carrying I-PpoI specific DSBs was

1309   subjected to ligation-mediated purification using biotin-conjugated adaptor nucleotides with 5`-

1310   AATT-3` overhangs that bind to the DSB site generated by I-PpoI. Adaptor sequences were as

1311   follows: dRbiot-BglII-IPpoI F 5`-CCCTATAGTGAGTCGTATTAGATCTGCGTTAA-3`, dRbiot-

1312   BglII-IPpoI R 5`-CGCAGATCTTAATACGACTCACTATAGGG-3`. The biotinylated fragment was

1313   digested using EcoRI for 3 h at 37°C followed by purification with streptavidin magnetic beads

1314   (Dynabeads M-280 Streptavidin, Invitrogen) in binding buffer (20 mM Tris-HCl pH 8.0, 0.1%

1315   SDS, 1% Triton X-100, 2mM EDTA, 150 mM NaCl). After 4 h at 4°C, beads were washed five

1316   times with washing buffer (50 mM Tris-HCl pH 8.0, 0.1% SDS, 150 mM NaCl) and once with TE

1317   buffer. Cut DNA was eluted by digesting the adaptor with BglII at 37°C overnight. DNA was

1318   purified using glycogen, sodium acetate and ethanol. DNA primers were: 5+11 F 5`-

1319   ACTTAGAACTGGCGCTGAC -3`, 5+11 R 5`-CTGGCCTGGAACTCAGAAAT-3`, 28S F

1320   CCCACTGTCCCTACCTACTATC, 28S R AGCTCAACAGGGTCTTCTTTC.

1321

Indirect Calorimetry

1323   Food consumption, ambulatory activity, oxygen consumption (VO$_2$), carbon dioxide production

1324   (VCO$_2$) and respiration exchange ratio (RER) were measured using Columbus Instruments

1325　CLAMS. Mice were housed in metabolic cages for 3 days prior to collecting data and body

1326　composition was determined by EchoMRI 3-in-1.

1327

MMQPCR

1329　Monochrome multiplex quantitative PCR was performed as described previously (Cawthon,

1330　2009). Briefly, a PCR reaction containing 20 ng of genomic DNA was prepared with SYBR

1331　Green system (Applied Biosystems). The PCR program was set up as Step 1: 95°C; 15 min,

1332　Step 2; 2 cycles of 94°C for 15 sec and 49°C for 15 sec, Step 3: 32 cycles of 94°C for 15 sec,

1333　62°C for 15 sec, 74°C for 15 sec with signal acquisition for telomere or 28S amplification, 84°C

1334　for 10 sec, 88°C for 15 sec with signal acquisition for Hbbt1 amplification. Primers are listed in

1335　Table 1.

1336

Frailty index assessment

1338　The Frailty Index (FI) was scored as described previously (Whitehead et al., 2013). Briefly 31

1339　health-related deficits were assessed for each mouse. A mouse was weighed and body surface

1340　temperature was measured three times with an infrared thermometer (La Crosse Technology).

1341　Body weight and temperature were scored based on their deviation from mean weight and

1342　temperature of young mice (Whitehead et al 2014). Twenty-nine other items across the

1343　integument, physical/musculoskeletal, oscular/nasal, digestive/urogenital and respiratory

1344　systems were scored as 0, 0.5 and 1 based on the severity of the deficit. Total score across the

1345　items was divided by the number of items measured to give a frailty index score between 0 and

1346　1.

1347

Lens opacity scoring

1349　Lens opacity scoring was previously described (Wolf et al., 2008). Mice were held without

1350　anesthesia and assessed in a dark room using a SL-14 Kowa hand-held slit lamp (Kowa, Tokyo,

1351　Japan).

1352

PET-CT

1354　Mice were anesthetized with 2% isoflurane gas in oxygen and injected with ~200 µCi F-18

1355　labeled flourodeoxyglucose (FDG) via tail vein injection. After 45 minutes, mice were imaged on

47

a Siemens Inveon small animal imaging scanner for positron emission tomography (PET) and computed tomography (CT) imaging under isoflurane. CT imaging was performed over 360 projections with a 80 kVp 500 μA x-ray tube and reconstructed using a modified feldkamp cone beam reconstruction algorithm (COBRA Exxim Inc., Pleasanton, CA) with 425 ms exposure time/projection during which Isovue-360 (Bracco Diagnostic Inc, Monroe Township, NJ) was pumped into the mouse via tail vein at a rate of 20 μl per minute. PET scans were reconstructed with ordered subset expectation maximization with maximum a posterior reconstruction algorithm with 2 OSEM iterations and 18 MAP iterations.

Magnetic Resonance Imaging

Mice were anesthetized with 2% isoflurane gas in oxygen and placed in a 4.7 Tesla Bruker Pharamscan magnetic resonance imager. Rare T1 (TE: 13.4 ms, TR: 900 ms, Rare factor: 4, Matrix: 256 x 256 x 24, Voxel size: 0.215 x 0.156 x 1 mm) and a Rare T2 (TE: 18.26 ms, TR: 2000 ms, Rare factor: 8, Matrix: 256 x 256 x 24, Voxel size: 0.215 x 0.156 x 1 mm) scans of the lower thoracic cavity, abdomen and lower extremities were performed.

Micro CT scanning

Femurs were isolated and placed in 70% ethanol. Micro-CT was performed by using SCANCO Medical μ-CT35 at the core facility at the Harvard School of Dental Medicine (Idelevich et al., 2018).

Quantification of optic nerve axons

To quantify axons, optic nerves were dissected and fixed in Karnovsky's reagent (50% in phosphate buffer) overnight. Semi-thin cross-sections of the nerve were taken at 1.0 mm posterior to the globe and stained with 1% p-phenylenediamine (PPD) for evaluation by light microscopy. Six to eight non-overlapping photomicrographs were taken at 60x magnification covering the entire area of the optic nerve cross-section. Using ImageJ software, a 100 x 100 μM square was placed on each 60x image and all axons within the square (0.01 mm^2) were counted using the threshold and analyze particles function in image J. The average axon counts in 6-8 images was used to calculate the axon density/mm^2 of optic nerve. Scorers were blinded to experimental groups.

48

1387

Immunohistochemistry for mouse skin

1388

1389 Dorsal skin samples were fixed with 4% paraformaldehyde/PBS and kept on ice for 2 h. The

1390 fixed skin samples were embedded in OCT (Sakura Finetek) and snap frozen in liquid nitrogen

1391 for histology. After washing in PBS, nonspecific staining was blocked with PBS containing 3%

1392 skim milk and 0.1% Triton-X for 30 min. Sections were incubated with primary antibodies at 4°C

1393 overnight: rat anti-mouse CD117 (BD Pharmingen) and rabbit anti-human KRT5 (COVANCE).

1394 Secondary antibodies were conjugated with Alexa Fluor 488 or 594 (Invitrogen). Nuclei were

1395 counterstained with 4',6-diamidino-2-phenylindole (DAPI) and images were obtained using

1396 FV1000 confocal microscope (Olympus). >100 hair follicles per mouse (n=8) were analyzed for

1397 the presence of KIT+ melanocytes in the bulge.

1398

Quantification of subepidermal thickness

1399

1400 Site-matched skin tissue was fixed in formalin, embedded in paraffin, and 5 μm sections were

1401 cut and stained with hematoxylin and eosin. Representative regions of the subcutaneous layer

1402 were measured from the limits of the dermis to the panniculus carnosus ('subepidermis') with

1403 the assistance of an ocular micrometer. Care was taken to ensure that tissue was embedded

1404 perpendicularly and the subdermal thickness determination was not artificially enhanced due to

1405 tangential sectioning. Because the subepidermal layer reached maximum thickness in control

1406 Cre mice at 17-18 months, this timepoint was selected for comparisons with the ICE mice. A

1407 minimum of 10 randomly selected thickness determinations were generated for each tissue

1408 section.

1409

Brain immunohistochemistry

1410

1411 For GFAP and Iba1 staining, the tissues were incubated overnight in paraformaldehyde (4%

1412 v/v). Fixed brains were embedded in paraffin and 6 μm sections were generated using a manual

1413 rotary microtome (Leica). After deparaffinization and re-hydration of tissue slides, an antigen

1414 revealing step was performed by using antigen unmasking solution (Vector). Sections were

1415 blocked in PBS with 5% BSA and 0.3% Triton-X at 4°C for 1 hr and incubated with primary

1416 antibodies in PBS with 2% BSA and 0.1% Triton-X at 4°C overnight with Rabbit anti-GFAP

1417 antibody (Abcam, ab7260), Rabbit anti-Iba1 antibody (Funakoshi, GTX100042). Secondary

49

1418 antibodies conjugated with Alexa Fluor 488 or 594 (Invitrogen) were used followed by DPAI

1419 staining. To localize I-*Ppo*I expression and DNA damage, mice were perfused transcardially and

1420 brains were post-fixed overnight with 4% paraformaldehyde/PBS, then cleared by 30% sucrose

1421 solution. Brains were embedded in OCT (Sakura Finetek) and 40 µm sections were collected

1422 using a cryostat (Leica). Sections were blocked in horse serum/TBS-Triton-X for 30 min at RT,

1423 and then incubated with primary antibodies overnight at 4°C with goat anti-GFP (Abcam) and

1424 rabbit anti-γ-H2AX (Cell Signaling). Secondary antibodies were conjugated with Alexa Flour 488

1425 and 647 (Jackson ImmunoResearch) and co-stained with DAPI.

1426

1427 **ATP and mtDNA measurement**

1428 Snap frozen tissue was briefly washed with PBS and 3 ml Tris-HCl TE saturated phenol per 100

1429 mg was added to the tissue followed by homogenizing with a tissue homogenizer (Omni TH,

1430 Omni). After centrifugation, cell lysates were added to an equal amount of TE saturated phenol,

1431 chloroform and water were added to the same tube. After centrifugation, the supernatant was

1432 used for ATP and mtDNA measurement. ATP was measured using an ATP kit (ThermoFisher

1433 Scientific) and normalized to tissue weight. Genomic DNA and mtDNA were purified with 2.5-

1434 fold ethanol and glycogen. Primers for 18S ribosomal and CytB were used to calculate the ratio

1435 of mtDNA to genomic DNA. Primers were: mouse 18S, 5`-TGTGTTAGGGGACTGGTGGACA-3`

1436 (forward) and 5`-CATCACCCACTTACCCCCAAAA-3` (reverse), mouse Cytb, 5`-

1437 CCCTAGCAATCGTTCACCTC-3` and 5`- TGGGTCTCCTAGTATGTCTGG -3` (reverse).

1438

1439 **Contextual fear conditioning test**

1440 Contextual fear conditioning was assessed using a TSE system. On day 1, mice were placed

1441 into an experimental box (52 cm x 52 cm x 65 cm) and allowed to explore freely for 180 s

1442 followed by 0.5 mA electric shock for 1 s. One more 0.5 mA shock for 1 s was given after 30 s

1443 and immediate freezing was measured every 10 s by a visual count, after which mice were

1444 returned to their home cage. Contextual freezing without a tone was assessed for 180s, 24

1445 hours after the shock, counting freezing every 10 sec.

1446

1447 **Barnes maze test**

50

1448 The maze consisted of a circular and white platform (90 cm in diameter) with 20 x 5 cm diameter

1449 holes arranged around the edge of the platform, elevated 82 cm above the floor. For visual

1450 cues, the platform was surrounded by four pictures with different colors and shapes. A mouse

1451 was placed in the center of maze and then, the mouse was guided to a small chamber termed a

1452 target hole at adaptation period. After 2 min in the target hole, the mouse was returned to the

1453 cage. During the spatial acquisition period, the mouse was allowed to explore the target hole for

1454 3 min. If the mouse entered the target hole or it passed 3 min, the mouse was left for 1 min in

1455 the hole. The trial was repeated 3 times/day for 5 d. A probe trial was performed to test long-

1456 term memory 7 days later by covering the target hole with a lid. The mouse was allowed to

1457 explore the position of target hole for 90 s and the number of pokes in each hole was measured

1458 using TopScanLite version 2.

1459

1460 **Grip strength test, treadmill test and lactate measurement**

1461 To measure muscular strength, a mouse was held by the tail and allowed to grip a mesh grip

1462 with the front paws (BIO-G53, BIOSEB) then pulled backward until grip was released. After a 10

1463 min break, the experiment was repeated. Maximum exercise endurance was assessed with a

1464 treadmill system (TSE). Mice were trained for 3 d prior to recording the performance to

1465 familiarize the mice to the equipment. An electrical stimulation grid was adjusted as 1 mA and

1466 slope was set at 15 degrees. The first day of the training, mice walked on the treadmill at 10

1467 m/min speed for 10 min, with a 10 min break, then walked at 10 m/min speed for 10 min. On the

1468 second and third day, the initial two steps were the same as first day, then walking was started

1469 at 10 m/min and the speed was increased by 1 m/min every minute to a maximum speed of 20

1470 m/min. On day 4, maximum exercise endurance was measured. Six mice were placed on the

1471 treadmill and the belt speed was started at 5 m/min for 5 min to allow the mice warm up. The

1472 speed was increased by 1 m/min up to 20 m/min. After running for 5 min, the speed was

1473 increased from 20 m/min to 21 m/min for 10 min. Mice were then forced to run at 22 m/min until

1474 they remained on the electrical stimulation grid for 10 seconds. Details are available upon

1475 request. The tail blood at pre-exercising and post-exercising was taken and serum lactate level

1476 were measured with a lactate meter (Nova Biomedical).

1477

1478 **Ambulatory activity**

51

1479 Animals were maintained in specific-pathogen-free (SPF) facility and single-housed in

1480 instrumented individually ventilated cages (IVC) (Digital Smart House, Vium, San Mateo, CA,

1481 and Innovive, San Diego, CA) containing corncob bedding with access to Innowheel and

1482 Innodome (Innovive, San Diego, CA), Bed-r'Nest (Andersons Lab Bedding, Maumee, OH), and

1483 foraging mix (Veggie Relish, LabDiet). Animals had unrestricted access to food (Pico Rodent

1484 Diet 5053, Lab Diet, St. Louis, MO) and acidified, sterile water (Innovive, San Diego, CA).

1485 Vium Digital Smart Houses slotted in Vium's proprietary rack system were outfitted with sensors

1486 and a high-definition (HD) camera that enables continuous, 24/7 monitoring of animals and

1487 streams data to a secure cloud-based infrastructure. As described elsewhere (Lim et al., 2019;

1488 Lim et al., 2017), video is processed using computer vision algorithms to produce a digital

1489 history of motion (mm/sec). Motion (mm/s) was averaged across 1 hr bins to produce 1 hr

1490 averages. All 1 hr averages from 6am to 7am across 55 days were averaged and repeated for

1491 each hour of the day.

1492

1493 **Treadmill Gait Analysis**

1494 Gait patterns were measured using forced walking on a treadmill (Columbus Instruments;

1495 Columbus, OH). A high-speed digital video camera recorded images of the ventral side of the

1496 mouse through a transparent treadmill belt reflected off a mirror. Mice for approximately 24 sec

1497 at speeds of 13, 19, and 25 cm/s. TreadScan® software (CleverSys, Inc, Reston, VA) identified

1498 each individual paw of the mouse in each frame as it walked on the treadmill and measures of

1499 stance and swing duration, among other measures, were assessed.

1500

1501 **COX and capillary density staining**

1502 Freshly isolated quadriceps and gastrocnemius muscles were mounted in OCT (Tissue-Tek),

1503 placed in an isopentane bath, and slowly cooled in liquid nitrogen. Transverse sections (20 mm)

1504 were sectioned on a cryostat (Leica). Sections were fixed in pre-cooled acetone (-20°C) for 10

1505 min, washed with PBS, then blocked with BlockAid (Invitrogen) for 1 h at RT, and then

1506 incubated with CD31 (ab56299, Abcam), Laminin (L9393, Sigma) antibodies diluted in blocking

1507 buffer overnight at 4°C. Slides were washed with PBST, then incubated with anti-rat Alexa Fluor

1508 488-conjugated (Life Technologies) and anti-rabbit Alexa Fluor 594-conjugated (Life

1509 Technologies) diluted to 1:500 in blocking buffer for 2 h at RT. Slides were washed again with

52

1510 PBST and mounted with Fluoroshield with DAPI mounting medium (Sigma). Images were

1511 acquired using a confocal fluorescence microscope (Nikon A1). COX staining was performed

1512 according to a protocol (Ross, 2011). Briefly, 20 µm cryostat sections was dried at room

1513 temperature for 1 hr and media containing 1X DAB, 100 µM cytochrome c, 2 µg/ml bovine

1514 catalase was added to sections and slides were incubated at 37°C for 40 min. Quantification of

1515 capillary number and density were performed using ImageJ.

1516

1517 **Electron microscopy**

1518 Mice at 15 months of age were anesthetized with isoflurane and sacrificed by cervical

1519 dislocation or decapitation, in accordance with available ethical permits. Muscle was collected

1520 and fixed in electron microscopy fixative (consisting of 3% glutaraldehyde, 2.5%

1521 paraformaldehyde, 2 mM calcium chloride, 2% sucrose in 0.1 M cacodylate buffer) and tissue

1522 was processed as previously reported (Le Couteur et al., 2001). Two blocks from different parts

1523 of the muscle were used and from each section 10 images were taken at 5000X on a Jeol 1210

1524 transmission microscope and photographed using a Gatan US 4000MP digital camera.

1525 Mitochondrial network, size and number were quantified blindly using FUJI ImageJ.

1526

1527 **Podocyte density p57 and PAS representative images**

1528 Podocyte density was quantitated following staining for p57 on formalin fixed, paraffin-

1529 embedded, 4 µm kidney sections as previously described (Ohse et al., 2010; Schneider et al.,

1530 2017; Zhang et al., 2013). Briefly, Histoclear (National Diagnostics, Atlanta, GA) was used to

1531 deparaffinize kidney sections, followed by rehydration using graded 100%, 95%, and 70%

1532 ethanol baths. Next, antigen retrieval was performed using 10 mM EDTA pH 6.0. Endogenous

1533 peroxidase activity was blocked with 3% v/v H_2O_2. Non-specific antibody binding was blocked

1534 using a 5% non-fat milk in PBS. Rabbit polyclonal p57 antibody (Santa Cruz) was diluted 1:800

1535 in 1% BSA in PBS, applied to the sections, and incubated overnight at 4°C. Rabbit-on-rodent

1536 HRP polymer (Biocare Medical, Concord, CA) was applied and incubated at room temperature

1537 for 45 min. Diaminobenzidine (DAB) (Sigma-Aldrich, St. Louis, MO) with 0.05% NiCl (Sigma-

1538 Aldrich) was used to detect staining. Slides used for podocyte density were not counterstained

1539 in order to improve quantitation sensitivity. For representative images, counterstaining was

1540 performed with periodic acid–Schiff. Sections were placed in 0.5% periodic acid (Sigma-Aldrich),

53

1541   washed in ddH2O, incubated for 10 min with Schiff's Reagent (Sigma-Aldrich), washed in 0.5%

1542   sodium metabisulfate (Sigma-Aldrich) and incubated with hematoxylin (Sigma-Aldrich). Tissue

1543   was dehydrated in 95% and 100% ethanol baths, followed by Histoclear and Histomount

1544   (National Diagnostics). Podocyte density was quantitated according to the correction factor

1545   method from single histological sections, as previous reported (Venkatareddy et al., 2014). An

1546   average of 119 (±14.1) glomeruli for ICE mice and 139 (±16.1) glomeruli for Cre mice were

1547   quantified.

1548

1549   **Glomerular Injury**

1550   Organized matrix accumulation was detected on paraffin-embedded tissue by Jones' basement

1551   membrane stain (Silver Stain) performed by the University of Washington Pathology Research

1552   Services Laboratory following standard protocols (Luna, 1968). Silver stained slides were

1553   quantitated according to the criteria presented in figure 6G. An average of 156 (±10.8) glomeruli

1554   for ICE mice and 187 (±6.36) glomeruli for Cre mice were quantified.

1555

1556   **Parietal epithelial cell to mesenchymal transition**

1557   Parietal epithelial cells (PECs) were stained for alpha-smooth muscle actin (α-SMA) in order to

1558   determine epithelial-mesenchymal transition (EMT) as described above. Non-specific antibody

1559   binding was blocked using Background buster (Accurate Chemical & Scientific Corporation,

1560   Westbury, NY). Rabbit polyclonal α-SMA antibody (Abcam) was diluted 1:400 in 1% BSA in

1561   PBS, applied to the sections, and incubated overnight at 4°C. Detection was performed as

1562   described above. Quantification was performed by counting the number of glomeruli with α-SMA

1563   staining in PECs as previously described (Schneider et al., 2017). An average of 110 (±6.22)

1564   glomeruli for ICE mice and 122 (±19.3) glomeruli for Cre mice were quantified.

1565

1566   **5-Ethynyl-2'-deoxyuridine (EdU) staining**

1567   % EdU-positive cells was measured using the Click-iT® EdU Flow Cytometry Assay Kits

1568   (Invitrogen). Briefly,10 μM EdU was added to the culture medium and incubated for 1h. Cells

1569   were trypsinized, washed, fixed and permeabilized for Click-iT reaction. EdU+ cells were

1570   analyzed using the BD LSR II flow cytometer.

1571

54

Microscopy and imaging for kidney

Imaging and quantification were performed on a Leica DMI400B microscope and an EVOS FL Cell Imaging System. ImageJ 1.51 (NIH) was used to measure podocyte density.

Immunocytochemistry

Cells were washed with sterile PBS and fixed with 4% paraformaldehyde. Fixed cells were permeabilized with 0.5% Triton X-100 in PBS, then blocked with 2% PBA (PBS containing 2% bovine serum albumin) overnight. Primary antibodies were incubated in 2% PBA at RT for 1hr and cells were washed with PBS 3 times. The secondary antibodies (Alexa Fluor 488 Goat Anti-Mouse IgG or Alexa Fluor 568 Goat Anti-Rabbit IgG) were incubated in 2% PBA at RT for 30 min. After PBS washes, nuclei were stained with antifade mounting medium containing DAPI (Vector Laboratories). Immunofluorescence was examined using Olympus Fluoview FV1000 confocal microscope.

Senescence-associated β-galactosidase assay

Senescence-associated β-galactosidase assay were performed using Senescence β-galactosidase staining kit (Cell Signaling Technology). When cells were not senescent at 4d post-treatment, the standard medium was switched to low serum (0.1% FBS) medium to preserve senescent cells that appeared later. Cells were fixed in 4% paraformaldehyde at RT for 10 min. Cells were washed with PBS and stained in β-galactosidase staining solution containing X-gal (pH 6) at 37°C for overnight in dry incubator. Stained cells were monitored under bright field microscopy.

Small molecule-driven neuronal reprogramming

Neuronal reprogramming was performed as described in (Li et al., 2015). MEFs were transferred to matrigel-coated plates. When MEFs were confluent, MEF growth medium was switched to Neurobasal Medum containing 1% N2 and 2% B27 supplements, 1% GlutaMAX (Life technologies), 1% penicillin/streptomycin, 100 ng/ml bFGF (STEM CELL), 20 μM ISX9, 100 μM Forskolin, 0.5 μM I-BET151 (CAYMAN CHEM), 20 μM CHIR99021 (LC Laboratories), 2 μM Fasudil and 1 μM SB203580 (Selleckchem). After 2 days, cells were maintained without Fasudil

55

1602 and SB203580. qPCR to detect neuronal gene activation was performed at day 2 after switching

1603 to Neurobasal medium, and Tuj1 immunocytochemistry was performed at day 13.

1604

1605 **Quantitative real-time PCR for transcription of repetitive elements**

1606 Total RNA was isolated from 30-50 mg of tissue using Trizol reagent (ThermoFisher) according

1607 to the manufacturer's instructions. Prior to the synthesis of cDNA, total RNA was digested with

1608 27.2 Kunitz units of RNase-free DNase (Qiagen) for 45 min at room temperature and further

1609 cleaned up on RNeasy columns (Qiagen) (De Cecco et al., 2013). The effectiveness of the

1610 digestion was assessed using controls that omitted reverse transcriptase (RT). Digestion with

1611 DNase was repeated until the control lacking RT was negative for γ-satellite sequences. RNA

1612 integrity was determined using an Agilent Bioanalyzer 2100 and an RNA-nano chip. Total RNA

1613 (1 μg) of was transcribed into cDNA in 50 μl reactions using the TaqMan Gold RT-PCR kit

1614 (Applied Biosystems) and random hexamers, according to the manufacturer's protocol. This

1615 reaction (1.0 μl) was used in subsequent qPCR reactions, performed using the SYBR Green

1616 system (Applied Biosystems) on the ViiA 7 Real Time System (Applied Biosystems), according

1617 to the manufacturer's specifications. Primers were used at a final concentration of 300 nM.

1618 Tissue from 6 individual animals was analyzed in triplicate. Statistical analysis was determined

1619 using Student's t-test and SigmaPlot 12.5 (Systat Software).

1620

1621 **Design of PCR primers for repetitive elements**

1622 All primers used in this study are listed in Table S1. For expression analysis of LINE-1, MusD

1623 and pericentromeric γ-satellite sequences (MSAT) we used primers described by Changolkar et

1624 al. (Changolkar et al., 2008). Primers for the SINE elements B1 and B2 were designed using the

1625 consensus sequence from Repbase (Genetic Information Research Institute,

1626 www.girinst.org/repbase/index.html) and Primer-Blast software

1627 (www.ncbi.nlm.nih.gov/tools/primer-blast/). Primers against GAPDH and β-actin, used as

1628 normalization controls, were designed with Primer-Blast using NCBI reference sequences

1629 NC_000072.6 and NM_007393.3, respectively. Primer sequences were analyzed using the

1630 UCSC genome browser *in silico* PCR tool (genome.ucsc.edu/cgi-bin/hgPcr) to determine the

1631 number of genomic elements that contribute to the amplification products (De Cecco et al.,

56

1632 2013). All primers were tested with serial dilutions of cDNA to ensure they amplified their target
1633 sequences quantitatively.

1634

1635 **Production and transduction of adeno-associated viruses**
1636 Adeno-associated viruses for OSK expression were produced by the Boston Children's Hospital
1637 Viral Core. Fibroblasts were isolated from 3-month old Cre or ICE mice and maintained in
1638 DMEM with 10% Tet System Approved FBS (Takara) and 1% Pen/Strep. 24h before AAV
1639 transduction, cells were plated in DMEM with 1% Tet System Approved FBS. AAV-DJ-OSK or
1640 rtTA at 10^4 genome copies per cell was transduced and 2 μg/ml doxycycline was treated from
1641 day 6 to day 12. Intravitreal injection of AAV2 was described in detail previously (Lu et al.,
1642 2020).

1643

1644 **RGC sorting and RNA-seq**
1645 Thy1.2+ and Calcein Blue+ RGS were sorted using a BD FACS Aria Cell Sorter with an 130-μm
1646 nozzle and sent to Genewiz for ultra-low input RNA sequencing as previously published (Lu et
1647 al., 2020).

1648

1649 **ChIP-sequencing**
1650 MEF ChIP was done following the protocol described in (Yang et al., 2011) with minor
1651 modifications. 1/4 number of *Drosophila* S2R+ cells relative to mouse cells were added as a
1652 spiked-in control and combined cells were treated as a single sample during the rest of the
1653 procedures. Cells were cross-linked with 1% formaldehyde at RT for 10 min and glycine was
1654 added to final concentration 0.125 M for 5 min to quench crosslinking. Fixed cells were washed
1655 with PBS and nuclei were isolated using Lysis buffer A (10 mM Tris-HCl pH 7.5, 10 mM KCl, 5
1656 mM MgCl2, 0.5% NP40, protease inhibitor cocktail). Nuclei were resuspended in SDS lysis
1657 buffer (50 mM Tris-HCl pH 7.9, 10 mM EDTA, 0.5% SDS, protease inhibitor cocktail). Chromatin
1658 was sheared using Covaris E210 Ultrasonicator (duty cycle:5%, intensity:4, cycle/burst:200,
1659 time:15-20 min) to generate fragmented chromatin ranging between 200 and 1,000 bp. After
1660 centrifugation, sonicated chromatin solution was 5 fold-diluted with ChIP dilution buffer (12.5
1661 mM Tris-HCl pH 7.9, 187.5 mM NaCl, 1.25% Triton X-100, protease inhibitor cocktail).
1662 Antibodies and magnetic beads were added to diluted chromatin solutions and

57

1663 immunoprecipitation were performed at 4°C overnight with rotation. Immunocomplexes were

1664 washed with Low salt wash Buffer (0.1% SDS, 1% Triton X-100, 2 mM EDTA, 20 mM Tris-HCl

1665 pH 8.1, 150 mM NaCl), High salt wash buffer (0.1% SDS, 1% Triton X-100, 2 mM EDTA, 20 mM

1666 Tris-HCl pH 8.1, 500 mM NaCl), LiCl wash buffer (0.25 M LiCl, 1% NP40, 1% deoxycholate, 1

1667 mM EDTA, 10 mM Tris-HCl pH 8.1), and TE (10 mM Tris-HCl pH 8.0, 1 mM EDTA).

1668 Immunocomplexes were eluted in elution buffer (1% SDS, 0.1 M NaHCO3) at RT for 30min with

1669 rotation, and RNaseA (final concentration of 0.5 mg/ml at 37°C for 30 min) and proteinase K

1670 (final concentration of 0.5 mg/ml at 55°C for 1 h) were treated. Samples were de-crosslinked at

1671 65°C overnight, and ChIP DNA was purified using a ChIP DNA clean and concentrator kit

1672 (Zymo).

1673 Muscle ChIP was performed as described previously (Gao et al., 2010). Tissue was chopped

1674 into small pieces on the ice and fix solution (50 mM HEPES pH 7.5, 1 mM EDTA pH 8.0, 0.5

1675 mM EGTA, 100 mM NaCl) was added to cross-link the tissue sample. After incubation for 15

1676 min at room temperature, glycine was added as 0.125 M final concentration to stop the reaction.

1677 The sample was washed using cold PBS three times followed by homogenizing it in cell lysis

1678 buffer (10 mM Tris-HCl pH 8.0, 10 mM NaCl, 0.2% NP40). Cell lysate was centrifuged at 12,000

1679 rpm for 5 min and suspended in nuclear lysis buffer (1% SDS, 10 mM EDTA pH 8.0, 50 mM

1680 Tris-HCl pH 8.0). Sonication was performed using Covaris E220 Ultrasonicator (duty cycle:5%,

1681 intensity:4, cycle/burst:200, time:120 sec). The resulting chromatin was diluted by 10 fold using

1682 dilution buffer (1% Triton X-100, 150 mM NaCl, 2 mM EDTA, 20 mM Tris-HCl pH 8.0). To

1683 reduce non-specific binging to beads, the diluted chromatin was mixed with Dynabeads protein

1684 A/G for 1 h at 4 °C and the beads were removed prior to incubating chromatin with 2 ug of the

1685 appropriate antibodies with Dynabeads protein A/G. After 4 h incubation at 4 °C, beads were

1686 washed three times with wash buffer and once with final wash buffer, LiCl Buffer and TE buffer

1687 each. Wash buffer contains 1% Triton X-100, 150 mM NaCl, 2 mM EDTA, 20 mM Tris-HCl pH

1688 8.0, 0.1% SDS and final wash buffer contains 500 mM NaCl instead of 150 mM NaCl. The

1689 composition of LiCl buffer is 0.25 M LiCl, 1% NP40, 1% deoxycholic acid, 1 mM EDTA, 10 mM

1690 Tris-HCl. ChIP DNA was eluted by incubating at 65°C overnight in elution buffer containing

1691 0.25% SDS, 1 mM EDTA, 10 mM Tris-HCl pH7.5. After treatment of proteinase K and RNase A,

1692 DNA was purified using ethanol precipitation and MinElute kit (QIAGEN).

1693 Purified DNA (1-5 ng) was used for ChIP-seq library construction with NEBNext ChIP-Seq
1694 Library Prep Master Mix Set. ChIP DNA was end-repaired and added with dA tail using Klenow
1695 fragment. Sequencing adaptors were ligated to the dA-tailed libraries, and the libraries raging
1696 around 270 bp were selected using AMPure XP beads (Beckman Coulter). Size-selected
1697 libraries were enriched by PCR with index primers. The quantity and quality of libraries were
1698 respectively monitored by library quantification kit (Kapa Biosystems) and Bioanalyzer (Agilent)
1699 for 75bp, paired-end Illumina NextSeq.

1700

1701 **Hi-C**
1702 Cells were fixed in PBS containing 1% formaldehyde at RT for 15 min, then quenched by adding
1703 glycine at final concentration 0.125 M on ice for 10 min. Dovetail Hi-C libraries were prepared in
1704 a similar manner as described previously (Lieberman-Aiden et al., 2009). Briefly, for each
1705 library, chromatin was fixed in place with formaldehyde in the nucleus and then extracted. Fixed
1706 chromatin was digested with DpnII, the 5' overhangs filled in with biotinylated nucleotides, and
1707 then free blunt ends were ligated. After ligation, crosslinks were reversed and the DNA purified
1708 from protein. Purified DNA was treated to remove biotin that was not internal to ligated
1709 fragments. The DNA was then sheared to ~350 bp mean fragment size and sequencing libraries
1710 were generated using NEBNext Ultra enzymes and Illumina-compatible adapters. Biotin-
1711 containing fragments were isolated using streptavidin beads before PCR enrichment of each
1712 library.

1713

1714 **HiChIP**
1715 HiChIP assay was performed on 5x10^6 post-treated Cre and ICE cells. Frozen cells were
1716 resuspended in 1X PBS and crosslinked with 3mM DSG and 1% formaldehyde. Washed cells
1717 were digested with 0.5 uL MNase in 100 uL of Nuclease digest buffer with MgCl2. Cells were
1718 lysed with 1X RIPA and clarified lysate (approximately 1400 ng) was used for ChIP. The Protein
1719 A/G bead pulldown, proximity ligation, and libraries were prepared as described in the Dovetail
1720 protocol (Dovetail™ HiChIP MNase Kit). Libraries were sequenced on an Illumina HiSeq 4000.
1721 Raw fastq files were aligned using BWA mem with the -5SP HiC options with an index
1722 containing only the 21 main chromosome from the mouse genome release mm10 (available
1723 from the UCSC genome). The aligned paired reads were annotated with pairtools parse

1724   (https://github.com/open2c/pairtools) with the following options --min-mapq 40 --walks-policy

1725   5unique --max-inter-align-gap 30 and the --chroms-path file corresponding to the size of the

1726   chromosome used for the alignment index. The paired reads were further processed to remove

1727   duplicated reads, sorted with unaligned reads removed with the pairtools sort and the pairtools

1728   dedup tools with the basic option to produce an alignment file in the bam format as well as the

1729   location of the valid pair. The valid pairs were finally converted to the .cool and .mcool format

1730   using the cooler cload and cooler zoomify tools (Abdennur and Mirny, 2020) and to the .hic

1731   format using the juicer tool (Durand et al., 2016).

1732

1733   Whole-genome sequencing

1734   Genomic DNA was isolated from snap frozen cells or tissues using DNeasy Blood & Tissue Kit.

1735   The genomic DNA was fragmented by an ultrasonicator Covaris at 500 bp peak and TruSeq

1736   DNA Library Preparation Kit added DNA adaptors to double strand DNA by following the

1737   manufacturer's instructions of Illumina. Deep whole genome sequencing on an Illumina HiSeq

1738   X10 platform were performed at BGI.

1739

1740   RRBS and epigenetic (DNA methylation) clock

1741   RRBS libraries were prepared in two batches. DNA in the first batch was isolated using Quick-

1742   DNA Universal kit (Zymo) and in the second batch using E.Z.N.A. Tissue DNA Kit (Omega Bio-

1743   tek). 100 μl of 10 mM Tris-HCl buffer was used to elute the samples. Incubation with 2 μl of

1744   RNaseA (Life Technologies) was performed for each sample and followed by a purification

1745   using Genomic DNA Clean & Concentrator-10 (Zymo). DNA was eluted in 25 μl of TE buffer (10

1746   mM Tris-HCl, 0.1 mM EDTA, pH 8.0). 100ng of each sample, estimated using using a Qubit 2.0

1747   (Life Technologies), was used to prepare RRBS libraries following the previously reported

1748   protocol (Petkovich et al., 2017). Libraries included 6-10 samples. The first batch of samples

1749   was sequenced on the Illumina HiSeq 2500 platform using 75 bp paired-end sequencing with

1750   more than 14 million reads per sample. The second batch was sequenced on the Illumina HiSeq

1751   X Ten using 150 paired-end sequencing with more than 32M reads per sample. To compensate

1752   for the low complexity of RRBS libraries 10-20% of phiX was spiked in.

1753   Raw reads were filtered and mapped as previously described (Meer et al., 2018). More than 3.6

1754   M CpG sites were covered in each sample and 2.7M were covered in all samples. Data were

1755 normalized using ComBat from the SVA package in R. Only CpG sites covered in all samples

1756 were considered for DNA methylation clocks application. This resulted in 89 out of 90 sites

1757 being covered for the blood DNA methylation clock. Increase of the threshold for the CpG sites

1758 coverage decreased the number of the clock sites included in the analysis.

1759

1760 **Histone mass spectrometry**

1761 Histone extraction and qMS were performed as previously described (Luense et al., 2016). Acid-

1762 extracted histones were propionylated, trypsin-digested and stage-tip desalted with C18 mini-

1763 disks. Desalted histone peptides were separated by reversed-phase HPLC on a Thermo

1764 Scientific™ EASY-nLC 1000 system. Histone peptide quantified as described (Luense et al.,

1765 2016).

1766

1767 **ChIP-sequencing analysis methods**

1768

1769 **Aligning reads**

1770 The techniques described for processing the ChIP-seq and ATAC-seq reads are based on

1771 ENCODE/Roadmap guidelines with a few modifications (Gjoneska et al., 2015; Landt et al.,

1772 2012; Roadmap Epigenomics et al., 2015). The reads were aligned to the mm10 (GRCm38)

1773 genome (Cunningham et al., 2019) using Bowtie 2 (Langmead and Salzberg, 2012). The

1774 genome fasta files were first indexed and then aligned using the command: bowtie2 -x

1775 /directory/with/reference/genome/rootfilename --fast -U /directoryTree/fastq/SAMPLE.fastq -S

1776 /directoryTree/fastq/SAMPLE.sam, where SAMPLE was replaced with a unique sample

1777 identifier. Following alignment to the genome, the reads were converted from SAM to BAM

1778 format (Li et al., 2009). Low quality reads and reads (q < 20) that did not map to the genome

1779 were removed. For visualization and peak calling, the bamToBed command line tool was used

1780 to convert the BAM files to a modified BED format, called TAGALIGN, which preserved only the

1781 read coordinates (Landt et al., 2012; Quinlan and Hall, 2010).

1782

1783 **Spike-in controls**

1784 Equal amounts of D. Melanogaster DNA were spiked-into ChIP-seq samples. In addition to

1785 aligning to the mouse genome, we aligned reads to the D. Melanogaster dm6 genome

61

1786 (Cunningham et al., 2019). To provide a sense of total ChIP-seq signal strength, the proportion
1787 of reads aligning to the dm6 genome were compared to the proportion aligning to the mouse
1788 genome (Orlando et al., 2014). To compare Cre and ICE mice, a student's t-test was used on
1789 those proportions.
1790

1791 **Visualizing read coverage**
1792 For visualizing individual samples, the genomecov tool within BedTools was used to convert
1793 from the BED format to a BEDGRAPH format (Quinlan and Hall, 2010). Finally, the BEDGRAPH
1794 file was converted to the more efficient BIGWIG format using the UCSC command line tool
1795 bedGraphToBigWig (Kent et al., 2010; Speir et al., 2016). The information was uploaded to the
1796 NCBI sequence read archive and SRA files representing the raw reads, the BAM file
1797 representing the aligned reads, and the BigWig files of read coverage across the genome.
1798

1799 **Visualizing signal relative to background**
1800 Macs2 bdgcmp command was used to calculate the signal to noise ratio for every position in the
1801 genome for each combination of histone modification and experimental condition (Cre and ICE)
1802 (Feng et al., 2012). The BEDGRAPH file was converted to the more efficient BIGWIG format
1803 using the UCSC command line tool bedGraphToBigWig (Speir et al., 2016).
1804

1805 **Quantification and statistical analysis**
1806

1807 **Peak Calling**
1808 For each epigenetic measurement (H3K27ac, H3K56ac, H3K27me3, ATAC-seq) and input
1809 samples, the TAGALIGN files were merged using the unix command zcat and sorted using the
1810 unix sort command according to the chromosome using the start position. For each histone
1811 modification, MACS2 was used to call the peaks relative to the input control: macs2 callpeak -t
1812 H3K27ac.tagAlign.gz -f BED -c input.tagAlign.gz -n H3K27ac_signal -g mm -p 1e-2 --nomodel --
1813 extsize 73 -B –SPMR (Feng et al., 2012). For ATAC-Seq, no input control was used. We
1814 removed peaks with significance (signal relative to noise) of $p > 10^{-5}$. Peaks that fell into the
1815 ENCODE blacklist regions were removed (Landt et al., 2012). The output of the program is a
1816 BED file with peak coordinates for the mm10 version of the mouse genome.

62

1817

Peak annotation

1818 **Peak annotation**

1819 Peaks are annotated based on their mapping to the nearest transcription start site, which was

1820 performed using BEDTools closestBed command (Quinlan and Hall, 2010) based on ENSEMBL

1821 gene annotations, GRCm38 version 79 (Cunningham et al., 2019).

1822

1823 **Counting reads across peaks**

1824 For each histone modification and ATAC-seq sample, the reads from each experiment are

1825 counted in the called peaks using featureCounts in the subread package (Liao et al., 2013). To

1826 perform the counting the peak BED file were converted to SAF format.

1827

1828 **Differential peaks between Cre and ICE**

1829 The negative binomial model in the DESeq2 R package was used to identify differential peaks

1830 between the CRE and ICE mice (Love et al., 2014). For MEF experiments, we used a stringent

1831 threshold of adjusted $p < 0.01$. For muscle ChIP-Seq experiments, very few peaks attained

1832 significance levels at that cutoff. Therefore, we restricted our analysis to looking at the group of

1833 peaks enriched at $p < 0.01$. The varianceStabilizingTransformation function in the DESeq2

1834 package was used to normalize the read counts per peak. Sex chromosomes were excluded

1835 from analyses due to the inconsistency of the sexes of the MEFs.

1836

1837 **ChIP-seq metaplots and heatmaps**

1838 Metaplots and heatmaps were produced using deepTools version 3.0.1 (Ramirez et al., 2016).

1839 Intermediate matrix files were generated by applying computeMatrix (scale-regions mode) to

1840 BIGWIG files over genomic loci in BED format. plotProfile and plotHeatmap functions were

1841 applied to the matrix files to generate output data used to graph each metaplot and heatmap.

1842

1843 **Gene ontology of ChIP-seq differential peaks**

1844 Gene ontology analysis for ChIP-seq were performed using Genomic Regions Enrichment of

1845 Annotations Tool (GREAT) (McLean et al., 2010). Genomic coordinates of differential ChIP-seq

1846 regions and all ChIP-seq peaks were used as test regions and background regions,

1847 respectively. GO biological processes were ranked by HyperFdrQ and only GO terms made up

1848 of at least 5 genes were included. ChIP-seq data were also analyzed using ChIP-Enrich (Welch

1849 et al., 2014). GO terms with at least 5 genes were ranked by FDR.

1850

1851 Hi-C analysis

1852 Paired-end reads were aligned with bwa mem (v0.7.17) (Li and Durbin, 2009) using the options

1853 -S -P. Interaction were parsed and deduplicated with pairsamtools (v0.0.1). Pairwise interaction

1854 frequencies were binned in 50-kb nonoverlapping windows and intra-chromosome interaction

1855 frequencies were normalized by dividing each interaction by the average number of interactions

1856 observed with that distance. Normalized interaction matrices were binned with smoothMat

1857 (Yang et al., 2017). Matrix pearson's correlations were calculated in R v 3.6.1 (Bunn, 2008,

1858 2010) and used to perform a principal component analysis. The sign of the first eigenvector for

1859 each chromosome was adjusted to correlate with GC content, and were smoothed with loess

1860 smoothing using 1 megabase windows.

1861

1862 Whole-genome sequencing analysis

1863 Whole-Genome raw sequencing reads from paired-end library was quality-controlled with

1864 FastQC and subsequently mapped to the reference genome GRCm38/mm10 (mm10) using the

1865 Burrows–Wheeler Alignment (BWA-MEM, version 0.7.17) (Li et al., 2009). A paired-end

1866 mapping strategy with default parameters was utilized. After mapping, the reads were sorted

1867 and converted into binary alignment format (BAM) via Sequence Alignment/Map tools

1868 (SAMtools, version 1.9). The best practices recommended by the Broad Institute for variant

1869 calling were then followed (Van der Auwera et al., 2013). The sorted binary alignments

1870 underwent post-processing to remove duplicates via Picard's MarkDuplicates (v.2.01;

1871 http://broadinstitute.github.io/picard) before germline variants were identified using Genome

1872 Analysis Toolkit (GATK; v. 3.7) HaplotypeCaller (McKenna et al., 2010).

1873

1874 Muscle RNA-seq analysis

1875 Paired-end reads from gastrocnemius muscle RNA-Seq were mapped to the UCSC mm10

1876 genome build using HISAT2 version 2.1.0 (Kim et al., 2015). The featureCounts function from

1877 the Rsubread package (Rsubread 1.32.2) was used to collect read counts for genes. DESeq2

1878 (DESeq2 1.22.2) was applied for differential expression analysis to all genes with rowSums >=
1879 10.

1880 To compare gene expression in gastrocnemius muscles of ICE, Cre, and WT, a table of
1881 normalized read counts was exported from a combined DESeq dataset with all replicates and
1882 conditions. The 200 genes with the smallest adjusted p-value for differential expression between
1883 Cre and ICE were selected and ordered by the log2-fold-change difference between Cre and
1884 Ice. The heatmap.2 (gplots 3.0.1) R function was used to produce a plot of Z-score values for
1885 each gene.

1886

1887 **Epigenetic clock (DNAme age)**
1888 Tissue samples were immediately preserved in DNA/RNA Shield™ (Zymo Research; Cat. No.
1889 R1100-50) and genomic DNA were purified using Quick-DNA Plus Kit (Zymo Research; Cat.
1890 No. D4068) according to manufacturer's instructions. Sample library preparation and data
1891 analyses were performed by Zymo Research, CA. Briefly, genomic DNA (200 ng) was bisulfite-
1892 converted using EZ DNA Methylation-Lightning™ Kit (Zymo Research; Cat. No. D5030).
1893 Bisulfite-converted DNA libraries for targeted bisulfite sequencing platform, called SWARM®
1894 (Simplified Whole-panel Amplification Reaction Method) were prepared according the to the
1895 manufacturer's instructions, then sequenced on a HiSeq 1500 sequencer at >1,000X coverage.
1896 Sequence reads were identified using Illumina basecalling software and aligned to the reference
1897 genome using Bismark (http://www.bioinformatics.babraham.ac.uk/projects/bismark/), an aligner
1898 optimized for bisulfite sequence data and methylation calling . The methylation level of each
1899 sampled cytosine was estimated as the number of reads reporting a C, divided by the total
1900 number of reads reporting a C or T. DNA methylation levels of >500 age-related CpG loci were
1901 used for age prediction using epigenetic age algorithms.

1902

1903 **Data availability**
1904 All sequencing data are available through the BioSample database (NCBI) under BioProject ID:
1905 PRJNA554729.

1906

1907

1908 **Supplemental Information**

65

1909

1918

1919

1920

1921

1922

1923

1924

1925   **REFERENCES**

1926
1927   Abdennur, N., and Mirny, L.A. (2020). Cooler: scalable storage for Hi-C data and other

1928   genomically labeled arrays. Bioinformatics (Oxford, England) *36*, 311-316.

1929   Ackert-Bicknell, C.L., Anderson, L.C., Sheehan, S., Hill, W.G., Chang, B., Churchill, G.A.,

1930   Chesler, E.J., Korstanje, R., and Peters, L.L. (2015). Aging Research Using Mouse Models.

1931   Current protocols in mouse biology *5*, 95-133.

1932   Baruch, K., Deczkowska, A., David, E., Castellano, J.M., Miller, O., Kertser, A., Berkutzki, T.,

1933   Barnett-Itzhaki, Z., Bezalel, D., Wyss-Coray, T.*, et al.* (2014). Aging. Aging-induced type I

1934   interferon response at the choroid plexus negatively affects brain function. Science (New York,

1935   NY) *346*, 89-93.

1936 Beggs, M.L., Nagarajan, R., Taylor-Jones, J.M., Nolen, G., Macnicol, M., and Peterson, C.A.
1937 (2004). Alterations in the TGFbeta signaling pathway in myogenic progenitors with age. Aging
1938 cell *3*, 353-361.

1939 Benayoun, B.A., Pollina, E.A., and Brunet, A. (2015). Epigenetic regulation of ageing: linking
1940 environmental inputs to genomic stability. Nature reviews Molecular cell biology *16*, 593-610.

1941 Benayoun, B.A., Pollina, E.A., Singh, P.P., Mahmoudi, S., Harel, I., Casey, K.M., Dulken, B.W.,
1942 Kundaje, A., and Brunet, A. (2019). Remodeling of epigenome and transcriptome landscapes
1943 with aging in mice reveals widespread induction of inflammatory responses. Genome research
1944 *29*, 697-709.

1945 Berkovich, E., Monnat, R.J., Jr., and Kastan, M.B. (2007). Roles of ATM and NBS1 in chromatin
1946 structure modulation and DNA double-strand break repair. Nature cell biology *9*, 683-690.

1947 Brack, A.S., Conboy, M.J., Roy, S., Lee, M., Kuo, C.J., Keller, C., and Rando, T.A. (2007).
1948 Increased Wnt signaling during aging alters muscle stem cell fate and increases fibrosis.
1949 Science (New York, NY) *317*, 807-810.

1950 Brown, M.F., and Stuart, J.A. (2007). Correlation of mitochondrial superoxide dismutase and
1951 DNA polymerase beta in mammalian dermal fibroblasts with species maximal lifespan.
1952 Mechanisms of ageing and development *128*, 696-705.

1953 Bunn, A.G. (2008). A dendrochronology program library in R (dplR). Dendrochronologia *26*, 115-
1954 124.

1955 Bunn, A.G. (2010). Statistical and visual crossdating in R using the dplR library.
1956 Dendrochronologia *28*, 251-258.

1957 Burgstaller, J.P., and Brem, G. (2017). Aging of Cloned Animals: A Mini-Review. Gerontology
1958 *63*, 417-425.

1959   Calkins, D.J. (2013). Age-related changes in the visual pathways: blame it on the axon.

1960   Investigative ophthalmology & visual science *54*, Orsf37-41.

1961   Carrero, D., Soria-Valles, C., and López-Otín, C. (2016). Hallmarks of progeroid syndromes:

1962   lessons from mice and reprogrammed cells. Disease Models & Mechanisms *9*, 719-735.

1963   Cawthon, R.M. (2009). Telomere length measurement by a novel monochrome multiplex

1964   quantitative PCR method. Nucleic acids research *37*, e21.

1965   Chailleux, C., Aymard, F., Caron, P., Daburon, V., Courilleau, C., Canitrot, Y., Legube, G., and

1966   Trouche, D. (2014). Quantifying DNA double-strand breaks induced by site-specific

1967   endonucleases in living cells by ligation-mediated purification. Nature protocols *9*, 517-528.

1968   Changolkar, L.N., Singh, G., and Pehrson, J.R. (2008). macroH2A1-dependent silencing of

1969   endogenous murine leukemia viruses. Molecular and cellular biology *28*, 2059-2065.

1970   Cheung, P., Vallania, F., Warsinske, H.C., Donato, M., Schaffert, S., Chang, S.E., Dvorak, M.,

1971   Dekker, C.L., Davis, M.M., Utz, P.J.*, et al.* (2018). Single-Cell Chromatin Modification Profiling

1972   Reveals Increased Epigenetic Variations with Aging. Cell *173*, 1385-1397 e1314.

1973   Chiarle, R., Zhang, Y., Frock, R.L., Lewis, S.M., Molinie, B., Ho, Y.J., Myers, D.R., Choi, V.W.,

1974   Compagno, M., Malkin, D.J.*, et al.* (2011). Genome-wide translocation sequencing reveals

1975   mechanisms of chromosome breaks and rearrangements in B cells. Cell *147*, 107-119.

1976   Choudhury, A.R., Ju, Z., Djojosubroto, M.W., Schienke, A., Lechel, A., Schaetzlein, S., Jiang,

1977   H., Stepczynska, A., Wang, C., Buer, J.*, et al.* (2007). Cdkn1a deletion improves stem cell

1978   function and lifespan of mice with dysfunctional telomeres without accelerating cancer

1979   formation. Nature genetics *39*, 99-105.

1980   Cunningham, F., Achuthan, P., Akanni, W., Allen, J., Amode, M.R., Armean, I.M., Bennett, R.,

1981   Bhai, J., Billis, K., Boddu, S.*, et al.* (2019). Ensembl 2019. Nucleic acids research *47*, D745-

1982   D751.

1983 Dang, W., Steffen, K.K., Perry, R., Dorsey, J.A., Johnson, F.B., Shilatifard, A., Kaeberlein, M.,
1984 Kennedy, B.K., and Berger, S.L. (2009). Histone H4 lysine 16 acetylation regulates cellular
1985 lifespan. Nature *459*, 802-807.

1986 Das, A., Huang, G.X., Bonkowski, M.S., Longchamp, A., Li, C., Schultz, M.B., Kim, L.J.,
1987 Osborne, B., Joshi, S., Lu, Y.*, et al.* (2019). Impairment of an Endothelial NAD(+)-H2S Signaling
1988 Network Is a Reversible Cause of Vascular Aging. Cell *176*, 944-945.

1989 De Cecco, M., Criscione, S.W., Peckham, E.J., Hillenmeyer, S., Hamm, E.A., Manivannan, J.,
1990 Peterson, A.L., Kreiling, J.A., Neretti, N., and Sedivy, J.M. (2013). Genomes of replicatively
1991 senescent cells undergo global epigenetic changes leading to gene silencing and activation of
1992 transposable elements. Aging cell *12*, 247-256.

1993 De Cecco, M., Ito, T., Petrashen, A.P., Elias, A.E., Skvir, N.J., Criscione, S.W., Caligiana, A.,
1994 Brocculi, G., Adney, E.M., Boeke, J.D.*, et al.* (2019). L1 drives IFN in senescent cells and
1995 promotes age-associated inflammation. Nature *566*, 73-78.

1996 Demontis, F., Piccirillo, R., Goldberg, A.L., and Perrimon, N. (2013). Mechanisms of skeletal
1997 muscle aging: insights from Drosophila and mammalian models. Disease Models
1998 & Mechanisms *6*, 1339-1352.

1999 Dobbin, M.M., Madabhushi, R., Pan, L., Chen, Y., Kim, D., Gao, J., Ahanonu, B., Pao, P.C., Qiu,
2000 Y., Zhao, Y.*, et al.* (2013). SIRT1 collaborates with ATM and HDAC1 to maintain genomic
2001 stability in neurons. Nature neuroscience *16*, 1008-1015.

2002 Dolle, M.E., Busuttil, R.A., Garcia, A.M., Wijnhoven, S., van Drunen, E., Niedernhofer, L.J., van
2003 der Horst, G., Hoeijmakers, J.H., van Steeg, H., and Vijg, J. (2006). Increased genomic
2004 instability is not a prerequisite for shortened lifespan in DNA repair deficient mice. Mutation
2005 research *596*, 22-35.

69

2006 Dolle, M.E., Giese, H., Hopkins, C.L., Martus, H.J., Hausdorff, J.M., and Vijg, J. (1997). Rapid
2007 accumulation of genome rearrangements in liver but not in brain of old mice. Nature genetics
2008 *17*, 431-434.

2009 Downs, J.C. (2015). Optic nerve head biomechanics in aging and disease. Experimental eye
2010 research *133*, 19-29.

2011 Durand, N.C., Shamim, M.S., Machol, I., Rao, S.S., Huntley, M.H., Lander, E.S., and Aiden, E.L.
2012 (2016). Juicer Provides a One-Click System for Analyzing Loop-Resolution Hi-C Experiments.
2013 Cell systems *3*, 95-98.

2014 Feltes, B.C. (2019). Architects meets Repairers: The interplay between homeobox genes and
2015 DNA repair. DNA repair *73*, 34-48.

2016 Feng, J., Liu, T., Qin, B., Zhang, Y., and Liu, X.S. (2012). Identifying ChIP-seq enrichment using
2017 MACS. Nature protocols *7*, 1728-1740.

2018 Ferguson, V.L., Ayers, R.A., Bateman, T.A., and Simske, S.J. (2003). Bone development and
2019 age-related bone loss in male C57BL/6J mice. Bone *33*, 387-398.

2020 Feser, J., Truong, D., Das, C., Carson, J.J., Kieft, J., Harkness, T., and Tyler, J.K. (2010).
2021 Elevated histone expression promotes life span extension. Molecular cell *39*, 724-735.

2022 Field, A.E., Robertson, N.A., Wang, T., Havas, A., Ideker, T., and Adams, P.D. (2018). DNA
2023 Methylation Clocks in Aging: Categories, Causes, and Consequences. Molecular cell *71*, 882-
2024 895.

2025 Florian, M.C., Nattamai, K.J., Dorr, K., Marka, G., Uberle, B., Vas, V., Eckl, C., Andra, I.,
2026 Schiemann, M., Oostendorp, R.A.*, et al.* (2013). A canonical to non-canonical Wnt signalling
2027 switch in haematopoietic stem-cell ageing. Nature *503*, 392-396.

2028   Freund, A., Laberge, R.M., Demaria, M., and Campisi, J. (2012). Lamin B1 loss is a
2029   senescence-associated biomarker. Molecular biology of the cell *23*, 2066-2075.

2030   Gallagher, M., Bakker, A., Yassa, M.A., and Stark, C.E. (2010). Bridging neurocognitive aging
2031   and disease modification: targeting functional mechanisms of memory impairment. Current
2032   Alzheimer research *7*, 197-199.

2033   Gao, J., Wang, W.Y., Mao, Y.W., Graff, J., Guan, J.S., Pan, L., Mak, G., Kim, D., Su, S.C., and
2034   Tsai, L.H. (2010). A novel pathway regulates memory and plasticity via SIRT1 and miR-134.
2035   Nature *466*, 1105-1109.

2036   Garlick, P.J., McNurlan, M.A., and Preedy, V.R. (1980). A rapid and convenient technique for
2037   measuring the rate of protein synthesis in tissues by injection of [3H]phenylalanine. The
2038   Biochemical journal *192*, 719-723.

2039   Garrett-Bakelman, F.E., Darshi, M., Green, S.J., Gur, R.C., Lin, L., Macias, B.R., McKenna,
2040   M.J., Meydan, C., Mishra, T., Nasrini, J.*, et al.* (2019). The NASA Twins Study: A
2041   multidimensional analysis of a year-long human spaceflight. Science (New York, NY) *364*.

2042   Gjoneska, E., Pfenning, A.R., Mathys, H., Quon, G., Kundaje, A., Tsai, L.H., and Kellis, M.
2043   (2015). Conserved epigenomic signals in mice and humans reveal immune basis of Alzheimer's
2044   disease. Nature *518*, 365-369.

2045   Gomes, A.P., Price, N.L., Ling, A.J., Moslehi, J.J., Montgomery, M.K., Rajman, L., White, J.P.,
2046   Teodoro, J.S., Wrann, C.D., Hubbard, B.P.*, et al.* (2013). Declining NAD(+) induces a
2047   pseudohypoxic state disrupting nuclear-mitochondrial communication during aging. Cell *155*,
2048   1624-1638.

2049   Gorkin, D.U., Leung, D., and Ren, B. (2014). The 3D genome in transcriptional regulation and
2050   pluripotency. Cell stem cell *14*, 762-775.

2051 Greer, E.L., Maures, T.J., Hauswirth, A.G., Green, E.M., Leeman, D.S., Maro, G.S., Han, S.,
2052 Banko, M.R., Gozani, O., and Brunet, A. (2010). Members of the H3K4 trimethylation complex
2053 regulate lifespan in a germline-dependent manner in C. elegans. Nature *466*, 383-387.

2054 Greer, E.L., Maures, T.J., Ucar, D., Hauswirth, A.G., Mancini, E., Lim, J.P., Benayoun, B.A., Shi,
2055 Y., and Brunet, A. (2011). Transgenerational epigenetic inheritance of longevity in
2056 Caenorhabditis elegans. Nature *479*, 365-371.

2057 Hannum, G., Guinney, J., Zhao, L., Zhang, L., Hughes, G., Sadda, S., Klotzle, B., Bibikova, M.,
2058 Fan, J.B., Gao, Y.*, et al.* (2013). Genome-wide methylation profiles reveal quantitative views of
2059 human aging rates. Molecular cell *49*, 359-367.

2060 Harkema, L., Youssef, S.A., and de Bruin, A. (2016). Pathology of Mouse Models of Accelerated
2061 Aging. Veterinary pathology *53*, 366-389.

2062 Heinz, S., Romanoski, C.E., Benner, C., and Glass, C.K. (2015). The selection and function of
2063 cell type-specific enhancers. Nature reviews Molecular cell biology *16*, 144-154.

2064 Hofmann, J.W., Zhao, X., De Cecco, M., Peterson, A.L., Pagliaroli, L., Manivannan, J., Hubbard,
2065 G.B., Ikeno, Y., Zhang, Y., Feng, B.*, et al.* (2015). Reduced expression of MYC increases
2066 longevity and enhances healthspan. Cell *160*, 477-488.

2067 Hofstatter, E.W., Horvath, S., Dalela, D., Gupta, P., Chagpar, A.B., Wali, V.B., Bossuyt, V.,
2068 Storniolo, A.M., Hatzis, C., Patwardhan, G.*, et al.* (2018). Increased epigenetic age in normal
2069 breast tissue from luminal breast cancer patients. Clinical epigenetics *10*, 112.

2070 Horvath, S. (2013). DNA methylation age of human tissues and cell types. Genome biology *14*,
2071 R115.

2072 Horvath, S., and Levine, A.J. (2015). HIV-1 Infection Accelerates Age According to the
2073 Epigenetic Clock. The Journal of infectious diseases *212*, 1563-1573.

72

2074 Houtkooper, R.H., Argmann, C., Houten, S.M., Canto, C., Jeninga, E.H., Andreux, P.A.,
2075 Thomas, C., Doenlen, R., Schoonjans, K., and Auwerx, J. (2011). The metabolic footprint of
2076 aging in mice. Scientific reports *1*, 134.

2077 Hu, Z., Chen, K., Xia, Z., Chavez, M., Pal, S., Seol, J.H., Chen, C.C., Li, W., and Tyler, J.K.
2078 (2014). Nucleosome loss leads to global transcriptional up-regulation and genomic instability
2079 during yeast aging. Genes & development *28*, 396-408.

2080 Idelevich, A., Sato, K., Nagano, K., Rowe, G., Gori, F., and Baron, R. (2018). Neuronal
2081 hypothalamic regulation of body metabolism and bone density is galanin dependent. The
2082 Journal of clinical investigation *128*, 2626-2641.

2083 Imai, S., and Kitano, H. (1998). Heterochromatin islands and their dynamic reorganization: a
2084 hypothesis for three distinctive features of cellular aging. Experimental gerontology *33*, 555-570.

2085 Jiang, N., Du, G., Tobias, E., Wood, J.G., Whitaker, R., Neretti, N., and Helfand, S.L. (2013).
2086 Dietary and genetic effects on age-related loss of gene silencing reveal epigenetic plasticity of
2087 chromatin repression during aging. Aging *5*, 813-824.

2088 Johnson, S., Wozniak, D.F., and Imai, S. (2018). CA1 Nampt knockdown recapitulates
2089 hippocampal cognitive phenotypes in old mice which nicotinamide mononucleotide improves.
2090 NPJ aging and mechanisms of disease *4*, 10.

2091 Kaeberlein, M., McVey, M., and Guarente, L. (1999). The SIR2/3/4 complex and SIR2 alone
2092 promote longevity in Saccharomyces cerevisiae by two different mechanisms. Genes &
2093 development *13*, 2570-2580.

2094 Kane, A.E., and Sinclair, D.A. (2019). Epigenetic changes during aging and their reprogramming
2095 potential. Critical reviews in biochemistry and molecular biology *54*, 61-83.

2096 Katzman, W.B., Wanek, L., Shepherd, J.A., and Sellmeyer, D.E. (2010). Age-related

2097 hyperkyphosis: its causes, consequences, and management. The Journal of orthopaedic and

2098 sports physical therapy *40*, 352-360.

2099 Kaya, A., Lobanov, A.V., and Gladyshev, V.N. (2015). Evidence that mutation accumulation

2100 does not cause aging in Saccharomyces cerevisiae. Aging cell *14*, 366-371.

2101 Keller, E.F. (2009). Knowing As Making, Making As Knowing: The Many Lives of Synthetic

2102 Biology. Biological Theory *4*, 333-339.

2103 Kennedy, B.K., Gotta, M., Sinclair, D.A., Mills, K., McNabb, D.S., Murthy, M., Pak, S.M.,

2104 Laroche, T., Gasser, S.M., and Guarente, L. (1997). Redistribution of silencing proteins from

2105 telomeres to the nucleolus is associated with extension of life span in S. cerevisiae. Cell *89*,

2106 381-391.

2107 Kent, W.J., Zweig, A.S., Barber, G., Hinrichs, A.S., and Karolchik, D. (2010). BigWig and

2108 BigBed: enabling browsing of large distributed datasets. Bioinformatics (Oxford, England) *26*,

2109 2204-2207.

2110 Kim, D., Langmead, B., and Salzberg, S.L. (2015). HISAT: a fast spliced aligner with low

2111 memory requirements. Nature methods *12*, 357-360.

2112 Klemm, S.L., Shipony, Z., and Greenleaf, W.J. (2019). Chromatin accessibility and the

2113 regulatory epigenome. Nature reviews Genetics *20*, 207-220.

2114 Koks, S., Dogan, S., Tuna, B.G., Gonzalez-Navarro, H., Potter, P., and Vandenbroucke, R.E.

2115 (2016). Mouse models of ageing and their relevance to disease. Mechanisms of ageing and

2116 development *160*, 41-53.

2117 Kundu, S., Ji, F., Sunwoo, H., Jain, G., Lee, J.T., Sadreyev, R.I., Dekker, J., and Kingston, R.E.

2118 (2017). Polycomb Repressive Complex 1 Generates Discrete Compacted Domains that Change

2119 during Differentiation. Molecular cell *65*, 432-446.e435.

74

2120 Landt, S.G., Marinov, G.K., Kundaje, A., Kheradpour, P., Pauli, F., Batzoglou, S., Bernstein,
2121 B.E., Bickel, P., Brown, J.B., Cayting, P*., et al.* (2012). ChIP-seq guidelines and practices of the
2122 ENCODE and modENCODE consortia. Genome research *22*, 1813-1831.

2123 Langmead, B., and Salzberg, S.L. (2012). Fast gapped-read alignment with Bowtie 2. Nature
2124 methods *9*, 357-359.

2125 Le Couteur, D.G., Cogger, V.C., Markus, A.M., Harvey, P.J., Yin, Z.L., Ansselin, A.D., and
2126 McLean, A.J. (2001). Pseudocapillarization and associated energy limitation in the aged rat
2127 liver. Hepatology (Baltimore, Md) *33*, 537-543.

2128 Leduc-Gaudet, J.P., Picard, M., St-Jean Pelletier, F., Sgarioto, N., Auger, M.J., Vallee, J.,
2129 Robitaille, R., St-Pierre, D.H., and Gouspillou, G. (2015). Mitochondrial morphology is altered in
2130 atrophied skeletal muscle of aged mice. Oncotarget *6*, 17923-17937.

2131 Lee, S.E., Paques, F., Sylvan, J., and Haber, J.E. (1999). Role of yeast SIR genes and mating
2132 type in directing DNA double-strand breaks to homologous and non-homologous repair paths.
2133 Current biology : CB *9*, 767-770.

2134 Li, H., Coghlan, A., Ruan, J., Coin, L.J., Heriche, J.K., Osmotherly, L., Li, R., Liu, T., Zhang, Z.,
2135 Bolund, L*., et al.* (2006). TreeFam: a curated database of phylogenetic trees of animal gene
2136 families. Nucleic acids research *34*, D572-580.

2137 Li, H., and Durbin, R. (2009). Fast and accurate short read alignment with Burrows-Wheeler
2138 transform. Bioinformatics (Oxford, England) *25*, 1754-1760.

2139 Li, H., Handsaker, B., Wysoker, A., Fennell, T., Ruan, J., Homer, N., Marth, G., Abecasis, G.,
2140 Durbin, R., and Genome Project Data Processing, S. (2009). The Sequence Alignment/Map
2141 format and SAMtools. Bioinformatics (Oxford, England) *25*, 2078-2079.

2142   Li, H., Vogel, H., Holcomb, V.B., Gu, Y., and Hasty, P. (2007). Deletion of Ku70, Ku80, or Both

2143   Causes Early Aging without Substantially Increased Cancer. Molecular and cellular biology *27*,

2144   8205-8214.

2145   Li, S., Lu, H., Wang, Z., Hu, Q., Wang, H., Xiang, R., Chiba, T., and Wu, X. (2019). ERCC1/XPF

2146   Is Important for Repair of DNA Double-Strand Breaks Containing Secondary Structures.

2147   iScience *16*, 63-78.

2148   Li, X., Zuo, X., Jing, J., Ma, Y., Wang, J., Liu, D., Zhu, J., Du, X., Xiong, L., Du, Y.*, et al.* (2015).

2149   Small-Molecule-Driven Direct Reprogramming of Mouse Fibroblasts into Functional Neurons.

2150   Cell stem cell *17*, 195-203.

2151   Li, Z., Zhang, W., Chen, Y., Guo, W., Zhang, J., Tang, H., Xu, Z., Zhang, H., Tao, Y., Wang, F.*,*

2152   *et al.* (2016). Impaired DNA double-strand break repair contributes to the age-associated rise of

2153   genomic instability in humans. Cell death and differentiation *23*, 1765-1777.

2154   Liao, Y., Smyth, G.K., and Shi, W. (2013). The Subread aligner: fast, accurate and scalable read

2155   mapping by seed-and-vote. Nucleic acids research *41*, e108.

2156   Lieberman-Aiden, E., van Berkum, N.L., Williams, L., Imakaev, M., Ragoczy, T., Telling, A.,

2157   Amit, I., Lajoie, B.R., Sabo, P.J., Dorschner, M.O.*, et al.* (2009). Comprehensive mapping of

2158   long-range interactions reveals folding principles of the human genome. Science (New York,

2159   NY) *326*, 289-293.

2160   Lim, M.A., Defensor, E.B., Mechanic, J.A., Shah, P.P., Jaime, E.A., Roberts, C.R., Hutto, D.L.,

2161   and Schaevitz, L.R. (2019). Retrospective Analysis of the Effects of Identification Procedures

2162   and Cage Changing by Using Data from Automated, Continuous Monitoring. Journal of the

2163   American Association for Laboratory Animal Science : JAALAS *58*, 126-141.

2164   Lim, M.A., Louie, B., Ford, D., Heath, K., Cha, P., Betts-Lacroix, J., Lum, P.Y., Robertson, T.L.,

2165   and Schaevitz, L. (2017). Development of the Digital Arthritis Index, a Novel Metric to Measure

2166   Disease Parameters in a Rat Model of Rheumatoid Arthritis. Frontiers in pharmacology *8*, 818.

2167 Lin, I.H., Chang, J.L., Hua, K., Huang, W.C., Hsu, M.T., and Chen, Y.F. (2018). Skeletal muscle
2168 in aged mice reveals extensive transformation of muscle gene expression. BMC genetics *19*,
2169 55.

2170 Liu, N., Matsumura, H., Kato, T., Ichinose, S., Takada, A., Namiki, T., Asakawa, K., Morinaga,
2171 H., Mohri, Y., De Arcangelis, A.*, et al.* (2019). Stem cell competition orchestrates skin
2172 homeostasis and ageing. Nature *568*, 344-350.

2173 Love, M.I., Huber, W., and Anders, S. (2014). Moderated estimation of fold change and
2174 dispersion for RNA-seq data with DESeq2. Genome biology *15*, 550.

2175 Lu, A.T., Fei, Z., Haghani, A., Robeck, T.R., Zoller, J.A., Li, C.Z., Zhang, J., Ablaeva, J., Adams,
2176 D.M., Almunia, J.*, et al.* (2021). Universal DNA methylation age across mammalian tissues.
2177 bioRxiv, 2021.2001.2018.426733.

2178 Lu, Y., Brommer, B., Tian, X., Krishnan, A., Meer, M., Wang, C., Vera, D.L., Zeng, Q., Yu, D.,
2179 Bonkowski, M.S.*, et al.* (2020). Reprogramming to recover youthful epigenetic information and
2180 restore vision. Nature *588*, 124-129.

2181 Luense, L.J., Wang, X., Schon, S.B., Weller, A.H., Lin Shiao, E., Bryant, J.M., Bartolomei, M.S.,
2182 Coutifaris, C., Garcia, B.A., and Berger, S.L. (2016). Comprehensive analysis of histone post-
2183 translational modifications in mouse and human male germ cells. Epigenetics & chromatin *9*, 24.

2184 Luna, L.G. (1968). Manual of histologic staining methods of the Armed Forces Institute of
2185 Pathology (Third edition. New York : Blakiston Division, McGraw-Hill, [1968] ©1968).

2186 Maccormick, R.E. (2006). Possible acceleration of aging by adjuvant chemotherapy: a cause of
2187 early onset frailty? Medical hypotheses *67*, 212-215.

2188 Mao, Z., Hine, C., Tian, X., Van Meter, M., Au, M., Vaidya, A., Seluanov, A., and Gorbunova, V.
2189 (2011). SIRT6 promotes DNA repair under stress by activating PARP1. Science (New York, NY)
2190 *332*, 1443-1446.

2191 Mapuskar, K.A., Flippo, K.H., Schoenfeld, J.D., Riley, D.P., Strack, S., Hejleh, T.A., Furqan, M.,

2192 Monga, V., Domann, F.E., Buatti, J.M., *et al.* (2017). Mitochondrial Superoxide Increases Age-

2193 Associated Susceptibility of Human Dermal Fibroblasts to Radiation and Chemotherapy. Cancer

2194 research *77*, 5054-5067.

2195 Martin, S.G., Laroche, T., Suka, N., Grunstein, M., and Gasser, S.M. (1999). Relocalization of

2196 telomeric Ku and SIR proteins in response to DNA strand breaks in yeast. Cell *97*, 621-633.

2197 Matsumura, H., Mohri, Y., Binh, N.T., Morinaga, H., Fukuda, M., Ito, M., Kurata, S.,

2198 Hoeijmakers, J., and Nishimura, E.K. (2016). Hair follicle aging is driven by transepidermal

2199 elimination of stem cells via COL17A1 proteolysis. Science (New York, NY) *351*, aad4395.

2200 McAinsh, A.D., Scott-Drew, S., Murray, J.A., and Jackson, S.P. (1999). DNA damage triggers

2201 disruption of telomeric silencing and Mec1p-dependent relocation of Sir3p. Current biology : CB

2202 *9*, 963-966.

2203 McCord, R.A., Michishita, E., Hong, T., Berber, E., Boxer, L.D., Kusumoto, R., Guan, S., Shi, X.,

2204 Gozani, O., Burlingame, A.L., *et al.* (2009). SIRT6 stabilizes DNA-dependent protein kinase at

2205 chromatin for DNA double-strand break repair. Aging *1*, 109-121.

2206 McKenna, A., Hanna, M., Banks, E., Sivachenko, A., Cibulskis, K., Kernytsky, A., Garimella, K.,

2207 Altshuler, D., Gabriel, S., Daly, M., *et al.* (2010). The Genome Analysis Toolkit: a MapReduce

2208 framework for analyzing next-generation DNA sequencing data. Genome research *20*, 1297-

2209 1303.

2210 McLean, C.Y., Bristor, D., Hiller, M., Clarke, S.L., Schaar, B.T., Lowe, C.B., Wenger, A.M., and

2211 Bejerano, G. (2010). GREAT improves functional interpretation of cis-regulatory regions. Nature

2212 biotechnology *28*, 495-501.

2213 Medawar, P.B. (1952). An unsolved problem of biology (Published for the College by H.K.

2214 Lewis).

2215 Meer, M.V., Podolskiy, D.I., Tyshkovskiy, A., and Gladyshev, V.N. (2018). A whole lifespan
2216 mouse multi-tissue DNA methylation clock. eLife 7.

2217 Miller, D.B., and O'Callaghan, J.P. (2005). Aging, stress and the hippocampus. Ageing research
2218 reviews 4, 123-140.

2219 Mills, K.D., Sinclair, D.A., and Guarente, L. (1999). MEC1-dependent redistribution of the Sir3
2220 silencing protein from telomeres to DNA double-strand breaks. Cell 97, 609-620.

2221 Miyoshi, N., Oubrahim, H., Chock, P.B., and Stadtman, E.R. (2006). Age-dependent cell death
2222 and the role of ATP in hydrogen peroxide-induced apoptosis and necrosis. Proceedings of the
2223 National Academy of Sciences of the United States of America 103, 1727-1731.

2224 Monnat, R.J., Jr., Hackmann, A.F., and Cantrell, M.A. (1999). Generation of highly site-specific
2225 DNA double-strand breaks in human cells by the homing endonucleases I-PpoI and I-CreI.
2226 Biochemical and biophysical research communications 255, 88-93.

2227 Mosammaparast, N., Kim, H., Laurent, B., Zhao, Y., Lim, H.J., Majid, M.C., Dango, S., Luo, Y.,
2228 Hempel, K., Sowa, M.E., et al. (2013). The histone demethylase LSD1/KDM1A promotes the
2229 DNA damage response. The Journal of cell biology 203, 457-470.

2230 Nance, M.A., and Berry, S.A. (1992). Cockayne syndrome: Review of 140 cases. American
2231 Journal of Medical Genetics 42, 68-84.

2232 Narayanan, L., Fritzell, J.A., Baker, S.M., Liskay, R.M., and Glazer, P.M. (1997). Elevated levels
2233 of mutation in multiple tissues of mice deficient in the DNA mismatch repair gene Pms2.
2234 Proceedings of the National Academy of Sciences of the United States of America 94, 3122-
2235 3127.

2236 Narendra, V., Rocha, P.P., An, D., Raviram, R., Skok, J.A., Mazzoni, E.O., and Reinberg, D.
2237 (2015). CTCF establishes discrete functional chromatin domains at the Hox clusters during
2238 differentiation. Science (New York, NY) 347, 1017-1021.

2239 Niedernhofer, L.J., Garinis, G.A., Raams, A., Lalai, A.S., Robinson, A.R., Appeldoorn, E., Odijk,
2240 H., Oostendorp, R., Ahmad, A., van Leeuwen, W.*, et al.* (2006). A new progeroid syndrome
2241 reveals that genotoxic stress suppresses the somatotroph axis. Nature *444*, 1038-1043.

2242 Nishimura, E.K., Granter, S.R., and Fisher, D.E. (2005). Mechanisms of Hair Graying:
2243 Incomplete Melanocyte Stem Cell Maintenance in the Niche. Science (New York, NY) *307*, 720-
2244 724.

2245 Norden, D.M., and Godbout, J.P. (2013). Review: microglia of the aged brain: primed to be
2246 activated and resistant to regulation. Neuropathology and applied neurobiology *39*, 19-34.

2247 Oberdoerffer, P., Michan, S., McVay, M., Mostoslavsky, R., Vann, J., Park, S.K., Hartlerode, A.,
2248 Stegmuller, J., Hafner, A., Loerch, P.*, et al.* (2008). SIRT1 redistribution on chromatin promotes
2249 genomic stability but alters gene expression during aging. Cell *135*, 907-918.

2250 Oberdoerffer, P., and Sinclair, D.A. (2007). The role of nuclear architecture in genomic instability
2251 and ageing. Nature reviews Molecular cell biology *8*, 692-702.

2252 Ocampo, A., Reddy, P., Martinez-Redondo, P., Platero-Luengo, A., Hatanaka, F., Hishida, T.,
2253 Li, M., Lam, D., Kurita, M., Beyret, E.*, et al.* (2016). In Vivo Amelioration of Age-Associated
2254 Hallmarks by Partial Reprogramming. Cell *167*, 1719-1733.e1712.

2255 Ohse, T., Vaughan, M.R., Kopp, J.B., Krofft, R.D., Marshall, C.B., Chang, A.M., Hudkins, K.L.,
2256 Alpers, C.E., Pippin, J.W., and Shankland, S.J. (2010). De novo expression of podocyte proteins
2257 in parietal epithelial cells during experimental glomerular disease. Am J Physiol Renal Physiol
2258 *298*, F702-711.

2259 Orlando, D.A., Chen, M.W., Brown, V.E., Solanki, S., Choi, Y.J., Olson, E.R., Fritz, C.C.,
2260 Bradner, J.E., and Guenther, M.G. (2014). Quantitative ChIP-Seq normalization reveals global
2261 modulation of the epigenome. Cell reports *9*, 1163-1170.

2262 Pal, S., and Tyler, J.K. (2016). Epigenetics and aging. Science advances *2*, e1600584.

2263   Park, D.C., and Reuter-Lorenz, P. (2009). The adaptive brain: aging and neurocognitive
2264   scaffolding. Annual review of psychology *60*, 173-196.

2265   Petkovich, D.A., Podolskiy, D.I., Lobanov, A.V., Lee, S.G., Miller, R.A., and Gladyshev, V.N.
2266   (2017). Using DNA Methylation Profiling to Evaluate Biological Age and Longevity Interventions.
2267   Cell metabolism *25*, 954-960 e956.

2268   Quinlan, A.R., and Hall, I.M. (2010). BEDTools: a flexible suite of utilities for comparing genomic
2269   features. Bioinformatics (Oxford, England) *26*, 841-842.

2270   Ramirez, F., Ryan, D.P., Gruning, B., Bhardwaj, V., Kilpert, F., Richter, A.S., Heyne, S., Dundar,
2271   F., and Manke, T. (2016). deepTools2: a next generation web server for deep-sequencing data
2272   analysis. Nucleic acids research *44*, W160-165.

2273   Richardson, R.B. (2009). Ionizing radiation and aging: rejuvenating an old idea. Aging *1*, 887-
2274   902.

2275   Roadmap Epigenomics, C., Kundaje, A., Meuleman, W., Ernst, J., Bilenky, M., Yen, A., Heravi-
2276   Moussavi, A., Kheradpour, P., Zhang, Z., Wang, J.*, et al.* (2015). Integrative analysis of 111
2277   reference human epigenomes. Nature *518*, 317-330.

2278   Roeder, S.S., Barnes, T.J., Lee, J.S., Kato, I., Eng, D.G., Kaverina, N.V., Sunseri, M.W., Daniel,
2279   C., Amann, K., Pippin, J.W.*, et al.* (2017). Activated ERK1/2 increases CD44 in glomerular
2280   parietal epithelial cells leading to matrix expansion. Kidney international *91*, 896-913.

2281   Roeder, S.S., Stefanska, A., Eng, D.G., Kaverina, N., Sunseri, M.W., McNicholas, B.A.,
2282   Rabinovitch, P., Engel, F.B., Daniel, C., Amann, K.*, et al.* (2015). Changes in glomerular parietal
2283   epithelial cells in mouse kidneys with advanced age. Am J Physiol Renal Physiol *309*, F164-
2284   178.

2285 Rogina, B., and Helfand, S.L. (2004). Sir2 mediates longevity in the fly through a pathway

2286 related to calorie restriction. Proceedings of the National Academy of Sciences of the United

2287 States of America *101*, 15998-16003.

2288 Roichman, A., Elhanati, S., Aon, M.A., Abramovich, I., Di Francesco, A., Shahar, Y., Avivi, M.Y.,

2289 Shurgi, M., Rubinstein, A., Wiesner, Y.*, et al.* (2021). Restoration of energy homeostasis by

2290 SIRT6 extends healthy lifespan. Nature communications *12*, 3208.

2291 Rosaleny, L.E., Antunez, O., Ruiz-Garcia, A.B., Perez-Ortin, J.E., and Tordera, V. (2005). Yeast

2292 HAT1 and HAT2 deletions have different life-span and transcriptome phenotypes. FEBS letters

2293 *579*, 4063-4068.

2294 Ross, J.M. (2011). Visualization of mitochondrial respiratory function using cytochrome c

2295 oxidase/succinate dehydrogenase (COX/SDH) double-labeling histochemistry. Journal of

2296 visualized experiments : JoVE, e3266.

2297 Ruan, J., Li, H., Chen, Z., Coghlan, A., Coin, L.J., Guo, Y., Heriche, J.K., Hu, Y., Kristiansen, K.,

2298 Li, R.*, et al.* (2008). TreeFam: 2008 Update. Nucleic acids research *36*, D735-740.

2299 Rubin, E., Wu, X., Zhu, T., Cheung, J.C., Chen, H., Lorincz, A., Pandita, R.K., Sharma, G.G.,

2300 Ha, H.C., Gasson, J.*, et al.* (2007). A role for the HOXB7 homeodomain protein in DNA repair.

2301 Cancer research *67*, 1527-1535.

2302 Ruzankina, Y., Pinzon-Guzman, C., Asare, A., Ong, T., Pontano, L., Cotsarelis, G., Zediak,

2303 V.P., Velez, M., Bhandoola, A., and Brown, E.J. (2007). Deletion of the developmentally

2304 essential gene ATR in adult mice leads to age-related phenotypes and stem cell loss. Cell stem

2305 cell *1*, 113-126.

2306 Ryu, H.Y., Rhie, B.H., and Ahn, S.H. (2014). Loss of the Set2 histone methyltransferase

2307 increases cellular lifespan in yeast cells. Biochemical and biophysical research communications

2308 *446*, 113-118.

2309 Salk, D., Fujiwara, Y., and Martin, G.M. (1985). Werner's Syndrome and Human Aging.

2310 Salzer, M.C., Lafzi, A., Berenguer-Llergo, A., Youssif, C., Castellanos, A., Solanas, G., Peixoto,
2311 F.O., Stephan-Otto Attolini, C., Prats, N., Aguilera, M.*, et al.* (2018). Identity Noise and
2312 Adipogenic Traits Characterize Dermal Fibroblast Aging. Cell *175*, 1575-1590 e1522.

2313 Samuel, M.A., Zhang, Y., Meister, M., and Sanes, J.R. (2011). Age-related alterations in
2314 neurons of the mouse retina. The Journal of neuroscience : the official journal of the Society for
2315 Neuroscience *31*, 16033-16044.

2316 Schneider, R.R., Eng, D.G., Kutz, J.N., Sweetwyne, M.T., Pippin, J.W., and Shankland, S.J.
2317 (2017). Compound effects of aging and experimental FSGS on glomerular epithelial cells. Aging
2318 *9*, 524-546.

2319 Schoenfelder, S., Sugar, R., Dimond, A., Javierre, B.M., Armstrong, H., Mifsud, B., Dimitrova,
2320 E., Matheson, L., Tavares-Cadete, F., Furlan-Magaril, M.*, et al.* (2015). Polycomb repressive
2321 complex PRC1 spatially constrains the mouse embryonic stem cell genome. Nature genetics *47*,
2322 1179-1186.

2323 Schworer, S., Becker, F., Feller, C., Baig, A.H., Kober, U., Henze, H., Kraus, J.M., Xin, B.,
2324 Lechel, A., Lipka, D.B.*, et al.* (2016). Epigenetic stress responses induce muscle stem-cell
2325 ageing by Hoxa9 developmental signals. Nature *540*, 428-432.

2326 Sen, P., Dang, W., Donahue, G., Dai, J., Dorsey, J., Cao, X., Liu, W., Cao, K., Perry, R., Lee,
2327 J.Y.*, et al.* (2015). H3K36 methylation promotes longevity by enhancing transcriptional fidelity.
2328 Genes & development *29*, 1362-1376.

2329 Sen, P., Shah, P.P., Nativio, R., and Berger, S.L. (2016). Epigenetic Mechanisms of Longevity
2330 and Aging. Cell *166*, 822-839.

2331 Shah, P.P., Donahue, G., Otte, G.L., Capell, B.C., Nelson, D.M., Cao, K., Aggarwala, V.,
2332 Cruickshanks, H.A., Rai, T.S., McBryan, T.*, et al.* (2013). Lamin B1 depletion in senescent cells

83

2333 triggers large-scale changes in gene expression and the chromatin landscape. Genes &
2334 development *27*, 1787-1799.

2335 Simon, M., Van Meter, M., Ablaeva, J., Ke, Z., Gonzalez, R.S., Taguchi, T., De Cecco, M.,
2336 Leonova, K.I., Kogan, V., Helfand, S.L.*, et al.* (2019). LINE1 Derepression in Aged Wild-Type
2337 and SIRT6-Deficient Mice Drives Inflammation. Cell metabolism *29*, 871-885 e875.

2338 Sinclair, D.A., and LaPlante, M.D. (2019). Lifespan: Why We Age—and Why We Don't Have To
2339 (Atria Books).

2340 Sinclair, D.A., Mills, K., and Guarente, L. (1997). Accelerated aging and nucleolar fragmentation
2341 in yeast sgs1 mutants. Science (New York, NY) *277*, 1313-1316.

2342 Singh, S.K., Williams, C.A., Klarmann, K., Burkett, S.S., Keller, J.R., and Oberdoerffer, P.
2343 (2013). Sirt1 ablation promotes stress-induced loss of epigenetic and genomic hematopoietic
2344 stem and progenitor cell maintenance. The Journal of experimental medicine *210*, 987-1001.

2345 Smeal, T., Claus, J., Kennedy, B., Cole, F., and Guarente, L. (1996). Loss of transcriptional
2346 silencing causes sterility in old mother cells of S. cerevisiae. Cell *84*, 633-642.

2347 Speir, M.L., Zweig, A.S., Rosenbloom, K.R., Raney, B.J., Paten, B., Nejad, P., Lee, B.T.,
2348 Learned, K., Karolchik, D., Hinrichs, A.S.*, et al.* (2016). The UCSC Genome Browser database:
2349 2016 update. Nucleic acids research *44*, D717-725.

2350 Szilard, L. (1959). ON THE NATURE OF THE AGING PROCESS. Proceedings of the National
2351 Academy of Sciences of the United States of America *45*, 30-45.

2352 Takahashi, K., and Yamanaka, S. (2006). Induction of pluripotent stem cells from mouse
2353 embryonic and adult fibroblast cultures by defined factors. Cell *126*, 663-676.

2354   Tamburini, B.A., and Tyler, J.K. (2005). Localized histone acetylation and deacetylation

2355   triggered by the homologous recombination pathway of double-strand DNA repair. Molecular

2356   and cellular biology *25*, 4903-4913.

2357   Tan, L., Ke, Z., Tombline, G., Macoretta, N., Hayes, K., Tian, X., Lv, R., Ablaeva, J., Gilbert, M.,

2358   Bhanu, N.V*., et al.* (2017). Naked Mole Rat Cells Have a Stable Epigenome that Resists iPSC

2359   Reprogramming. Stem cell reports *9*, 1721-1734.

2360   Tian, X., Firsanov, D., Zhang, Z., Cheng, Y., Luo, L., Tombline, G., Tan, R., Simon, M.,

2361   Henderson, S., Steffan, J*., et al.* (2019). SIRT6 Is Responsible for More Efficient DNA Double-

2362   Strand Break Repair in Long-Lived Species. Cell *177*, 622-638 e622.

2363   Tiku, V., Jain, C., Raz, Y., Nakamura, S., Heestand, B., Liu, W., Spath, M., Suchiman, H.E.D.,

2364   Muller, R.U., Slagboom, P.E*., et al.* (2017). Small nucleoli are a cellular hallmark of longevity.

2365   Nature communications *8*, 16083.

2366   Ungvari, Z., Tarantini, S., Hertelendy, P., Valcarcel-Ares, M.N., Fülöp, G.A., Logan, S., Kiss, T.,

2367   Farkas, E., Csiszar, A., and Yabluchanskiy, A. (2017). Cerebromicrovascular dysfunction

2368   predicts cognitive decline and gait abnormalities in a mouse model of whole brain irradiation-

2369   induced accelerated brain senescence. GeroScience *39*, 33-42.

2370   Van der Auwera, G.A., Carneiro, M.O., Hartl, C., Poplin, R., Del Angel, G., Levy-Moonshine, A.,

2371   Jordan, T., Shakir, K., Roazen, D., Thibault, J*., et al.* (2013). From FastQ data to high

2372   confidence variant calls: the Genome Analysis Toolkit best practices pipeline. Current protocols

2373   in bioinformatics *43*, 11.10.11-33.

2374   Venkatareddy, M., Wang, S., Yang, Y., Patel, S., Wickman, L., Nishizono, R., Chowdhury, M.,

2375   Hodgin, J., Wiggins, P.A., and Wiggins, R.C. (2014). Estimating podocyte number and density

2376   using a single histologic section. Journal of the American Society of Nephrology : JASN *25*,

2377   1118-1129.

2378   Vilenchik, M.M., and Knudson, A.G. (2003). Endogenous DNA double-strand breaks:
2379   Production, fidelity of repair, and induction of cancer. Proceedings of the National Academy of
2380   Sciences *100*, 12871-12876.

2381   Waddington, C.H. (1957). The strategy of the genes; a discussion of some aspects of theoretical
2382   biology (London,: Allen & Unwin).

2383   Weidner, C.I., Lin, Q., Koch, C.M., Eisele, L., Beier, F., Ziegler, P., Bauerschlag, D.O., Jockel,
2384   K.H., Erbel, R., Muhleisen, T.W.*, et al.* (2014). Aging of blood can be tracked by DNA
2385   methylation changes at just three CpG sites. Genome biology *15*, R24.

2386   Welch, R.P., Lee, C., Imbriano, P.M., Patil, S., Weymouth, T.E., Smith, R.A., Scott, L.J., and
2387   Sartor, M.A. (2014). ChIP-Enrich: gene set enrichment testing for ChIP-seq data. Nucleic acids
2388   research *42*, e105.

2389   Welle, S., Brooks, A.I., Delehanty, J.M., Needler, N., Bhatt, K., Shah, B., and Thornton, C.A.
2390   (2004). Skeletal muscle gene expression profiles in 20-29 year old and 65-71 year old women.
2391   Experimental gerontology *39*, 369-377.

2392   Wenz, T., Rossi, S.G., Rotundo, R.L., Spiegelman, B.M., and Moraes, C.T. (2009). Increased
2393   muscle PGC-1α expression protects from sarcopenia and metabolic disease during aging.
2394   Proceedings of the National Academy of Sciences *106*, 20405-20410.

2395   White, R.R., and Vijg, J. (2016). Do DNA Double-Strand Breaks Drive Aging? Molecular cell *63*,
2396   729-738.

2397   Whitehead, J.C., Hildebrand, B.A., Sun, M., Rockwood, M.R., Rose, R.A., Rockwood, K., and
2398   Howlett, S.E. (2013). A Clinical Frailty Index in Aging Mice: Comparisons With Frailty Index Data
2399   in Humans. The Journals of Gerontology: Series A *69*, 621-632.

2400   Williams, G.C. (1957). Pleiotropy, Natural Selection, and the Evolution of Senescence. Evolution
2401   *11*, 398-411.

2402 Wittmayer, P.K., McKenzie, J.L., and Raines, R.T. (1998). Degenerate DNA recognition by I-
2403 PpoI endonuclease. Gene *206*, 11-21.

2404 Wolf, N., Pendergrass, W., Singh, N., Swisshelm, K., and Schwartz, J. (2008). Radiation
2405 cataracts: mechanisms involved in their long delayed occurrence but then rapid progression.
2406 Molecular vision *14*, 274-285.

2407 Wolf, N.S., Li, Y., Pendergrass, W., Schmeider, C., and Turturro, A. (2000). Normal mouse and
2408 rat strains as models for age-related cataract and the effect of caloric restriction on its
2409 development. Experimental eye research *70*, 683-692.

2410 Wood, J.G., Jones, B.C., Jiang, N., Chang, C., Hosier, S., Wickremesinghe, P., Garcia, M.,
2411 Hartnett, D.A., Burhenn, L., Neretti, N.*, et al.* (2016). Chromatin-modifying genetic interventions
2412 suppress age-associated transposable element activation and extend life span in Drosophila.
2413 Proceedings of the National Academy of Sciences of the United States of America *113*, 11277-
2414 11282.

2415 Yang, J.H., Song, Y., Seol, J.H., Park, J.Y., Yang, Y.J., Han, J.W., Youn, H.D., and Cho, E.J.
2416 (2011). Myogenic transcriptional activation of MyoD mediated by replication-independent
2417 histone deposition. Proceedings of the National Academy of Sciences of the United States of
2418 America *108*, 85-90.

2419 Yang, T., Zhang, F., Yardimci, G.G., Song, F., Hardison, R.C., Noble, W.S., Yue, F., and Li, Q.
2420 (2017). HiCRep: assessing the reproducibility of Hi-C data using a stratum-adjusted correlation
2421 coefficient. Genome research *27*, 1939-1949.

2422 Zeng, Q., Chen, X., Ning, C., Zhu, Q., Yao, Y., Zhao, Y., and Luan, F. (2018). Methylation of the
2423 genes ROD1, NLRC5, and HKR1 is associated with aging in Hainan centenarians. BMC
2424 medical genomics *11*, 7.

2425   Zhang, J., Pippin, J.W., Krofft, R.D., Naito, S., Liu, Z.H., and Shankland, S.J. (2013). Podocyte
2426   repopulation by renal progenitor cells following glucocorticoids treatment in experimental FSGS.
2427   Am J Physiol Renal Physiol *304*, F1375-1389.
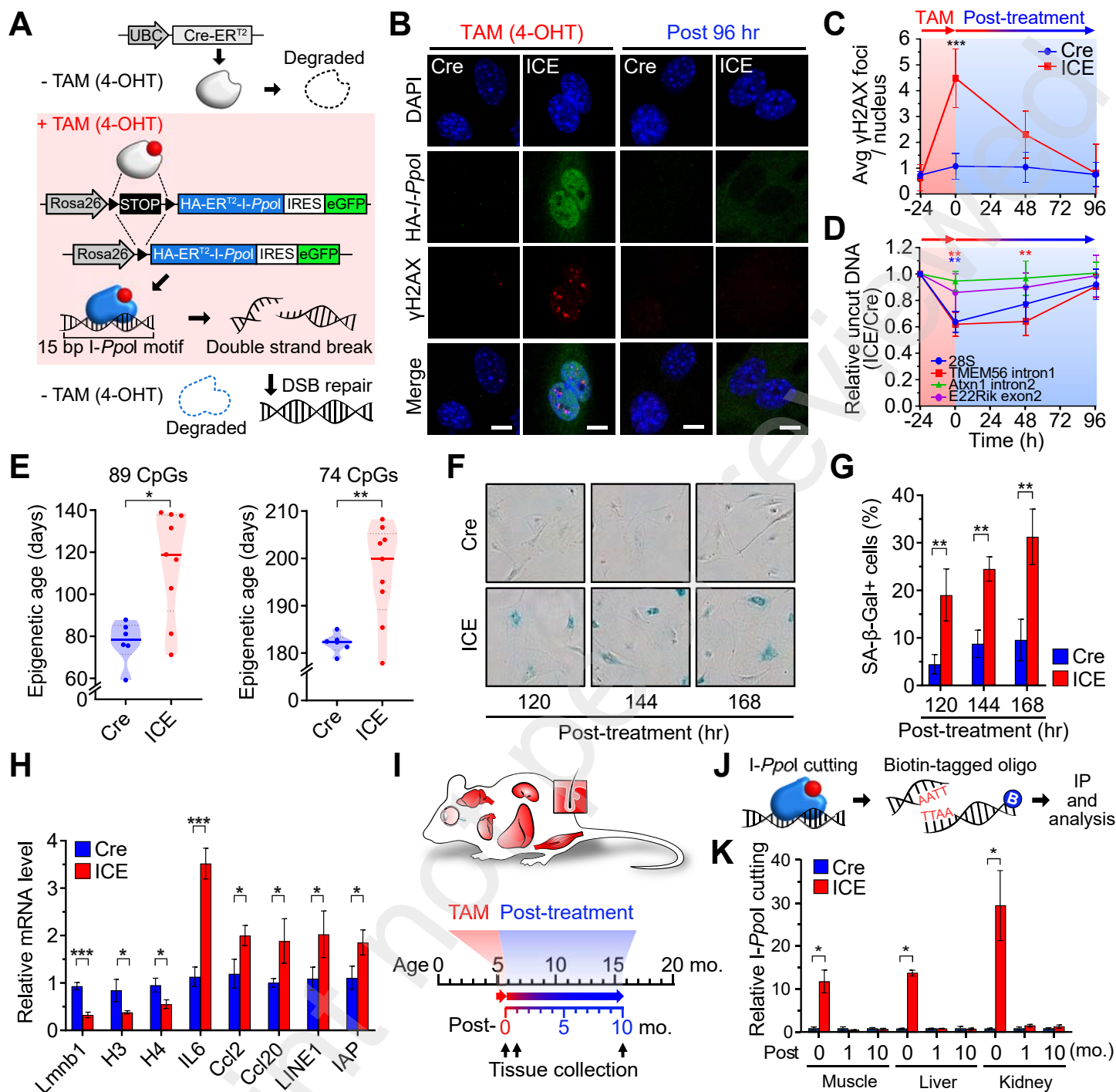
2428   Zhang, Y., Hapala, J., Brenner, H., and Wagner, W. (2017). Individual CpG sites that are
2429   associated with age and life expectancy become hypomethylated upon aging. Clinical
2430   epigenetics *9*, 9.

2431   Zhao, Y., Yi, J., Tao, L., Huang, G., Chu, X., Song, H., and Chen, L. (2018). Wnt signaling
2432   induces radioresistance through upregulating HMGB1 in esophageal squamous cell carcinoma.
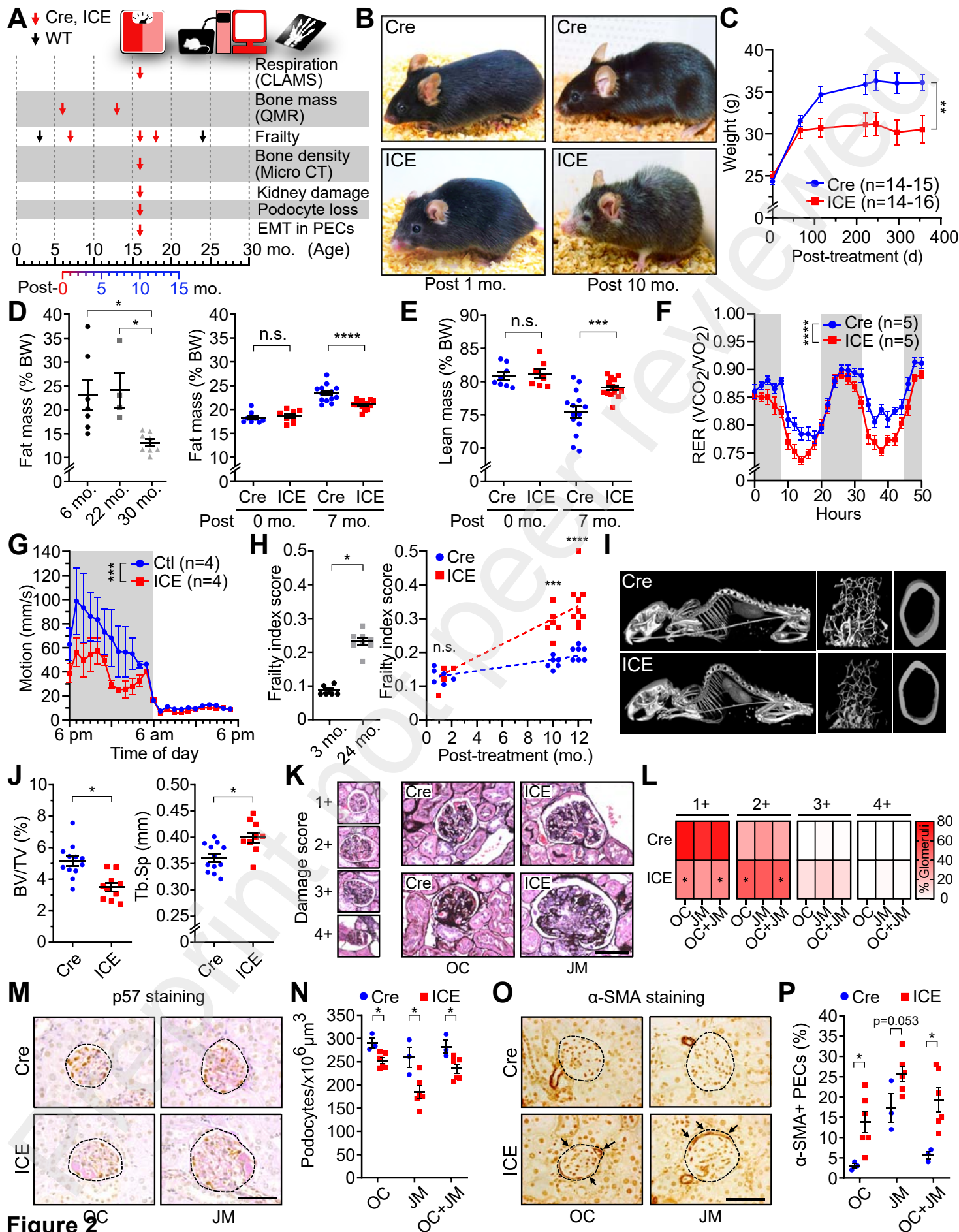2433   Cell death & disease *9*, 433.

2434   Zirkel, A., Nikolic, M., Sofiadis, K., Mallm, J.P., Brackley, C.A., Gothe, H., Drechsel, O., Becker,
2435   C., Altmüller, J., Josipovic, N.*, et al.* (2018). HMGB2 Loss upon Senescence Entry Disrupts
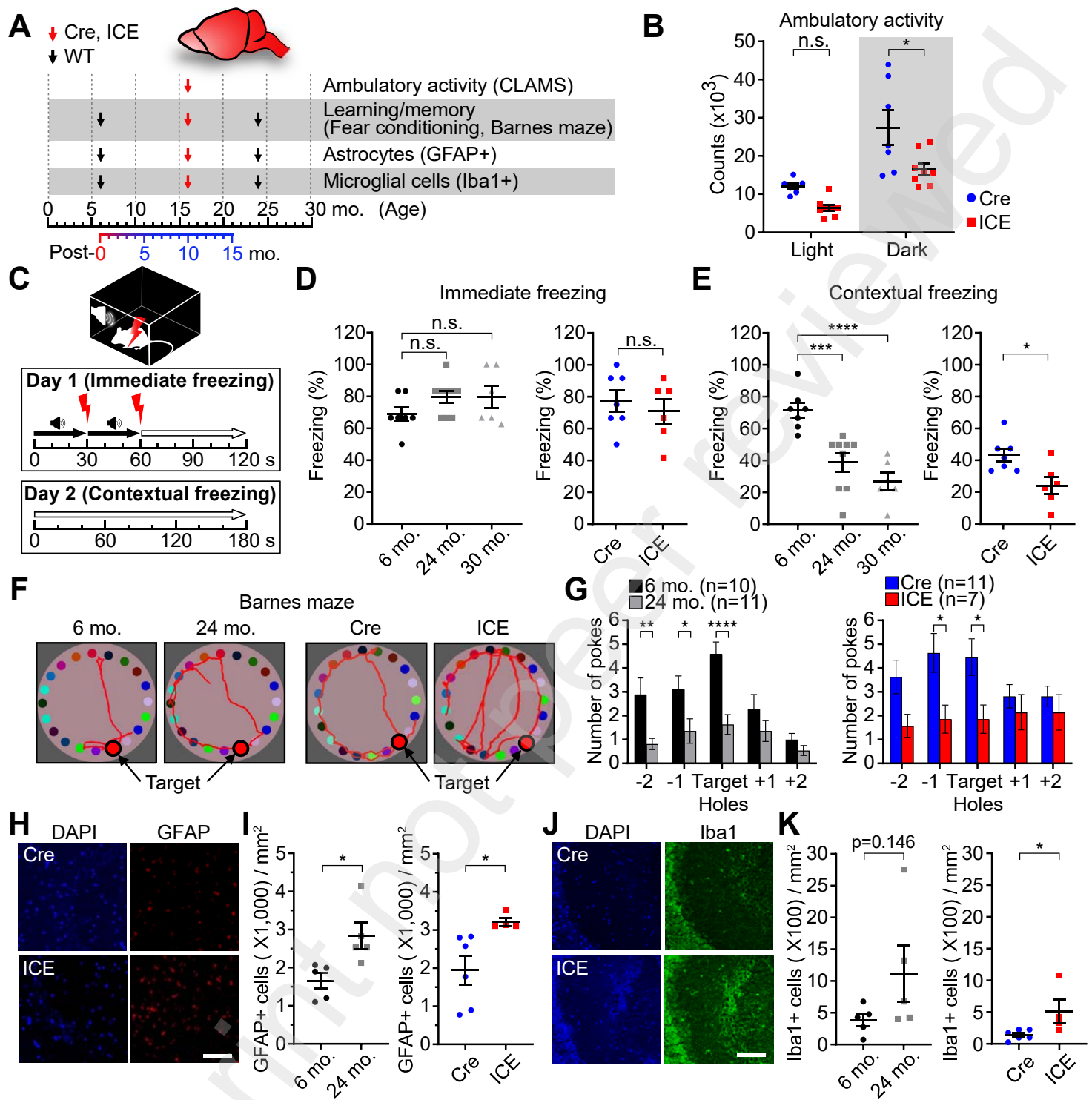2436   Genomic Organization and Induces CTCF Clustering across Cell Types. Molecular cell *70*, 730-
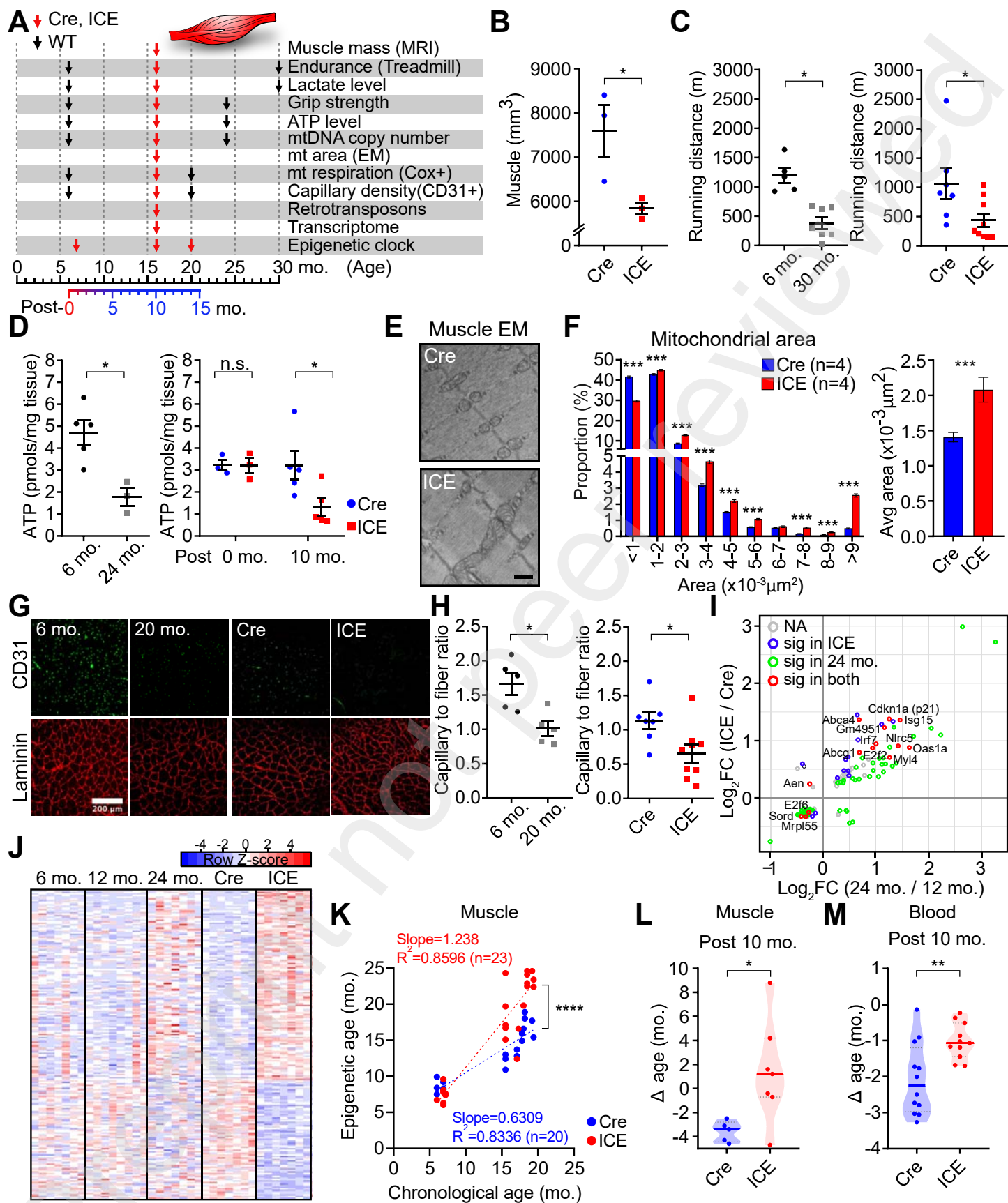2437   744.e736.
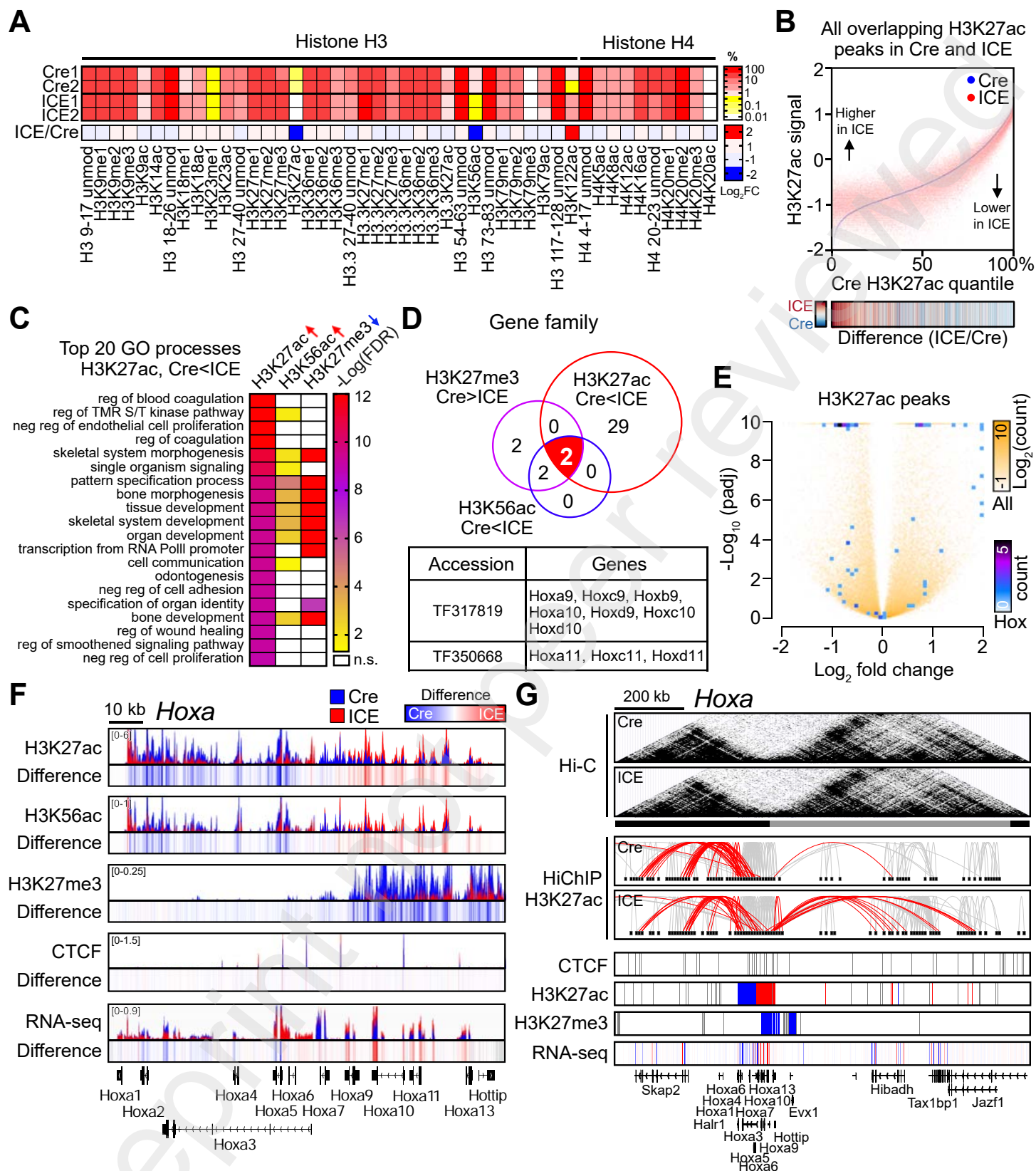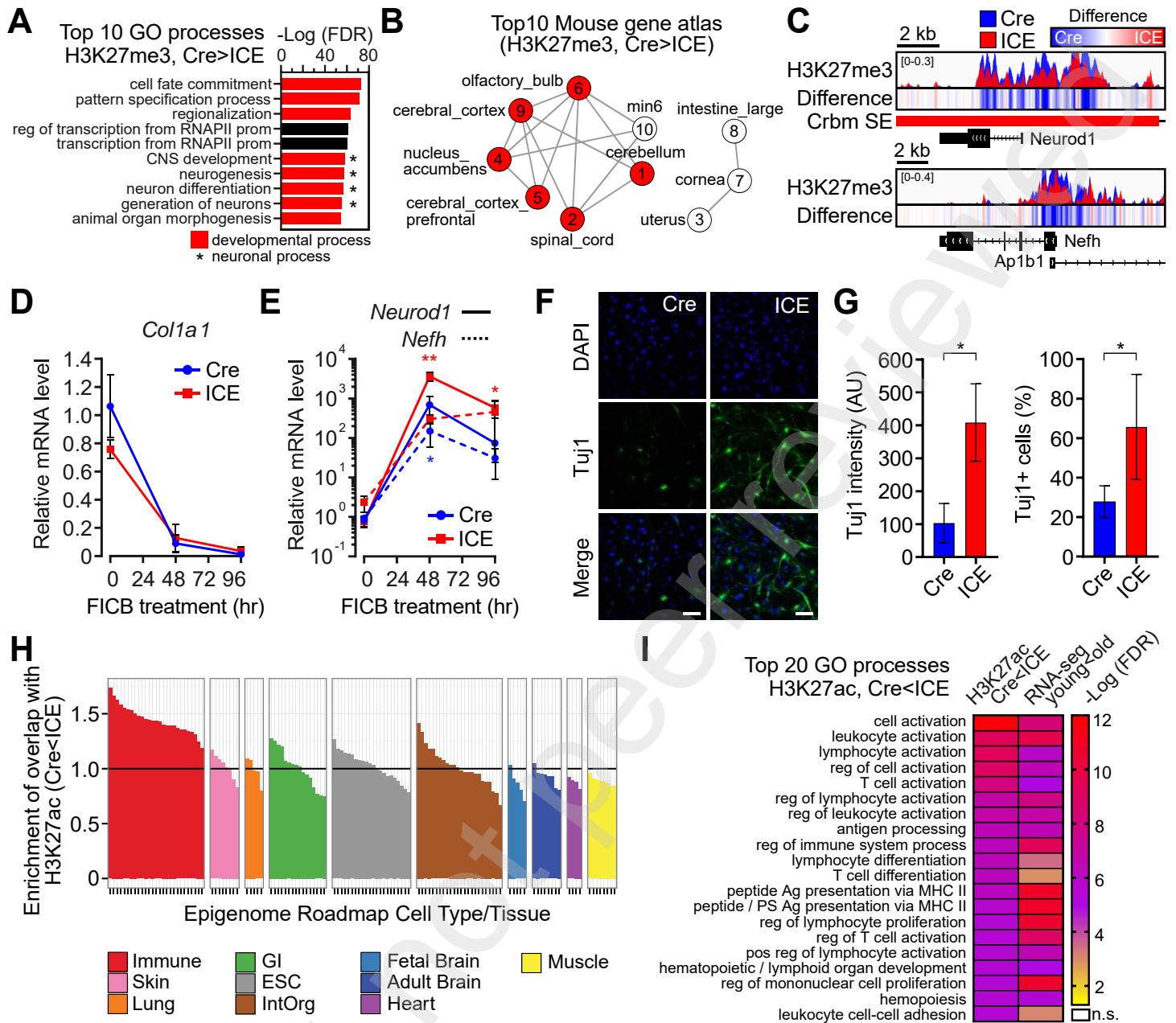2438
2439
2440
2441

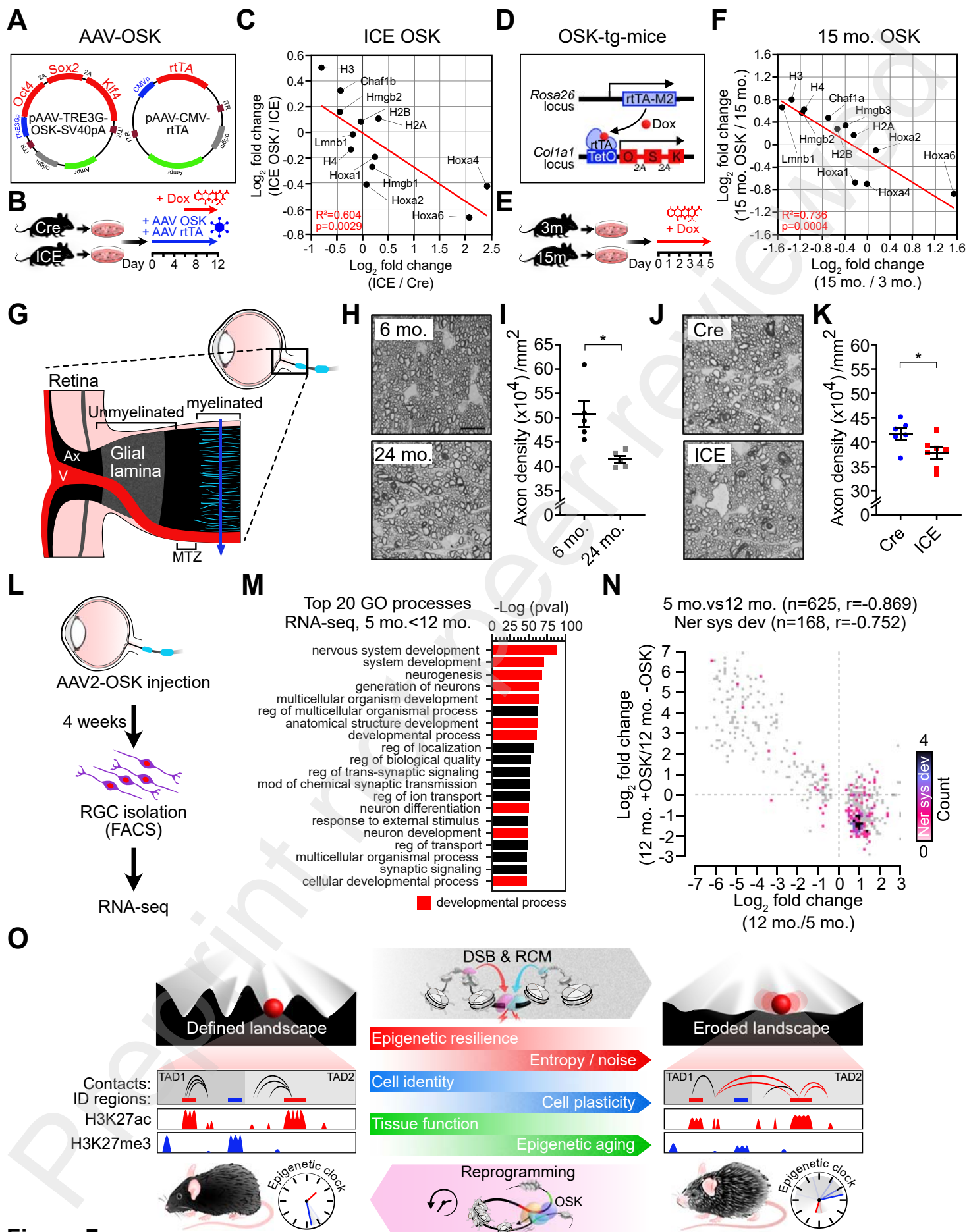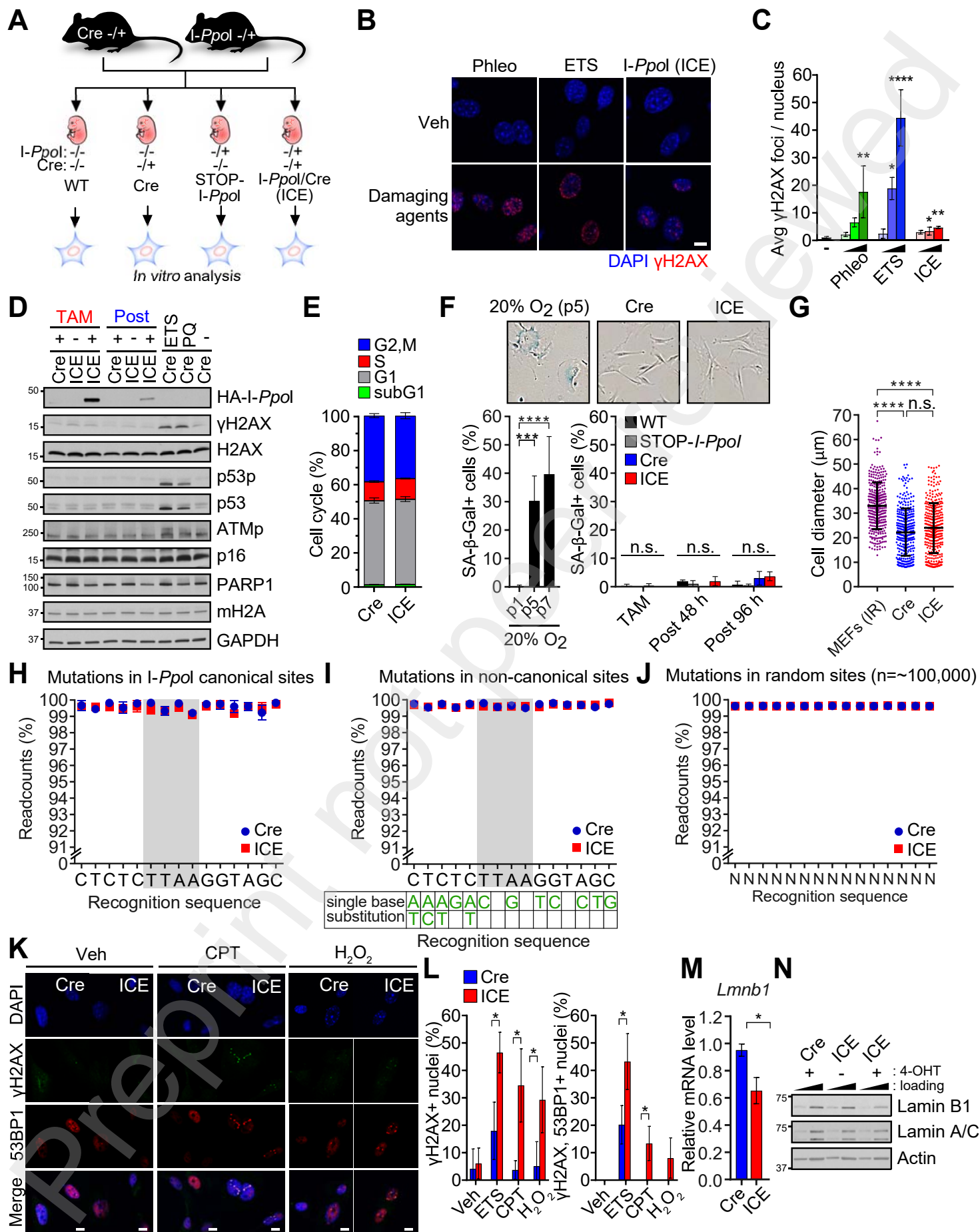**Figure 1**

Figure 2

Figure 3

Figure 4

Figure 5

A Top 10 GO processes
H3K27me3, Cre>ICE   -Log (FDR)

cell fate commitment
pattern specification process
regionalization
reg of transcription from RNAPII prom
transcription from RNAPII prom
CNS development *
neurogenesis *
neuron differentiation *
generation of neurons *
animal organ morphogenesis

■ developmental process
* neuronal process

B Top10 Mouse gene atlas
(H3K27me3, Cre>ICE)

olfactory_bulb ⑥
cerebral_cortex ⑨   min6   intestine_large ⑧
nucleus_ ④   cerebellum ①
accumbens   cornea ⑦
cerebral_cortex ⑤
prefrontal   uterus ③
spinal_cord ②

C
2 kb   ■ Cre ■ ICE   Difference
H3K27me3 [0-0.3]
Difference
Crbm SE
Neurod1

2 kb
H3K27me3 [0-0.4]
Difference
Nefh
Ap1b1

D *Col1a1*

Relative mRNA level
FICB treatment (hr)
● Cre ■ ICE

E *Neurod1* ——
Nefh ·····

Relative mRNA level
FICB treatment (hr)
● Cre ■ ICE

F   Cre   ICE

DAPI
Tuj1
Merge

G
Tuj1 intensity (AU)   *
Cre ICE

Tuj1+ cells (%)   *
Cre ICE

H
Enrichment of overlap with
H3K27ac (Cre<ICE)

Epigenome Roadmap Cell Type/Tissue

■ Immune   ■ GI   ■ Fetal Brain   ■ Muscle
■ Skin   ■ ESC   ■ Adult Brain
■ Lung   ■ IntOrg   ■ Heart

I Top 20 GO processes
H3K27ac, Cre<ICE

H3K27ac   RNA-seq
Cre<ICE   young<old   -Log (FDR)

cell activation
leukocyte activation
lymphocyte activation
reg of cell activation
T cell activation
reg of lymphocyte activation
reg of leukocyte activation
antigen processing
reg of immune system process
lymphocyte differentiation
T cell differentiation
peptide Ag presentation via MHC II
peptide / PS Ag presentation via MHC II
reg of lymphocyte proliferation
reg of T cell activation
pos reg of lymphocyte activation
hematopoietic / lymphoid organ development
reg of mononuclear cell proliferation
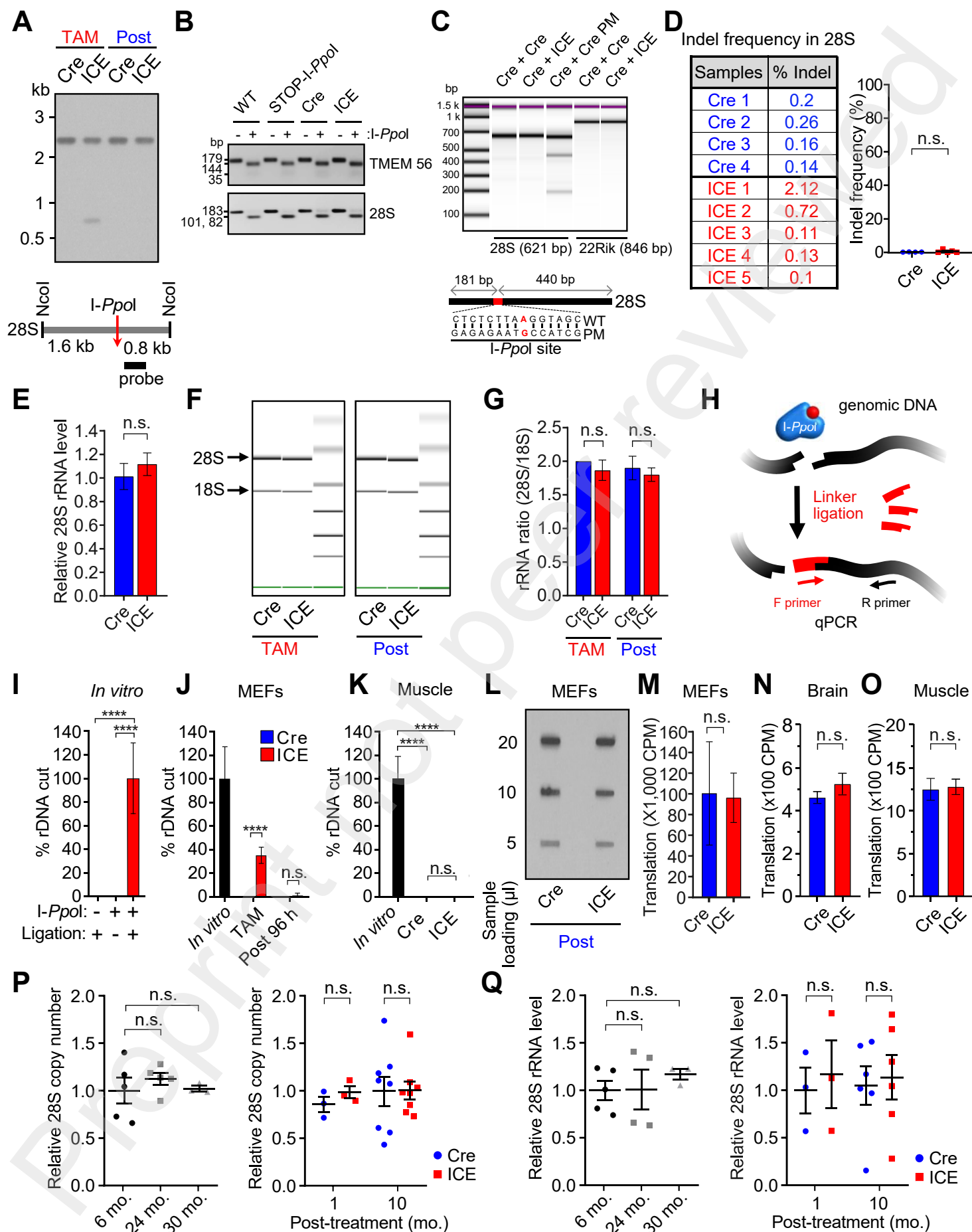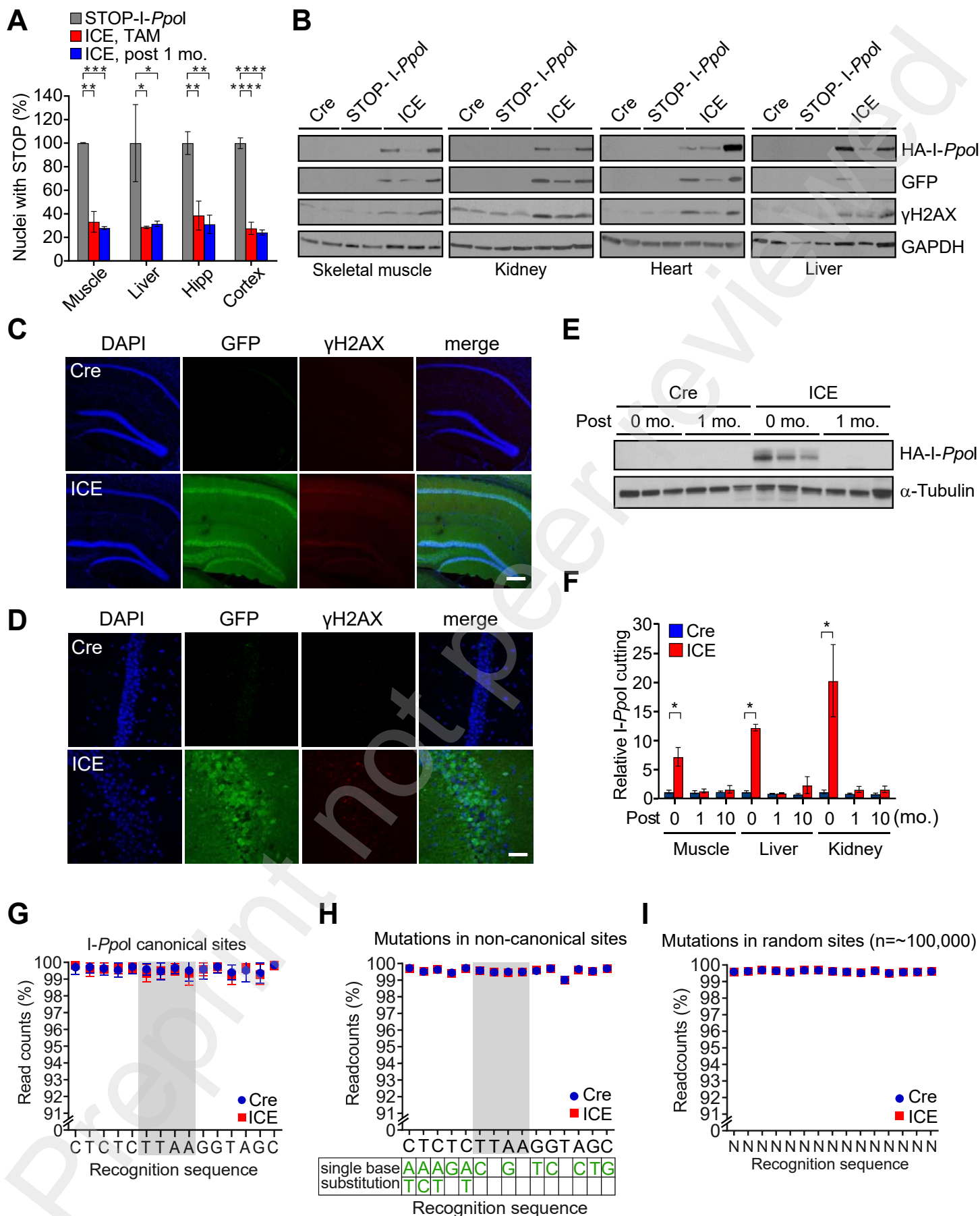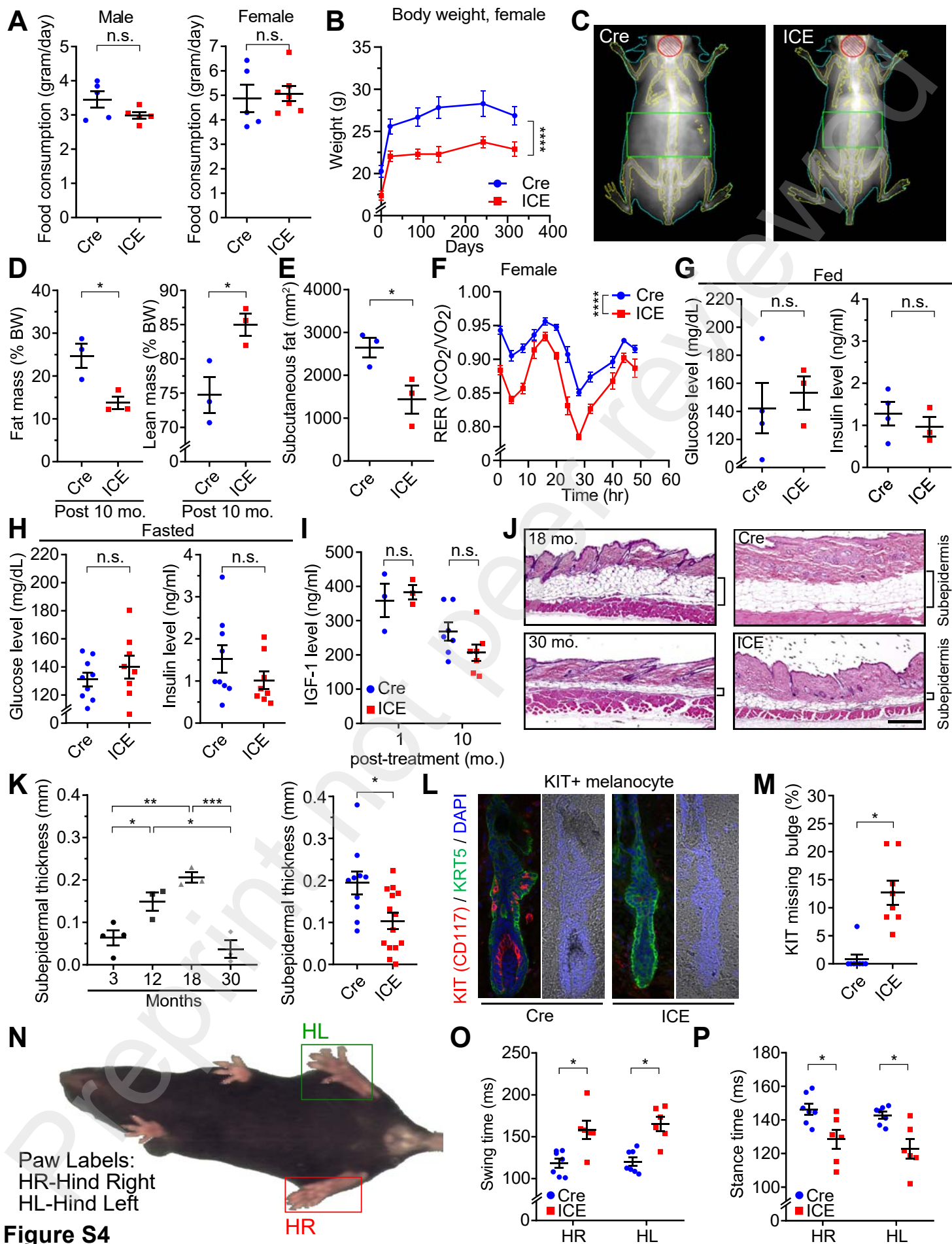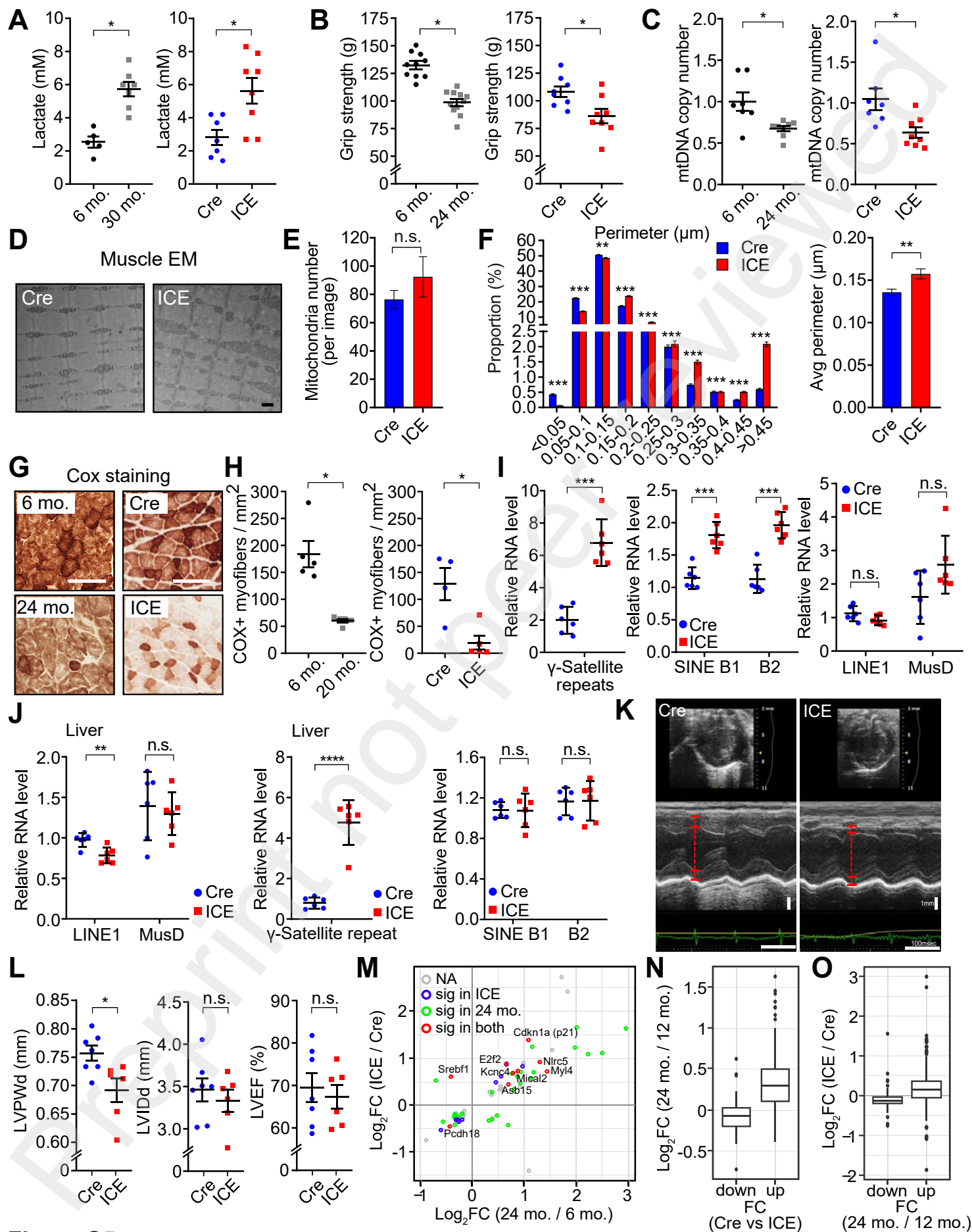hemopoiesis
leukocyte cell-cell adhesion
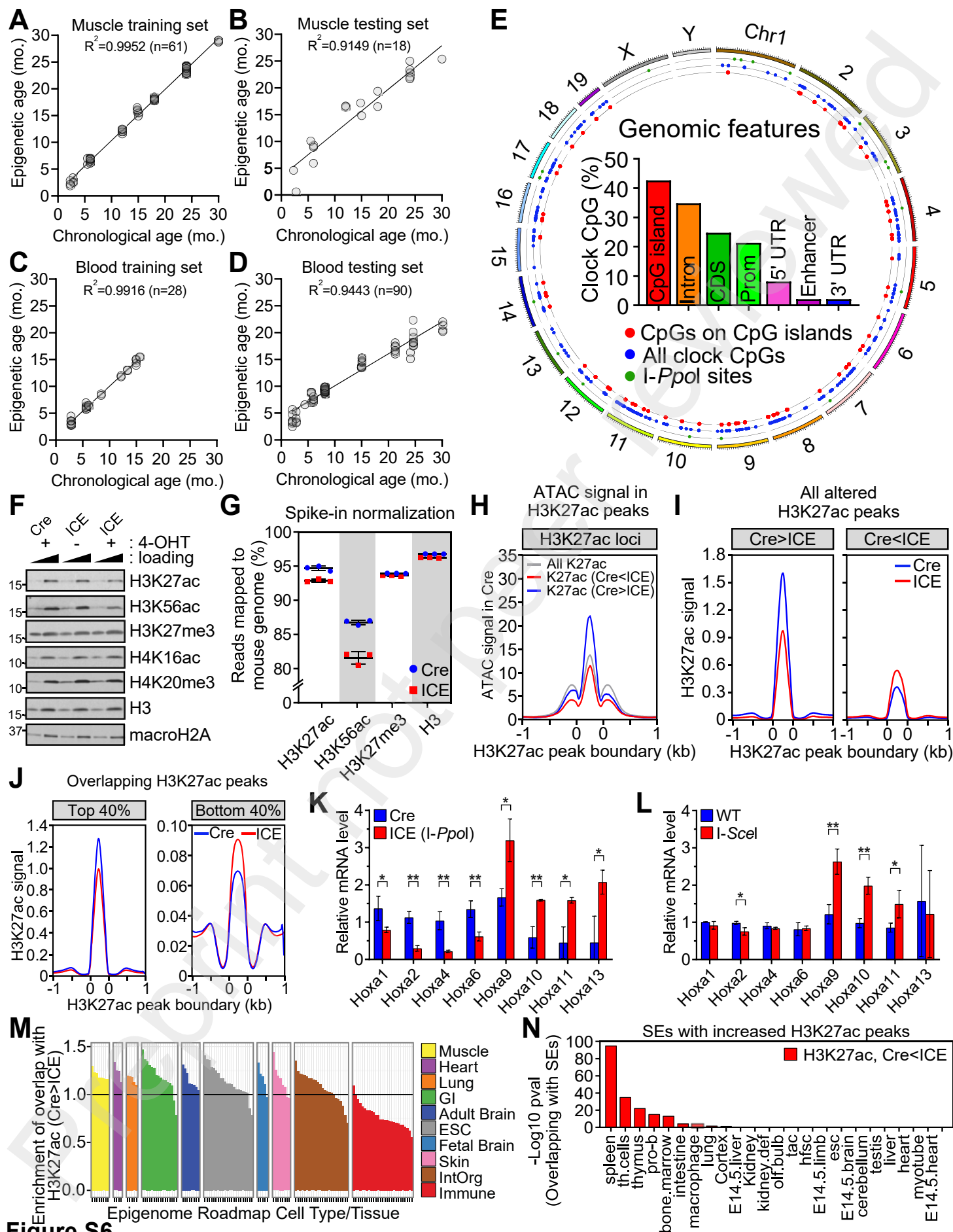
□ n.s.

Figure 6

Figure 7

Figure S1
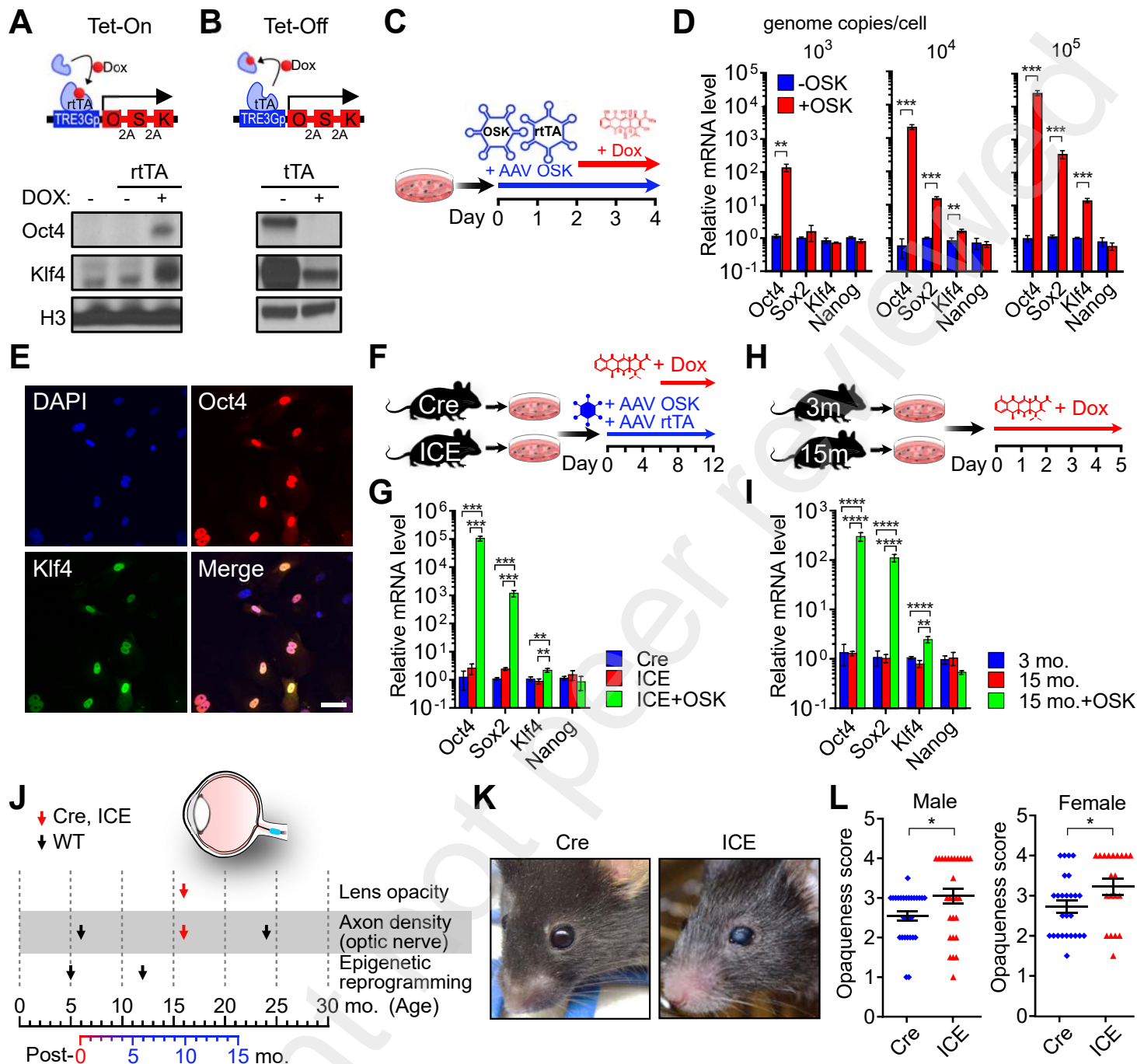
Figure S2

Figure S3

Figure S4

Paw Labels:
HR-Hind Right
HL-Hind Left

Figure S5

Figure S6

Figure S7